

DUDLEY BOX LIBRARY
NAVAL POSTGRADUATE SCHOOL
MONTEREY CA 93943-5101

NAVAL POSTGRADUATE SCHOOL

Monterey, California



DISSERTATION

A Three-Dimensional Study of the Influence
of Mountains on a Front

by

Shang-Wu Li

December 1992

Co-Advisor: Melinda S. Peng
Co-Advisor: Roger T. Williams

Approved for public release; distribution unlimited

Unclassified

Security Classification of this page

REPORT DOCUMENTATION PAGE

1a Report Security Classification UNCLASSIFIED		1b Restrictive Markings	
2a Security Classification Authority		3 Distribution Availability of Report Approved for public release; distribution is unlimited	
2b Declassification/Downgrading Schedule		5 Monitoring Organization Report Number(s)	
4 Performing Organization Report Number(s)		7a Name of Monitoring Organization Naval Postgraduate School	
6a Name of Performing Organization Naval Postgraduate School	6b Office Symbol (If Applicable) MR	7b Address (city, state, and ZIP code) Monterey, CA 93943-5000	
6c Address (city, state, and ZIP code) Monterey, CA 93943-5000		9 Procurement Instrument Identification Number	
8a Name of Funding/Sponsoring Organization	8b Office Symbol (If Applicable)	10 Source of Funding Numbers	
8c Address (city, state, and ZIP code)		Program Element Number	Project No.
		Task No.	Work Unit Accession No.
11 Title (Include Security Classification) A three dimensional Study of the Influence of Mountains on a Front (Unclassified)			
12 Personal Author(s) Li, Shang-Wu			
13a Type of Report Ph. D Dissertation	13b Time Covered	14 Date of Report (year, month, day) 1992, December	15 Page Count 142

16 Supplementary Notation		
17 Cosati Codes		18 Subject Terms Front Mountain Frontogenesis Numerical Model
Field	Group	

19 Abstract (continue on reverse if necessary and identify by block number)

This study investigates mountain effects on a frontal system in three dimensions. A numerical hydrostatic primitive-equation model is employed. The frontal system is developed in the model from the most unstable Eady wave in a baroclinic state and is then introduced into a new model domain that contains mountain ridges of different sizes, shapes and orientations.

20 Distribution/Availability of Abstract (x) appropriate box <input checked="" type="checkbox"/> unclassified/unlimited <input type="checkbox"/> same as report <input type="checkbox"/> DTIC users		21 Abstract Security Classification Unclassified	
22a Name of Responsible Individual Roger T. Williams / Melinda S. Peng		22b Telephone (Include Area code) (408)646-2722	22c Office Symbol MR/Wu MR/Pg

19 Abstract Continued:

The cold front experiences a weakening on the upwind slope and strengthening on the downwind slope of a mountain. Mountain-induced frontogenetic forcing by these winds associated with the front produces frontogenesis/frontolysis at different locations. The deformation and the distortion of the front by a mountain is a superposition effect of the mountain-induced frontogenesis regions and the original front. The front recovers its original horizontal structure after moves away from the mountain.

The frontogenetic forcing is dominated mainly by the convergence/divergence associated with the flow over the mountain. Major intensification occurs on the lee side convergence zone. Frontal intensity returns approximately to the original level when the front moves away from the mountain. Mountain orientation is an important factor that determines the frontal distortion.

Approved for public release; distribution unlimited

A Three-Dimensional Study of the Influence of Mountains on a Front

by

Shang-Wu Li
Civilian, Central Weather Bureau, ROC
B.S. Chinese Culture University, 1979
M.S. National Taiwan University, 1986

Submitted in partial fulfillment of the
requirements for the degree of

DOCTOR OF PHILOSOPHY IN METEOROLOGY

from the
NAVAL POSTGRADUATE SCHOOL

December 1992

c./

ABSTRACT

This study investigates mountain effects on a frontal system in three dimensions. A numerical hydrostatic primitive-equation model is employed. The frontal system is developed in the model from the most unstable Eady wave in a baroclinic state and is then introduced into a new model domain that contains mountain ridges of different sizes, shapes and orientations.

The cold front experiences a weakening on the upwind slope and strengthening on the downwind slope of a mountain. Mountain-induced frontogenetic forcing by these winds associated with the front produces frontogenesis/frontolysis at different locations. The deformation and the distortion of the front by a mountain is a superposition effect of the mountain-induced frontogenesis regions and the original front. The front recovers its original horizontal structure after moves away from the mountain.

The frontogenetic forcing is dominated mainly by the convergence/divergence associated with the flow over the mountain. Major intensification occurs on the lee side convergence zone. Frontal intensity returns approximately to the original level when the front moves away from the mountain. Mountain orientation is an important factor that determines the frontal distortion.

TABLE OF CONTENTS

I.	INTRODUCTION.....	1
A.	OBSERVATIONS.....	2
B.	REVIEW OF PREVIOUS STUDIES.....	6
C.	SUMMARY AND PROPOSED STUDY.....	10
II.	NUMERICAL MODEL DESCRIPTION.....	13
A.	NUMERICAL METHOD	13
B.	INITIAL AND BOUNDARY CONDITIONS.....	13
III.	MOUNTAIN SOLUTION.....	15
A.	UNIFORM FLOW	16
1.	Flow over Large-scale Mountains.....	19
2.	Mesoscale Flow Response.....	20
B.	BAROCLINIC FLOW	20
1.	Large-scale Mountain.....	20
2.	Mesoscale Mountain.....	22
C.	EFFECTS OF HORIZONTAL ASPECT RATIO.....	22
D.	SUMMARY.....	25
IV.	FRONTAL SOLUTION.....	31
A.	BAROCLINIC FRONTOGENESIS	34
1.	Initial Conditions.....	34
2.	Evolution of a Frontal System.....	34
B.	SUMMARY.....	36
V.	INFLUENCE OF MOUNTAINS ON A FRONTAL SYSTEM	37
A.	INTRODUCTION OF A FRONTAL SYSTEM INTO A NEW DOMAIN	38

1.	Boundary Condition Treatment.....	39
2.	Frontal Structure in the New Domain.....	40
B.	EXPERIMENTAL APPROACH	40
1.	Mountain Structure and Model Configuration.....	40
2.	Description of Cases.....	44
C.	DISCUSSIONS OF RESULTS.....	45
1.	Case 1: Large-scale Circular Mountain.....	45
a.	Analysis of The Results.....	45
b.	Frontogenetic Forcing.....	54
c.	Summary	57
2.	Case 2: Meso-Scale Circular Mountain.....	58
a.	Analysis of The Results.....	58
b.	Frontogenetic Forcing.....	62
c.	Summary.....	63
3.	Case 3: East-West Oriented Mountain Ridge.....	65
a.	Analysis of The Results.....	65
b.	Frontogenetic Forcing.....	74
c.	Summary.....	80
4.	Case 4: North-South Oriented Mountain Ridge	82
a.	Analysis of The Results.....	82
b.	Frontogenetic Forcing.....	86
c.	Summary.....	90
5.	Case 5: Mountain With The Major Axis Parallel To The Approaching Front.....	92
a.	Analysis of The Results.....	92

b. Frontogenetic Forcing.....	97
c. Summary.....	99
D. SUMMARY.....	99
VI. SUMMARY AND CONCLUSION.....	109
APPENDIX A MODEL CONFIGURATIONS.....	115
APPENDIX B NUMERICAL METHOD.....	116
REFERENCES.....	118
INITIAL DISTRIBUTION LIST.....	122

LIST OF TABLES

TABLE 1 SUMMARY OF MOUNTAIN SCALES FOR ALL CASES.	43
--	----

LIST OF FIGURES

1.1 Streamlines and isotherms (dashed line in °C) on 850 hpa surface of frontal passages on 8 Oct. 1987 (top) and 12 Nov. 1987 (bottom) (after Kurz 1990)....	4
1.2 Schematic illustrations of frontal passage in the Alps and its associated phenomena from Smith (1987).....	5
3.1 The vertical profile of the mountain $h(x,y) = H_m/(x^2/a_0x^2 + y^2/a_0y^2 + 1)^{3/2}$, along the zonal (x) direction.....	17
3.2 Mountain solutions for uniform flow over a large-scale circular mountain at $t = 48$ h: (a) Streamlines at $\sigma = 0.9975$; (b) Vertical velocity (ω) with contour interval = 0.7 mb/h and upward (downward) motion in dashed (solid) lines; and (c) Vertical profile (0-8 km) of the potential temperature (°K) along an east-west cross-section passing through the mountain.....	17,18
3.3 Mountain solutions as in Fig. 3.2(a) and (c) except over a mesoscale circular mountain.....	21
3.4 Mountain solutions as in Fig. 3.2(a) and (c) except for a baroclinic flow over a large-scale circular mountain at $t = 72$ h.....	23
3.5 Mountain solutions as in Fig. 3.2(a) and (c) except for a baroclinic flow over a mesoscale circular mountain at $t = 48$ h.....	24
3.6 Mountain solutions for an uniform flow over the east-west oriented elliptical mountain at $t = 48$ h: (a) geostrophic wind on $\sigma = 0.9975$; (b) ageostrophic wind on $\sigma = 0.9975$; (c) Vertical profile (0 to 8 km) of potential temperature (°K) along an east-west cross-section through the mountain.....	27
3.7 Mountain solutions for a uniform flow over a north-south oriented mountain at $t = 48$ h: (a) Streamlines on $\sigma = 0.9975$; (b) Vertical profile (0 to 8 km) of	

potential temperature ($^{\circ}$ K) along an east-west cross-section through the mountain.....	29
3.8 Mountain solutions for a baroclinic flow over a north-south oriented mountain at $t = 72$ h: (a) surface wind vectors with a maximum of 25 m/s; and (b) divergence field for the surface wind, contour interval $0.2 \times 10^{-4} \text{ s}^{-1}$ with positive (negative) values in dashed (solid) lines.....	30
4.1 Vertical profile of the initial condition along an east-west cross-section in the middle of the domain for the frontogenesis process: (a) potential temperature ($^{\circ}$ K); (b) u , with contour interval of 2 m/s; and (c) v' , with contour interval is 2 m/s, and positive (negative) values in solid (dashed) lines.....	33
4.2 Frontal system on the sea-level surface at $t = 96$ h: (a) potential temperature ($^{\circ}$ K); and (b) wind vectors with maximum of 29 m/s.....	35
5.1 Time evolution each 6 h, from 48 h to 96 h, of the d-value (contour interval 300 km) of a frontal system introduced to a new model domain.....	41
5.2 Frontal system in the new domain with no mountain at $t = 54$ h: (a) sea-level potential temperature ($^{\circ}$ K), and (b) sea surface wind with a maximum vector of 32 m/s.....	42
5.3 Position of the cold front without a mountain determined by tracing the minimum d-value. Time interval is 6 h, the leftmost position is at 36 h and the rightmost one is at 96 h.....	43
5.4 Time evolution each 6 h from $t = 48$ h to $t = 96$ h of the d-value (km) of a front passage over the large-scale circular mountain in Case 1.....	47
5.5 Frontal system approaching large-scale circular mountain at $t = 24$ h in Case 1 on the level of $\sigma = 0.99$: (a) wind field, with contour interval 5 m/s; (b)	

vorticity, with contour interval of $0.55 \times 10^{-5} \text{ s}^{-1}$, maximum value = $0.45 \times 10^{-4} \text{ s}^{-1}$ and minimum value = $-0.7 \times 10^{-4} \text{ s}^{-1}$	48
5.6 Frontal system over large-scale circular mountain at $t = 48 \text{ h}$: (a) sea-level potential temperature ($^{\circ} \text{K}$); and (b) terrain surface wind with the maximum wind speed 36 m/s	50
5.7 As in Fig. 5.6 except for $t = 60 \text{ h}$, and maximum surface wind of 38 m/s	51
5.8 As in Fig. 5.6 except for $t = 72 \text{ h}$, and maximum surface wind of 48 m/s	52
5.9 Divergence (contour interval = $0.2 \times 10^{-4} \text{ s}^{-1}$) field for (a) $t = 72 \text{ h}$, (b) $t = 78 \text{ h}$, (c) $t = 84 \text{ h}$ and (d) $t = 90 \text{ h}$. Dashed line indicates convergent zone and solid line indicates divergent zone. The heavy dashed line is the cold front position.....	53
5.10 Horizontal deformation forcing ($^{\circ} \text{K}^2 \text{m}^{-2} \text{s}^{-1}$) on level $\sigma = 0.99$. in the region of frontogenesis (dashed lines) and in the region of frontolysis (solid line) at : (a) $t = 48 \text{ h}$ with minimum value of -0.16×10^{-13} associated with the cold front and -0.25×10^{-14} in the mountain area; (b) $t = 60 \text{ h}$, maximum forcing on northeastern slope with a minimum value of -0.59×10^{-14} ; and (c) $t = 72 \text{ h}$, with maximum forcing (-0.2×10^{-12}) located at the cold front region.....	55
5.11 (a) Stretching and (b) shearing deformation ($^{\circ} \text{K}^2 \text{m}^{-2} \text{s}^{-1}$) at $t = 60 \text{ h}$. The sum of these terms is the total deformation forcing function shown in Fig. 5.10 b. Contour interval 0.5×10^{-14} in both (a) and (b).....	56
5.12 Time (h) evolution of the maximum stretching, shearing, total horizontal deformation and tilting forcing at $\sigma = 0.99$ during the cold front passage over a large scale circular mountain (Case 1). Ordinate has a logarithm scale (unit: $^{\circ} \text{K}^2 \text{m}^{-2} \text{s}^{-1}$).....	56

5.13 Time evolution each 6 h, from 48 h to 96 h, of the d-value (contour interval 300 km) of a frontal passage over a large-scale circular mountain in Case 1.....	59
5.14 Divergence field (contour interval $0.2 \times 10^{-4} \text{ s}^{-1}$) for (a) $t = 66 \text{ h}$, (b) $t = 72 \text{ h}$, (c) $t = 78 \text{ h}$ and (d) $t = 84 \text{ h}$. Dashed line indicates convergent zone and solid lines indicate divergent zone. The heavy dashed line is the cold front position.....	60
5.15 Frontogenesis (dashed lines) and frontolysis (solid lines) regions from horizontal deformation forcing ($^{\circ} \text{K}^2 \text{m}^{-2} \text{s}^{-1}$) on level $\sigma = 0.99$ for the mesoscale circular mountain: (a) $t = 54 \text{ h}$, with minimum value of -0.98×10^{-13} and maximum value of 0.63×10^{-13} , contour interval = 0.14×10^{-13} , (b) $t = 60 \text{ h}$, with a maximum of 0.73×10^{-13} and a minimum of -0.23×10^{-12} , the contour interval 0.4×10^{-13} , (c) $t = 66 \text{ h}$, with maximum value of 0.14×10^{-12} , minimum value of -0.75×10^{-12} and the contour interval is 0.8×10^{-13} , and (d) $t = 72 \text{ h}$, with maximum value of 0.46×10^{-12} , minimum value of -0.63×10^{-12} and the contour interval = 0.8×10^{-13}	61
5.16 Time (h) evolution of the maximum stretching, shearing, total horizontal deformation and tilting forcing at $\sigma = 0.99$ during the cold front passage over a mesoscale circular mountain (Case 2). Ordinate has a logarithmic scale (unit: $^{\circ} \text{K}^2 \text{m}^{-2} \text{s}^{-1}$).....	64
5.17 Time evolution each 6 h from $t = 48 \text{ h}$ to $t = 96 \text{ h}$ of the d-value (km) of a front passage over the east-west oriented mountain in Case 2.....	66
5.18 Frontal system over the east-west oriented mountain at $t = 36 \text{ h}$: (a) sea-level potential temperature ($^{\circ} \text{K}$); and (b) terrain surface wind with the maximum wind speed of 35 m/s	67

5.19 Frontal system over the east-west oriented mountain at $t = 60\text{h}$: (a) sea-level potential temperature ($^{\circ}\text{K}$); and (b) terrain surface wind with the maximum wind speed 38 m/s	68
5.20 Analysis at 850 hpa on 12 UTC October 8. from Fig. 4 of Kurz(1990) (a): Winds (m s^{-1}) and isotherms (dashed, $^{\circ}\text{C}$); (b) frontogenesis function FH (in $10^{-10}\text{ km}^{-1}\text{s}^{-1}$); and (c) omega-forcing (in $10^{-17}\text{ m}^{-1}\text{s}^{-3}$).....	69
5.21 Frontal solution for Case 3 at $t = 66\text{ h}$ when the cold front is on the mountain, (a) sea-level temperature (b) surface wind vector (maximum = 43 m/s).....	71
5.22 As in Fig. 5.21, except for $t = 72\text{ h}$	72
5.23 As in Fig. 5.21, except for $t = 84\text{ h}$ when the front is away from the mountain.	73
5.24 Case 3. Divergence fields (contour interval = $0.2 \times 10^{-4}\text{s}^{-1}$) and cold front positions (heavy dashed line) at (a) $t = 66\text{ h}$, (b) $t = 72\text{ h}$, (c) $t = 78\text{ h}$ and (d) $t = 84\text{ h}$	75
5.25 Horizontal deformation forcing ($^{\circ}\text{K}^2\text{m}^{-2}\text{s}^{-1}$) on level $\sigma = 0.99$. in the region of frontogenesis (dashed lines) and in the region of frontolysis (solid line) at : (a) $t = 54\text{ h}$ with minimum value of -1.3×10^{-13} associated with the cold front and -0.25×10^{-14} in the mountain area, contour interval = 0.1×10^{-12} ; (b) $t = 60\text{ h}$, maximum forcing on northeastern slope with a minimum value of -0.31×10^{-12} , contour interval = 0.1×10^{-12}	76
5.26 Time (h) evolution of the maximum stretching, shearing, total horizontal deformation and tilting forcing at $\sigma = 0.99$ during the cold front passage over the east-west oriented mountain (Case 3). Ordinate has a logarithmic scale (unit: $^{\circ}\text{K}^2\text{m}^{-2}\text{s}^{-1}$).....	78
5.27 Horizontal deformation as in Fig. 5.25, except for (a) $t = 72\text{ h}$, contour interval = 0.6×10^{-12} (unit: $^{\circ}\text{K}^2\text{m}^{-2}\text{s}^{-1}$).....	79

5.28 Time evolution each 6 h from $t = 48$ h to $t = 96$ h of the d-value (km) of a front passage over the north-south oriented mountain in Case 4.....	83
5.29 Frontal system over the north-south oriented mountain (Case 4) at $t = 54$ h: (a) sea-level potential temperature ($^{\circ}$ K); and (b) terrain surface wind with the maximum wind speed of 38 m/s.....	84
5.30 Frontal solution for Case 4 as in Fig. 5.26 except for $t = 60$ h and maximum wind vector = 40 m/s.....	85
5.31 Divergence fields and cold front positions (heavy dashed line) for Case 4: (a) $t = 48$ h, (b) $t = 60$ h, (c) $t = 72$ h and (d) $t = 84$ h, with contour interval = $0.2 \times 10^{-4} \text{ s}^{-1}$	87
5.32 Vertical cross-section through the center of the north-south oriented mountain for potential temperature (panels a to f) and v' (panels g to l), during the frontal passage. The horizontal domain is 5600 km with tick markers at 80 km. Panels (a) to (f) for the potential temperature and (g) to (l) for the north-south wind v' correspond to $t = 48, 54, 60, 66, 72$ and 84 h, respectively. The contour interval is 2° in panels (a) to (f), 3 m/s in panels (g) to (k), and 6 m/s in panel (l). Positive v' is toward the north.....	88,89
5.33 Frontogenetic forcing terms at $t = 54$ h, (a) to (c) and at $t = 60$ h, (d) to (f). (a) and (d) are the stretching deformation, (b) and (e) are shearing deformation, and (c) and (f) are the total horizontal deformation forcing (sum of a and b or d and e). Contour interval is 0.25×10^{-13} (Unit: $\text{K}^2 \text{m}^{-2} \text{s}^{-1}$).....	91
5.34 Case 5. Frontal solution at $t = 50$ h: (a) sea-level temperature ($^{\circ}$ K); (b) surface wind vector (maximum vector = 34 m/s).....	93
5.35 As in Fig. 5.34, except for $t = 60$ h and maximum vector = 40 m/s.....	94
5.36 As in Fig. 5.35, except for $t = 66$ h and maximum vector = 41 m/s.....	95

5.37	Time evolution each 6 h from $t = 48$ h to $t = 96$ h of the d-value (km) of a front passage over the northeast-southwest oriented mountain in Case 5.....	96
5.38	Divergence (Contour interval = $0.2 \times 10^{-4} \text{s}^{-1}$) field for (a) $t = 84$ h, (b) $t = 90$ h. Dashed line indicates convergent zone and solid line indicates divergent zone. The heavy dashed line is the cold front position.....	98
5.39	Horizontal deformation forcing ($^{\circ} \text{K}^2 \text{m}^{-2} \text{s}^{-1}$) on level $\sigma = 0.99$ in the region of frontogenesis (dashed lines) and in the region of frontolysis (solid line) at : (a) $t = 50$ h with minimum value of -0.11×10^{-12} ; (b) $t = 60$ h, maximum forcing on northeastern slope with a minimum value of -0.35×10^{-12}	98
5.40	Magnitude (solid) and angular position (dashed) of the maximum frontogenesis forcing function in the mountain area between 36 h and 96 h for Cases 1 to 5. The horizontal coordinate is the forcing magnitude along the bottom (unit : $10^{-14} \text{K}^2 \text{m}^{-2} \text{s}^{-1}$), and angular position along the top.....	101
5.41	Maximum frontal intensity (d-value, km) of each of cases (value 0 refers to the no-mountain case) from $t = 36$ h to $t = 96$ h.....	103
5.42	Time evolution of the cold front positions for all cases determined by tracing the minimum d-value. Dashed lines indicate the contours of the mountain starting from 500 m, and with an interval of 500 m. Case 0 is the case with no mountain. Note that case 3 has been integrated to $t = 120$ h.....	104
5.43	Frontal positions for the six cases grouped at $t = 48$ (left group), 72 (central group) and 96 h (right group).....	106
5.44	Two-dimensional frontal solutions for (a) cross-frontal wind u (m/s), and (b) along-frontal wind v (m/s) from Williams <i>et al.</i> (1992).....	106

ACKNOWLEDGEMENT

I would first of all like to thank Professors Melinda S. Peng and Roger Terry Williams for their advice and patient guidance. Without the help, encouragement and indeed the pushing of Professor Peng I would not have been able to complete this dissertation. I appreciate Professor Russell I. Elsberry for his careful reading and constructive criticism of the manuscript, which makes this dissertation more readable. I also appreciate Dr. Simon W. Chang from NRL for his guidance in using the NRL Limited Area Numerical Model and constructive comments.

I also thank Central Weather Bureau of my country for sponsoring and giving me the opportunity to study at the Naval Postgraduate School. Without the sponsorship, I would never have had a chance to be educated here. This work is also supported in part by the National Science Foundation under Grant ATM9106495.

I appreciate Professors Robert L. Haney, Chih-Pei Chang and Dr. Chih-Sann Liou for reading and correcting as well as giving comments on the manuscript. The numerical model is supported by Dr. Simon W. Chang from the Naval Research Laboratory.

I want to thank my friend Dr. Ching-hua Wang for her encouragement and assistance with aspects of the computer work, and also many friends for their encouragement and concern: Dr. Hong-Chi Kuo, Tien-Ching Yeh, Jen-Her Chen, Wenwen Tseng, Shan Y. Tsen, David Hand, Winnie Y. Heh, Manlin Wang, Jean Chen, Ching-Huang Liu and Hway-jen Chen. I also appreciate the encouragement

and concern from my colleagues in the numerical weather prediction group and other colleagues in the Central Weather Bureau.

Finally, I would like to express my deep gratitude to my family for their understanding during the years of my absence and to dedicate this dissertation to the honored memory of my Grandfather, who regrettably passed away during my stay in Monterey.

I. INTRODUCTION

The frontal system in an extratropical cyclone is an important phenomenon in the winter hemisphere because of the intense weather associated with it as it passes. The life cycle and the behavior of extratropical cyclones have been extensively studied during the past decades. Palmen and Newton (1969) gave a good review and description of the extratropical cyclone in their book. In addition to advection by the basic current, the frontal system moves counterclockwise (Northern Hemisphere) around the cyclone center. In the early period, the cold front moves southeastward, while the warm front moves very slowly to the northeast. The central portion of a frontal system becomes occluded when the cold front moves northeastward and overtakes the warm front.

It is well known that the dynamics of cyclogenesis and frontogenesis in the midlatitudes are based on baroclinic instability. Linear stability theory (Charney 1947; Eady 1949) indicates that the source of energy for cyclone development is the available potential energy of the original zonal flow. However, nonlinear behavior can modify the results of the linear stability theory. When nonlinear effects are introduced, the growing disturbance is distorted and develops realistic surface frontal structures (Williams 1967; Hoskins and Bretherton 1972; Simmons and Hoskins 1978). Other influences such as diabatic processes and topographic effects may also modify the characteristics of a cyclone or a front.

The objective of this research is to study topographic effects on fronts. Since a great variety of topographies exist on the earth, a moving front may encounter a wide range of terrain effects. Observational studies (e.g., Steinacker 1981; Kurz 1990; and Smith 1986) demonstrate that topography can affect the structure,

translation speed and intensity of a frontal system near a mountain range. These observational studies will be reviewed in section A below.

During the past ten years, the mountain effects on frontal systems have been extensively studied with two-dimensional models or with an idealized frontal structure (Bannon 1983,1984a,b; Davies 1984; Schumann 1987; Williams *et al.* 1992; Zehnder and Bannon 1988). In the few studies that have explored three-dimensional effects, Blumen and Gross (1987b) used a passive scalar and Schumann (1987) treated a few cases with an idealized front. A review of these studies is given by Blumen (1992). A summary of model studies relevant to this research is given in section B below.

A. OBSERVATIONS

The many major mountain ridges of different sizes, heights, shapes and orientations on the earth surface have differing effects on an approaching frontal system. Enhanced observations in field experiments such as ALPEX (ALPine EXperiment) indicated that a cold front may experience retardation and frontolysis on the windward slope and acceleration and intensification on the leeward slope of a mountain ridge.

Bosart *et al.* (1973) studied the east-west oriented, south- or southwest-moving fronts (the so-called back-door front) in the east coast region of the United States. They found that the Appalachians play a prominent role in funnelling shallow cold air pools southward on their eastern side. Horizontal distributions of the frontal passage frequency indicate fronts are distorted by the mountain. Stronger evidence of cold frontal deformation by the terrain in the Rocky Mountain area is shown by Young and Johnson (1984), who utilized the PROFS (Program for Regional Observing and Forecasting Services) surface mesonetwork data and found

that cold fronts followed contours of the terrain height. In the general synoptic analysis, the front moved southward. In a local area mesoscale analysis near Boulder and Denver, the cold air was channeled westward by the mountains, which caused the cold front to follow the terrain height contours.

Well-known analyses of the Alps area by Godske *et al.* (1957) and Steinacker (1981) showed cold frontal deformation near those mountains. Steinacker (1981) showed that the cold air penetrated into valleys from the north, which caused more distortion of fronts and a reduction in frontal speed by a factor of four. McGinley (1982) used observed wind fields to estimate the frontogenetic effects of low-level blocking. The increased temperature gradient required the formation of a secondary circulation that acted to restore thermal wind balance. Hoinka (1986) showed that the average frontal speed in the Alps was 8 m/s on the windward side, 3 m/s across the mountain and 17 m/s on the leeside. He also indicated that the deformation terms show a frontolysis effect on the windward side. Kurz (1990) presented two cases from the German frontal experiment (Fig. 1.1). The first case showed deformation of the front by the Alps as in the other research discussed. The second case showed a new front-like discontinuity that formed ahead of the original front on the north slope of the Alps.

Smith (1986) provided a review of the effects of the Alps on frontal systems. He indicated that several phenomena may occur as a front approaches the mountains (Fig. 1.2). When the mountain is in the pre-frontal southerly wind, there is a foehn phenomenon on the north slope of Alps due to the adiabatic warming caused by the over-mountain flow. The front experiences some distortion as it arrives on the upwind slope of the mountain, and lee waves may be excited when the front passes over the mountain. The incident flow experiences a splitting effect

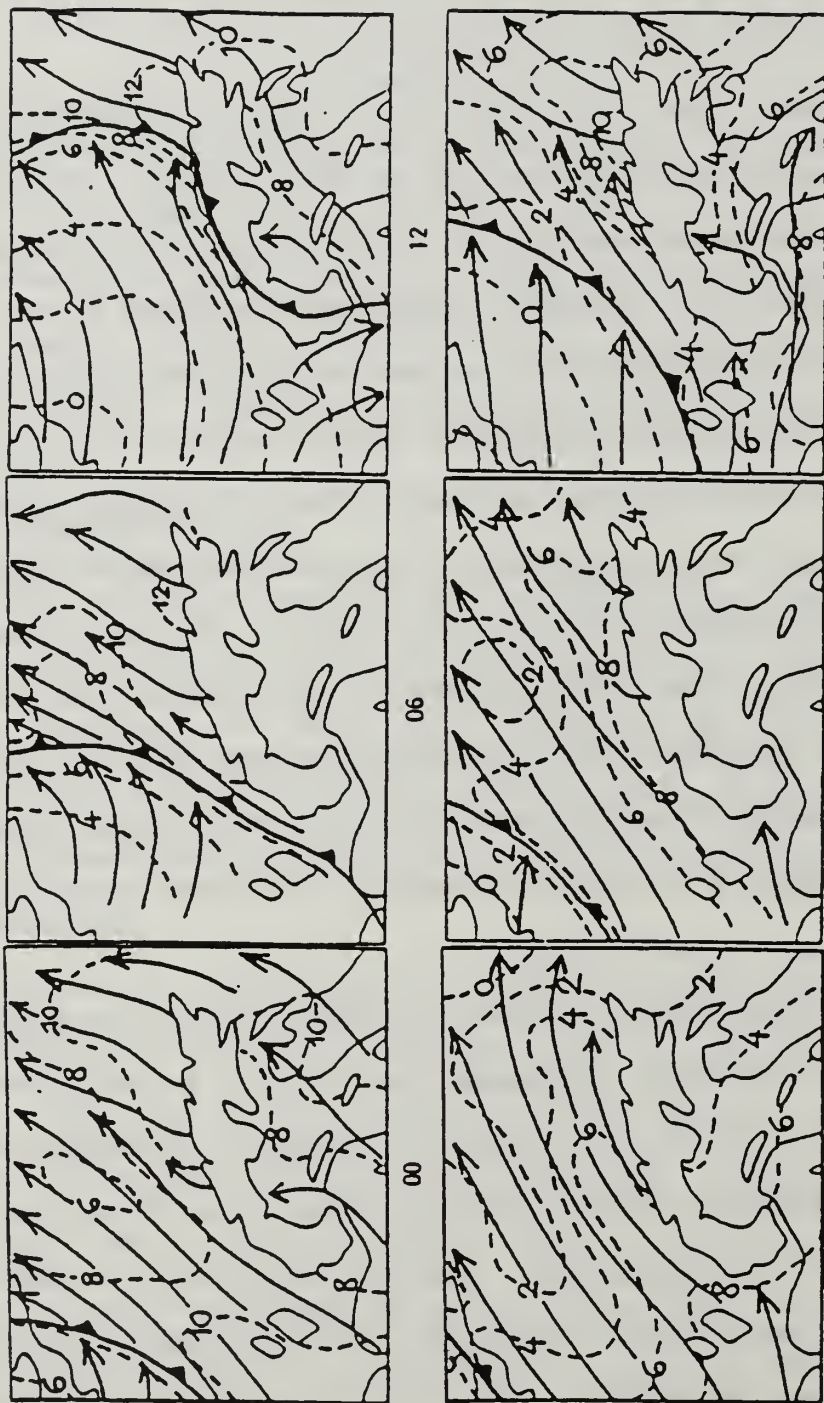


Fig. 1.1 Streamlines and isotherms (dashed line in °C) on 850 hpa surface of frontal passages on 8 Oct. 1987 (top) and 12 Nov. 1987 (bottom) (after Kurz 1990).

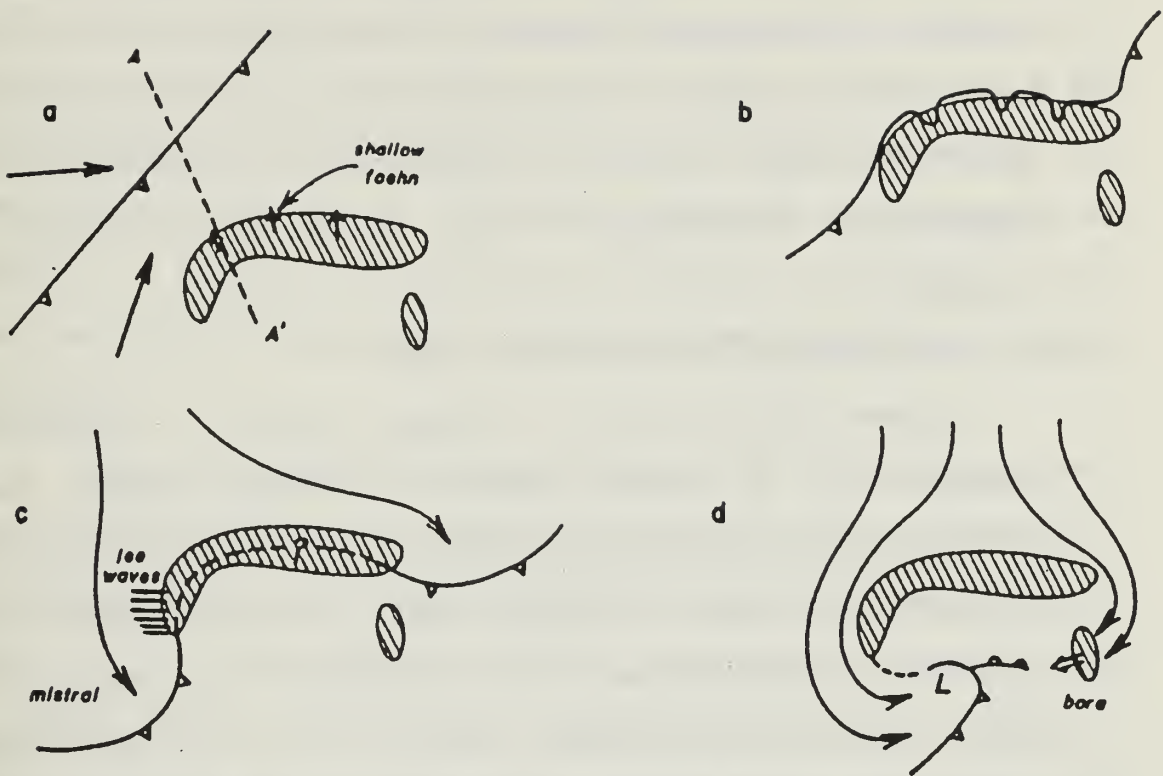


Fig. 1.2 Schematic illustrations of frontal passage in the Alps and its associated phenomena from Smith (1987).

when the mountain is in the post-frontal northerly or northwesterly flow. In this case, the bora phenomenon occurs after the front has passed over the mountain. Smith (1986) summarized some explanations of the frontal deformation that may be due to the blocking or turning of the along-frontal flow or cross-frontal flow and a modification of frontogenetic circulation by the mountain-induced vertical circulation.

B. REVIEW OF PREVIOUS STUDIES

Bannon (1983) derived an analytical solution for quasi-geostrophic frontogenesis in a vertically unbounded, uniformly stratified, Boussinesq atmosphere over a two-dimensional mountain ridge. The front was forced by a vertically constant horizontal deformation field. The quasi-geostrophic mountain solution had an anticyclonic flow over the mountain and a cyclonic flow on the lee side. A translating front experienced a reduction in the static stability before and after it passed over the mountain, while the static stability was increased when the front was over the mountain. While his solution for a cold front had a weakening of the potential temperature gradient on the upwind slope and a strengthening on the lee side, a warm front experienced the opposite behavior. This effect was entirely due to the superposition of the frontal temperature field on the temperature field associated with the mountain solution. Bannon also indicated that the ageostrophic vertical deformation field that was associated with the mountain should retard and weaken the cold front on the upwind slope of the mountain ridge, and conversely it should strengthen the front on the downwind slope.

Bannon (1984a) used a semi-geostrophic equation model with uniform potential vorticity and geostrophic coordinates to include the ageostrophic advection. He linearized the lower boundary condition at $z=0$ rather than at the

mountain surface. The solutions showed a retardation on the windward side and an advancement on the lee side. However, his model also predicted a tendency for the cold and warm front to be stronger on both the windward and leeward side. This frontal intensification on both windward and leeward sides is not consistent with observations or other research. This may be because the mountain profile was defined as a constant on the geostrophic coordinates, which leads to a time-dependent mountain in physical space after the transformation from the geostrophic coordinates.

Another analytical solution was derived by Davies (1984). He employed a two-dimensional shallow-water system with the semi-geostrophic approximation on a f -plane in which the free surface represented the interface between the cold and warm air. The flow behind the 'cold front' was driven by a reduced gravity, $g' = g/(\theta'/\theta)$ where θ is the potential temperature and θ' is the temperature difference between the two fluids, and by an imposed pressure-gradient force. The characteristics of the flow were determined by a rotational Froude number and a front-mountain aspect ratio. He showed that the semi-geostrophic solution was valid only when the front-mountain aspect ratio was larger than a critical value that depended on the rotational Froude number. His solutions indicated that the progression of the front depended on the frontal strength and steepness as well as the height of the mountain.

Schumann (1987) used an inviscid and adiabatic numerical primitive-equation model with the Boussinesq approximation to examine mountain influences. He performed two- and three-dimensional tests on idealized cold fronts that corresponded to the frontal solution of Davies (1984). His experiments included neutral and stable stratifications. The two-dimensional cases showed a

strong retardation at the foot of the mountain if the Froude number and the relative front-mountain height ratios were small. He also indicated that the front was strongly retarded when the mountain slope was steep in the neutral stratification condition. Hydraulic jumps were found on the leeside when the Froude number was of order one and the mountain was high. The retardation of fronts was further enhanced, but the leeside hydraulic jump was damped, compared with two-layer systems when stable stratification was present. Three-dimensional studies showed that fronts were deformed due to anticyclonic motion of the mean flow around the mountain, and stratification also enhanced the deformation.

Haderlein (1989) also used the shallow-water equations to study cold frontal retardation. He found the characteristics of the frontal retardation were determined by three parameters, the front-mountain aspect ratio H_F/H_B ; the gravitational Froude number $F_g = u_g/(g'H_F)^{1/2}$; and the rotational Froude number $F_r = (fL/(g'H_F))^{1/2}$. In these expressions, H_F and H_B are front and mountain heights respectively, u_g the geostrophic wind, g' is reduced gravity, f the Coriolis parameter and L is the horizontal scale. When the mountain is steep and the gravitational effect dominates, the frontal speed is strongly retarded. There is no retardation when the inertial or rotational effects are dominant.

Zehnder and Bannon (1988) carried out a numerical study of mountain effects on frontogenesis forced by a horizontal deformation field. The semi-geostrophic equations were solved without the coordinate transformation. Compared to the no-mountain frontal solution, they found that the temperature gradient weakened as the front moved up the windward slope due to the divergence of the ageostrophic flow, and strengthened as it moved down on the lee slope due to the convergence of ageostrophic zonal flow. They also found that the front was

about 100 km farther downstream after passing over the mountain ridge than it was in no-mountain case. They explained that the changes in the cold front motion were due to the expansion and contraction of the temperature gradient by the upstream divergence and downstream convergence fields, respectively. The enhanced net motion of the cold front was explained by the effect of the accelerated downstream motion on the leeside .

Another numerical study by Williams *et al.* (1992) used a two-dimensional primitive equation model with the hydrostatic and Boussinesq approximations. The frontal solution was forced by a horizontal deformation field. Their numerical solutions showed reduced frontogenesis on the upwind slope and increased frontogenesis on the lee slope. They explained this behavior in terms of the mountain-forced divergence on the upwind side and convergence on the lee side, which agreed with the solutions of Zehnder and Bannon (1988). They also examined the effects of the mountain horizontal scale on the frontal solution. For a wide mountain, the front behaved more like the semi-geostrophic solution. For the narrow mountain, the frontal structure on the lee side of the mountain was distorted by the gravity waves that were enhanced when the front passed down the lee slope. The increased lee side gravity wave activity may have been due to the increased downslope wind and static stability as the front passed the mountain.

Blumen and Gross (1987a,b) studied a passive scalar in a uniform flow past two- and three-dimensional finite-amplitude ridges. They found frontolysis on the windward slope and frontogenesis on the leeward slope. The passive scalar also experienced deformation in the flow around the mountain in the three-dimensional case due to the anticyclonic flow around the mountain. Blumen (1992) reviewed recent research in this area. He re-examined the frontal evolution in a shallow

water model and in a stratified fluid model. He also showed that a weak front behaves like a passive scalar as it moves over the mountain.

C. SUMMARY AND PROPOSED STUDY

The prior research has provided a picture of a two-dimensional idealized front as it passes over a mountain ridge. From these studies, mountain effects induce frontolysis on the windward side and frontogenesis on the lee side of the mountain. Also, the front experiences a retardation on the upstream slope and an acceleration on the downstream slope. Only a few studies have treated frontal passage over three-dimensional mountains. The idealized front in a uniform flow over the three-dimensional mountain (Schumann 1987; Blumen and Gross 1987b) is distorted by the anticyclonic motion of the mean flow over and around the mountain.

Although these studies have provided some insight into the behavior of a front passing over a mountain, there are some limitations in these prior studies. First, all the flow is forced to pass over the mountain in the two-dimensional model, so that no flow around the mountain was allowed. This causes an over-estimate of the flow that passes over the mountain, and of the effects on the windward side and lee side of the mountain. Second, the idealized front is advected by the mean flow in previous three-dimensional studies, the cold front was influenced only by the mountain modifications on the mean flow rather than on the modifications by the pre- and post-frontal flows.

The objective of this study is to investigate the mountain effects in a three-dimensional frontal system that possesses pre-frontal southwesterly and post-frontal northwesterly flow. We will examine the processes and determine the causes of the frontal distortion by a mountain. The processes of the weakening and the

retardation as well as the strengthening and the acceleration of a cold front during its passage over the mountain will be studied in this three-dimensional frontal system. The effects of different mountain sizes and orientations on a front will also be examined.

The goals of this research are summarized as the follows:

(1) Study the mountain effects on a realistic three-dimensional frontal system and the associated dynamics.

We will use a frontal system that is developed from a baroclinic wave rather than use an idealized cold front. The pre- and post-frontal flows will be retained in this frontal system and they will induce a mountain circulation that is different from the circulation in prior two-dimensional or three-dimensional studies with idealized fronts. This approach will extend our knowledge of topographic influence to three-dimensional mountains with realistic fronts. It is also important to find out the net effects induced by the mountain on the frontal intensity and structure as well as the frontal displacement after the front has moved away from the mountain. These have not been reported by previous analytical and numerical studies.

(2) Generalize the results by including the influences of different mountain circulations on an approaching front.

Pierrehumbert (1984) isolated two important parameters, the Rossby number and Froude number, that determine the characteristics of the flow influenced by a mountain ridge. The Rossby number determines the geostrophy of the induced mountain circulation, while the Froude number determines whether or not the flow has enough momentum to go over the mountain ridge. In a three-dimensional study, the incident angle of an impinging flow and the ratio of the along- to the cross-stream mountain scales are two more factors that affect the

mountain circulation. This study will determine the influence of different mountain sizes, shapes and orientations on the frontal system.

The three-dimensional hydrostatic primitive equation model for a limited area developed at the Naval Research Laboratory that will be used for the present study is described in Chapter II. The mountain solutions for different mountain sizes and shapes are presented and discussed in Chapter III. The frontal solutions generated by the model without the presence of the mountain are discussed in Chapter IV. Chapter V contains the major discussion of frontal systems passing over different mountains and the influences of the mountains on the fronts. Chapter VI concludes with an overview of the study and summary of the results.

II. NUMERICAL MODEL DESCRIPTION

The numerical model used in this three-dimensional study of mountain effects on a frontal system is the Naval Research Laboratory Limited Area Weather Prediction Model (Madala *et al.* 1987). It is a hydrostatic, primitive-equation model with a parameterized boundary layer and cumulus parameterization. However, the moisture and boundary layer treatments will be excluded and x-y coordinates will be used in this study rather than spherical coordinates (Appendix A).

A. NUMERICAL METHOD

The equations are solved by a second-order accurate finite-difference scheme. Arakawa C-grid (Arakawa and Lamb 1977) is used for the horizontal differencing because it is found to be best in simulating the geostrophic adjustment process. In this model, $\sigma = p/p_s$ is used as the vertical coordinate. The vertical domain is divided into 16 layers. Since the largest vertical gradients occur in lower atmosphere, most of the layers are concentrated near the bottom of the model.

The time integration scheme is the split-explicit method, in which the linearized terms in the prognostic equations are separated into the slower moving Rossby modes and the faster gravity modes. These different modes are integrated over different time intervals (Appendix B).

A second-order diffusion scheme with the diffusion coefficient $K = 2.5 \times 10^{-3}$ on the flux terms is included to damp the sub-grid noise. A dry convective adjustment is used in the model to prevent static instability.

B. INITIAL AND BOUNDARY CONDITIONS

We will use this model to probe the frontogenesis process, the mountain influence on an impinging flow, and then on the approaching front. The

frontogenesis will be initiated in a baroclinic basic state with a horizontal wind shear. The most unstable mode of the Eady wave will be used as the initial disturbance for the frontogenesis model.

The lateral boundary conditions vary in different experiments. For the mountain solution experiments, a fixed boundary condition is employed. The inflow and outflow are kept constant on the east-west boundaries, and no flow is allowed across the north-south boundary. In the frontogenesis experiment, a cyclic boundary condition is used on the east-west boundaries. In the combined front and mountain experiment, the upstream boundary is updated with data from the frontogenesis experiment by using the blending method (Perkey and Kreitzberg 1976).

III. MOUNTAIN SOLUTION

Before we study the effect of mountains on fronts, it is necessary to understand the mountain circulation under various conditions. Mountains may induce various phenomena as the air passes over and around them. The occurrence of these phenomena depends largely on the following parameters: the Froude number ($Fr = U/Nh$), the Rossby number ($Ro = U/fL$) and the horizontal aspect ratio of the mountain. In the large Fr limit, Queney (1947, 1948) obtained linear wave solutions for bell-shaped mountains for a uniform flow and uniform vertical stability. In the small Fr limit, Drazin (1960) obtained solutions for potential flows.

When the Rossby number is much less than unity, the flow can be described by quasi-geostrophic theory (Buzzi and Tibaldi 1977, Smith 1979a, b). An anticyclonic is formed over the mountain by the conservation of potential vorticity. Therefore, maximum velocity is found on the left and minimum velocity is found on the right of the mountain. The vertical velocity field has an upward motion on the windward side and downward motion on the lee side. When the air parcel approaches the foothills of the mountain, it is first vertically stretched slightly which produces a weak cyclonic vorticity. As it passes over the mountain, the column is shortened, which generates an anticyclonic vorticity. When it moves down on the lee side, the air parcel is stretched and produces a cyclonic vorticity again.

For mesoscale mountains, the Rossby number is no longer small. Pierrehumbert (1984) obtained a Green's function solution for Queney's model. The asymptotic and numerical analysis showed that the upstream deceleration can be estimated as a function of Ro and $\underline{h}_m = NH_m/U$, where U is the far upstream flow, N the Brunt-Vaisala frequency and H_m is the maximum mountain height. For

the barrier effects of a mesoscale mountain, he concludes that preserving the maximum height is superior to preserving an integrated quantity of the mountain (such as mountain volume). Somieski (1981) studied the linear response of three-dimensional flow over mesoscale mountains. He presented a quasi-geostrophic flow around a large-scale (500 km) mountain and also a highly ageostrophic flow around the mountain when the mountain size was reduced to 50 km.

Relatively fewer efforts have been devoted to baroclinic flows over the mountains. Bannon and Zehnder (1989) derived and discussed the steady-state mountain circulation in detail in the semi-geostrophic framework. For the geostrophic part of the flow, the isentropes are convex for forward shear. Compared to a uniform velocity flow, both the static stability and the anticyclonic vortex are weaker in the forward shear case. This is due to the horizontal temperature gradient because the northward flow on the upslope side produces warm air advection that partially compensates the adiabatic cooling by the forced ascent. For the ageostrophic part of the flow, there was rising motion upstream of the mountain, an ageostrophic wind over the mountain, and sinking motion downstream.

The baroclinic flows over mesoscale and three-dimensional mountains have not been studied and are needed for the present frontal study. They are presented in the results of this chapter. To compare our results with previous studies, we also treat some uniform flows over our mountains.

A. UNIFORM FLOW

The mountain profile in this study (Fig. 3.1) follows Smith (1979a, 1980), with a modification to two dimensions:

$$h(x,y) = H_m / (x^2/a_{0x}^2 + y^2/a_{0y}^2 + 1)^{3/2}, \quad (3.1)$$

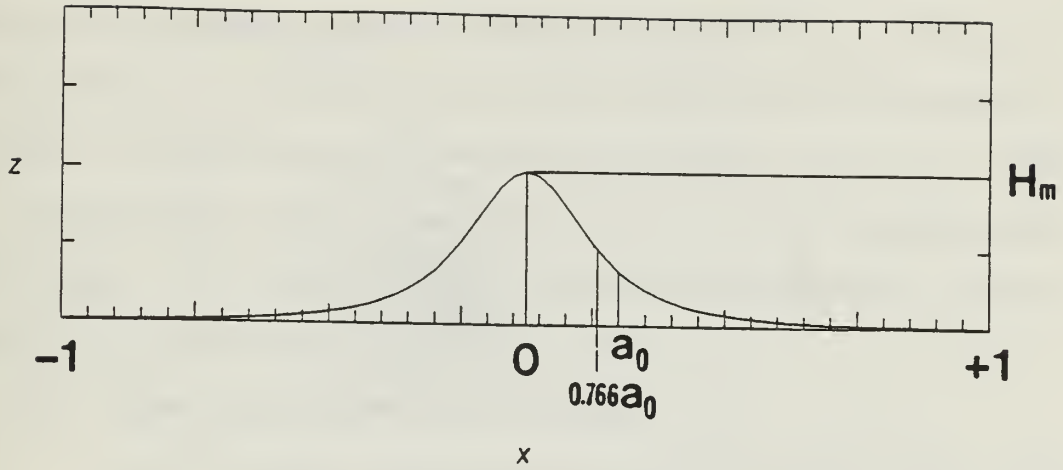


Fig. 3.1 The vertical profile of the mountain $h(x,y) = H_m / (x^2/a_{0x}^2 + y^2/a_{0y}^2 + 1)^{3/2}$, along the zonal (x) direction.

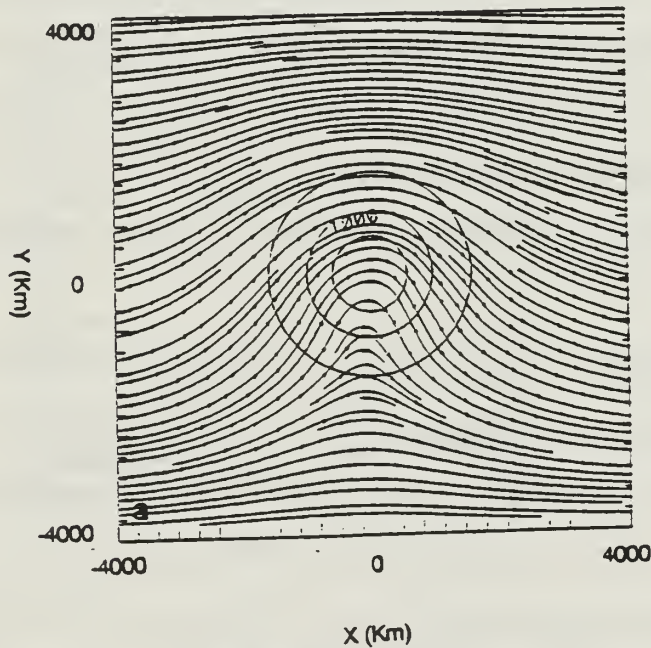


Fig. 3.2 Mountain solutions for uniform flow over a large-scale circular mountain at $t = 48$ h: (a) Streamlines at $\sigma = 0.9975$; (b) Vertical velocity (ω) with contour interval = 0.7 mb/h and upward (downward) motion in dashed (solid) lines; and (c) Vertical profile ($0-8$ km) of the potential temperature ($^{\circ}$ K) along an east-west cross-section passing through the mountain

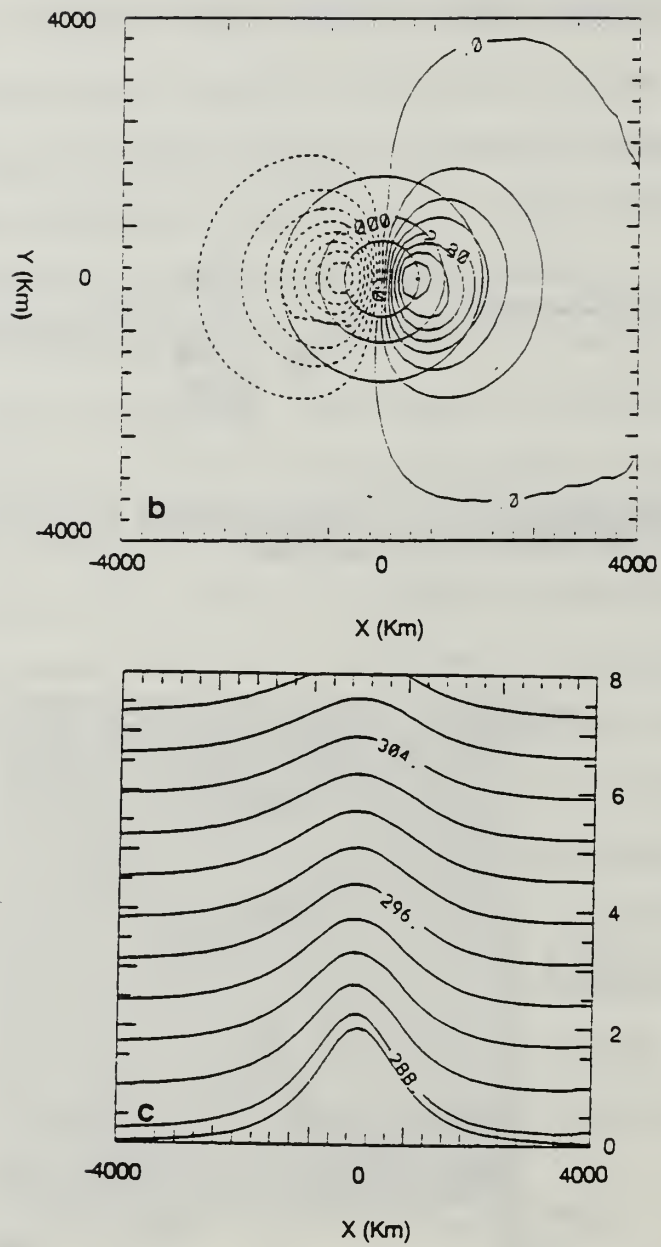


Fig. 3.2 (Continued)

where H_m is the maximum mountain height, a_{0x} the mountain scale in the x direction and a_{0y} is the mountain scale in the y direction. When $a_{0x} = a_{0y}$, the mountain is a circular mountain. We also define the horizontal aspect ratio of the mountain as $\beta = a_{0x}/a_{0y}$. Circular mountains will have the horizontal aspect ratio $\beta = 1$. When $\beta > 1$, the topography is east-west oriented. When $\beta < 1$, the topography is north-south oriented. The Rossby number for the mountain circulation is defined as $Ro = U/f a_{0x}$, and the Froude number is $Fr = U/NH_m$.

1. Flow over Large-scale Mountains

When the scale of the mountain is large and the flow speed is small, the Rossby number is much smaller than unity, and the flow is described by the quasi-geostrophic equations. To compare the results from the current numerical model with the quasi-geostrophic solution, the parameters are chosen as follows: the horizontal scale of the mountain $a_{0x} = a_{0y} = 1120$ km, the maximum mountain height $H_m = 2000$ m, uniform flow $U = 10$ m/s, Coriolis parameter $f = 1.0 \times 10^{-4} \text{ sec}^{-1}$ and $N = 0.01 \text{ sec}^{-1}$. The grid resolution is 160 km for this large-scale mountain case. The Rossby number Ro is equal to 0.089 and the Froude number Fr is equal to 0.5.

On the lowest model level ($\sigma = 0.9975$), the streamlines (Fig. 3.2a) have an anticyclonic curvature over the mountain. The vertical velocity (ω) on the lowest level of the model is upward on the windward side and downward on the leeside (Fig. 3.2b). The extremes of vertical motion occur on the slopes of the mountain. The vertical displacement of the isentropic surfaces decreases with height, but the horizontal extent of the perturbation increases (Fig. 3.2c). These results are the same as the previous quasi-geostrophic mountain solutions of Smith (1979b, 1982).

2. Mesoscale Flow Response

In the second experiment, the characteristic scales a_{0x} and a_{0y} of the mountain are 240 km. The upstream flow is 10 m/s, and H_m is 2000 m. The Coriolis parameter and the Brunt-Vaisala frequency are always the same in these experiments. The Froude number is 0.5, which is the same as in the previous quasi-geostrophic case, while the Rossby number is 0.42, which is much larger than the previous case. For this increased Rossby number, the flow field no longer satisfies the quasi-geostrophic approximation. The mountain-induced anticyclonic circulation is shifted downstream to the lee side slope of the mountain and a trough is generated on the lee side (Fig. 3.3a). The orientations of the ridge and trough are from northeast to southwest. This lee side trough, which is associated with the gravity wave shown in the isentropic surfaces, has an upstream tilt and its magnitude decreases with height (Fig. 3.3b). The ageostrophic flow is comparable to or larger than the geostrophic part of the flow (not shown). The anticyclonic circulation around the mountain is dominated by the ageostrophic flow.

When compared to the large-scale mountain circulation, the mesoscale mountain circulation has a significant ageostrophic flow on the leeside of the mountain and a lee side trough is generated.

B. BAROCLINIC FLOW

1. Large-scale Mountain

The flow response to a large-scale mountain for a baroclinic flow is different from the uniform flow case. The wind speed at the surface is 5 m/s, and a constant vertical wind shear of $2.5 \times 10^{-3} \text{ sec}^{-1}$ is imposed throughout the troposphere. The maximum mountain height is 2000 m and the mountain scale is 640 km.

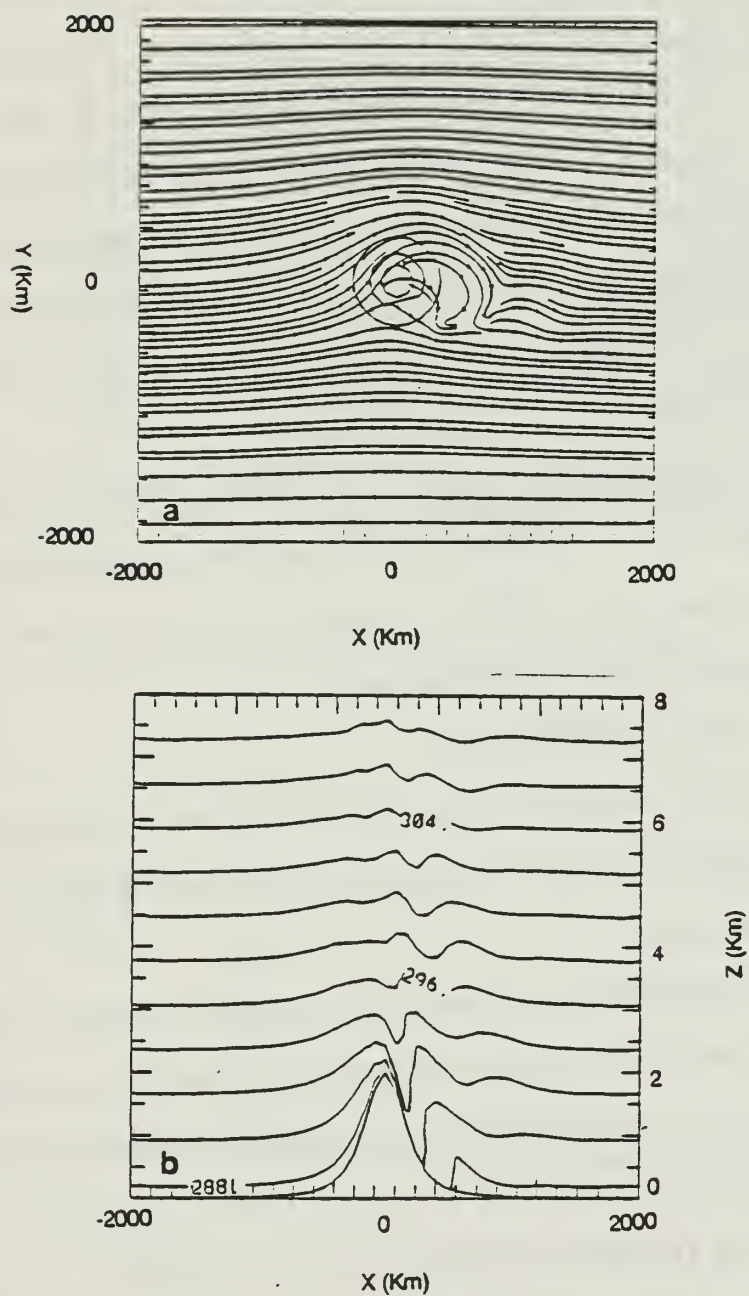


Fig. 3.3 Mountain solutions as in Fig. 3.2(a) and (c) except over a mesoscale circular mountain.

The most significant phenomena in the baroclinic flow over the mountain is the excitation of an unstable wave on the leeside that moves downstream. The anticyclonic circulation (Fig. 3.4a) over the mountain is weaker than in the uniform flow. The vertical profile of the potential temperature field shows that the isentropic surface is no longer along the topographic surface, since the mountain penetrates up through the isentropic surfaces (Fig. 3.4b). The downstream-moving leeside trough can also be seen in the vertical potential temperature profile.

As discussed by Bannon and Zehnder (1989) for the semi-geostrophic solution, the maximum anticyclonic circulation over the mountain is less in the baroclinic flow than in the uniform flow due to the warm advection that reduces the pressure in the vicinity of the mountain top.

2. Mesoscale Mountain

Flow with linear vertical wind shear over a mesoscale mountain is studied in this experiment. The mountain size $a_{0x} = a_{0y} = 240$ km is the same as in the uniform flow case.

An anticyclonic flow and an associated downstream cyclonic flow are also present in this case (Fig. 3.5a). However, these flows are weaker than they are in the uniform flow case. The vertical potential temperature cross-section has gravity waves that are more amplified at the upper levels (Fig. 3.5b).

C. EFFECTS OF HORIZONTAL ASPECT RATIO

The effect of the mountain height is included in the Froude number, which determines whether or not the flow has enough energy to climb over the mountain. The effect of horizontal mountain scale is included in the Rossby number, which is used to estimate the geostrophy of the flow response. When the mountain is not circular, a new scale is introduced into the system.

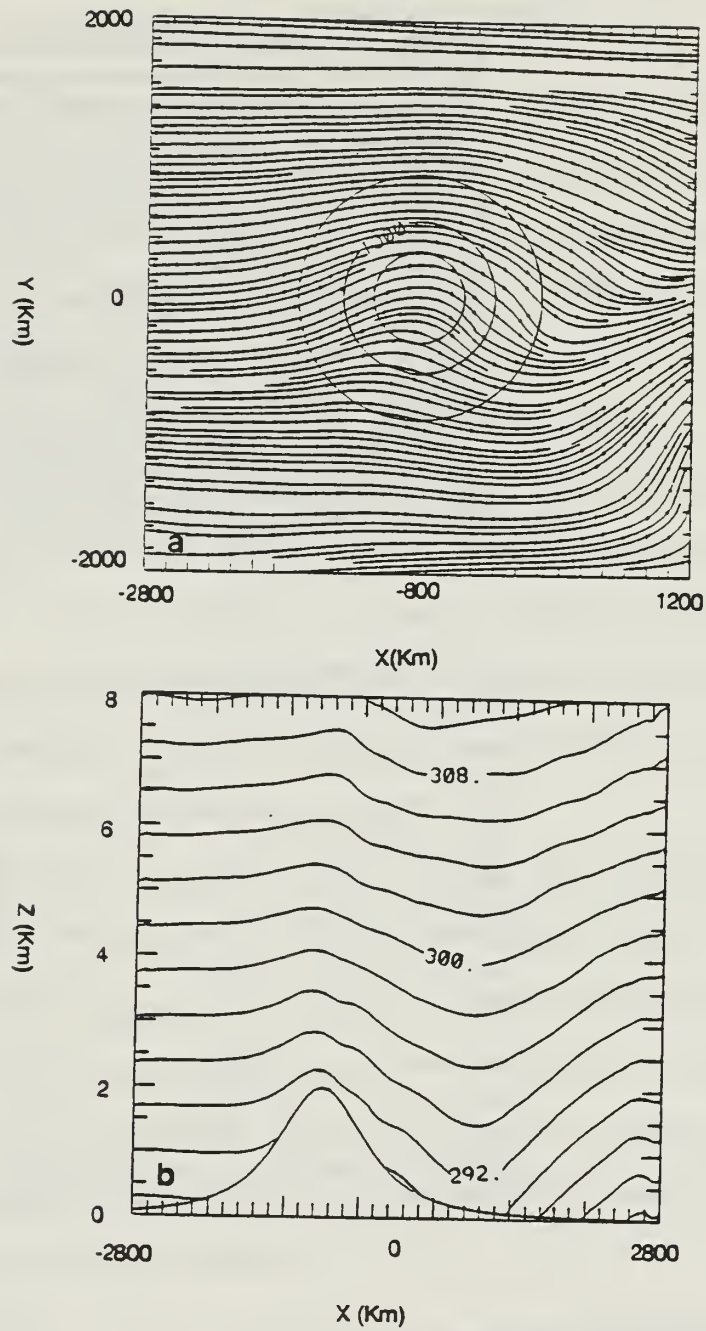


Fig. 3.4 Mountain solutions as in Fig. 3.2(a) and (c) except for a baroclinic flow over a large-scale circular mountain at $t = 72$ h.

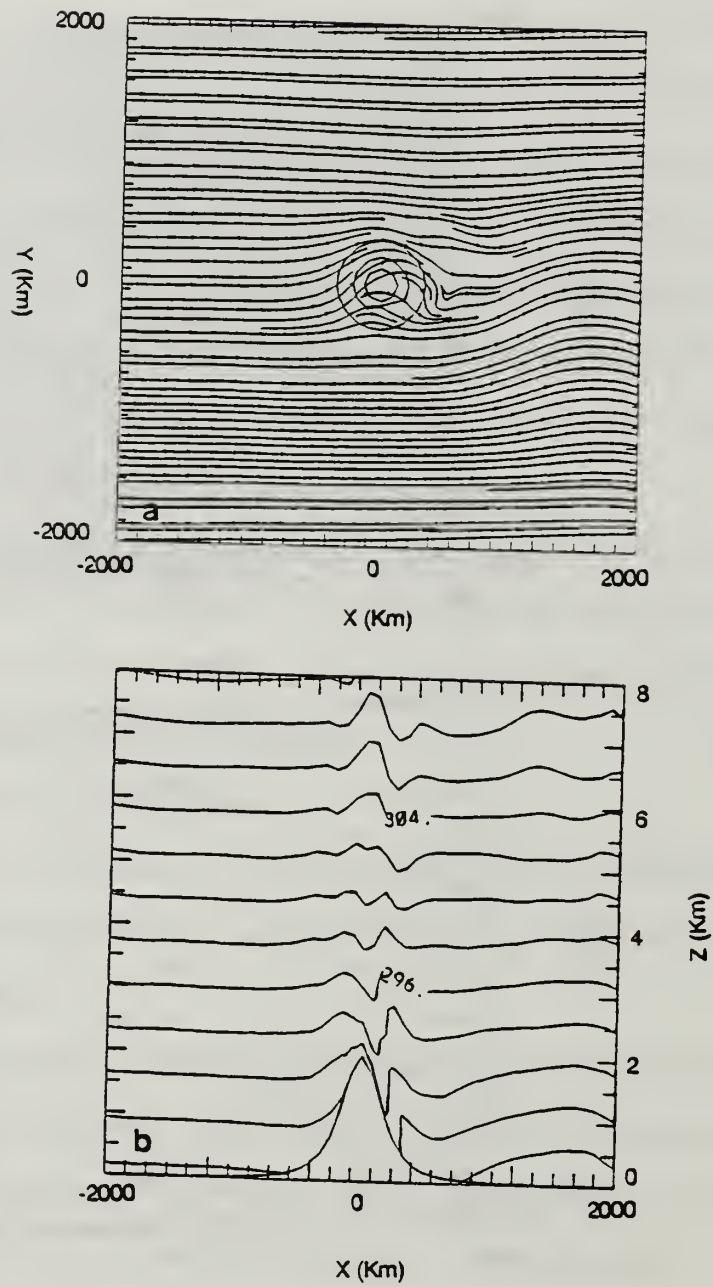


Fig. 3.5 Mountain solutions as in Fig. 3.2(a) and (c) except for a baroclinic flow over a mesoscale circular mountain at $t = 48$ h.

When $a_{0x} = 720$ km and $a_{0y} = 240$ km (i.e., $\beta = 1/3$), the mountain is east-west oriented. With a uniform basic flow $U = 10$ m/s, the flow (Fig. 3.6a) is similar to a quasi-geostrophic system because the mountain scale in the direction of the mean flow is large. The induced anticyclonic flow experiences the north-south mountain scale, which is only 240 km, and produces the significant ageostrophic motion (Fig. 3.6b). The vertical potential temperature profile in Fig. 3.6c shows only weak gravity waves are generated on the leeside.

When $a_{0x} < a_{0y}$, the mountain is north-south oriented. With $a_{0x} = 240$ km and $a_{0y} = 720$ km, (i.e., $\beta = 3$), the mountain circulation at $t = 48$ h with the same initial uniform flow $U = 10$ m/s is shown in Fig. 3.7a. The major feature is a lee-side trough. The potential temperature cross-section (Fig. 3.7b) shows a gravity wave on the lee side. This indicates that there is more flow over the mountain in this mountain orientation compared to the previous case as the gravity wave is generated by the stronger flow over the mountain.

The flow field with a vertical shear over the same north-south oriented mountain is shown in Fig. 3.8. The basic flow at the bottom is equal to 10 m/s and the vertical wind shear is equal to $2.5 \times 10^{-3} \text{ sec}^{-1}$. As in the previous case for the uniform flow, a strong lee-side trough associated with a gravity wave is generated. This lee-side gravity wave is shown more clearly by the divergence field. This divergence field is the key mechanism for explaining the mountain effects on the front as will be seen in Chapter V.

D. SUMMARY

The mountain solutions in this chapter present results that are compatible with earlier studies of large- and meso-scale circular mountains. Flows over large-scale mountains generate circulations that are described by the quasi-geostrophic

theory. Anticyclonic vorticity is induced over the mountain and the flow response is almost symmetric about the axis of the mountain. For mesoscale mountains, lee-side gravity waves are generated and the flows are asymmetric to the mountain axis. The ageostrophic flow is dominant in the around-mountain anticyclonic flow, which is located on the downslope of the mountain. A lee-side trough is also present downstream from the anticyclonic ridge.

Although the flow response to an elliptical-shaped mountain is determined primarily by the mountain scale that is parallel to the impinging flow, it is modified by the cross-flow mountain scale. An east-west oriented mountain, which has a large-scale in x -direction and a mesoscale in y -direction, induces a quasi-geostrophic anticyclonic circulation primarily. This anticyclonic circulation is modified by the mesoscale a_{0y} and produces a quadrant pattern in the vertical velocity field. A north-south oriented mountain, which has a mesoscale mountain size in the x -direction, produces an ageostrophic wind on the leeside. Due to the north-south extent of the mountain, most of the flow is forced over the mountain. These results are more similar to the two-dimensional experiments. With vertical wind shear, the mountain-induced circulation is weaker than the circulation that is induced in a uniform flow.

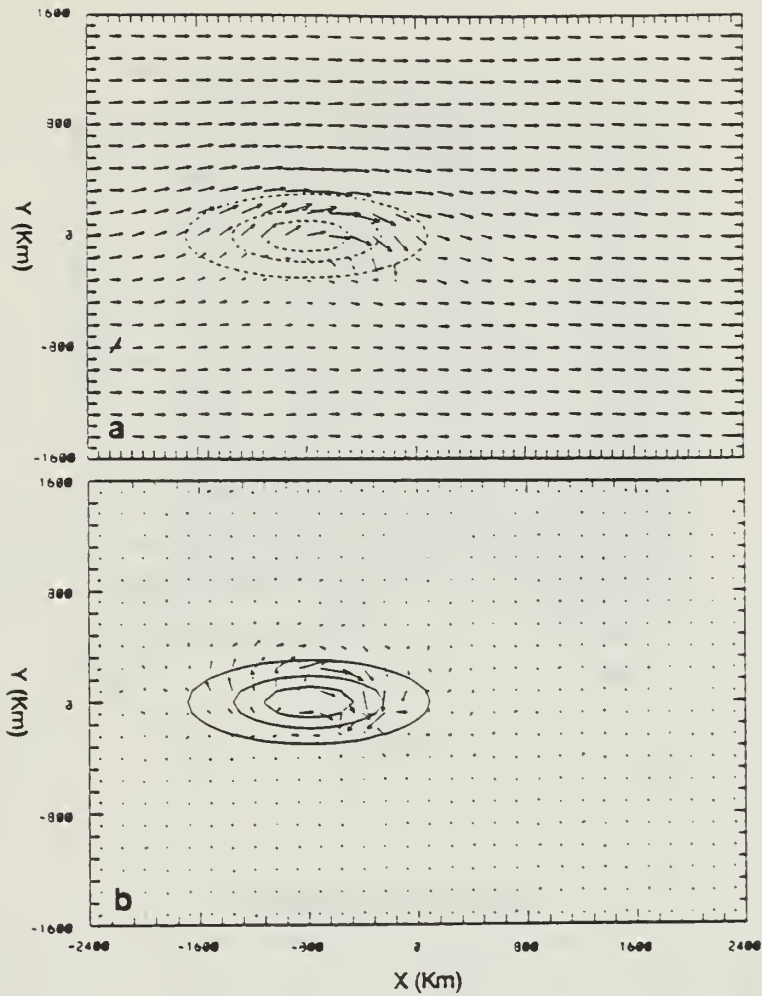


Fig. 3.6 Mountain solutions for an uniform flow over the east-west oriented elliptical mountain at $t = 48$ h: (a) geostrophic wind on $\sigma = 0.9975$; (b) ageostrophic wind on $\sigma = 0.9975$; (c) Vertical profile (0 to 8 km) of potential temperature ($^{\circ}$ K) along an east-west cross-section through the mountain.

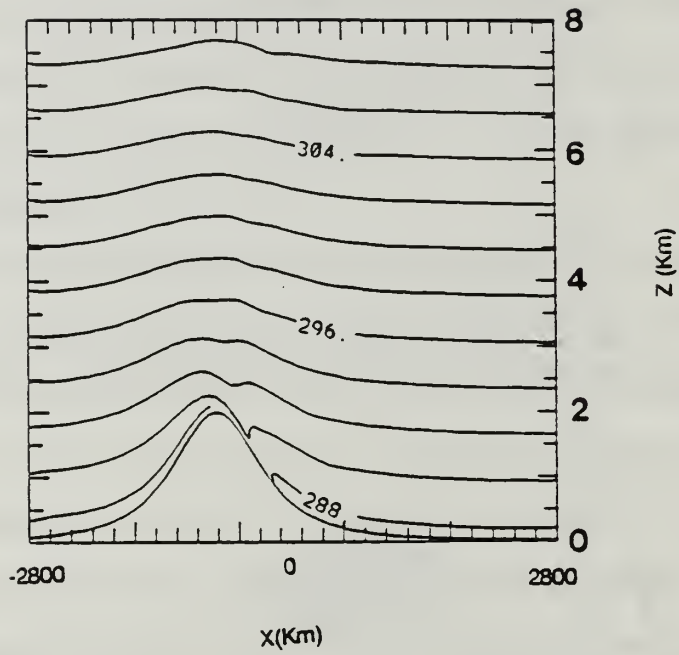


Fig. 3.6 (Continued)

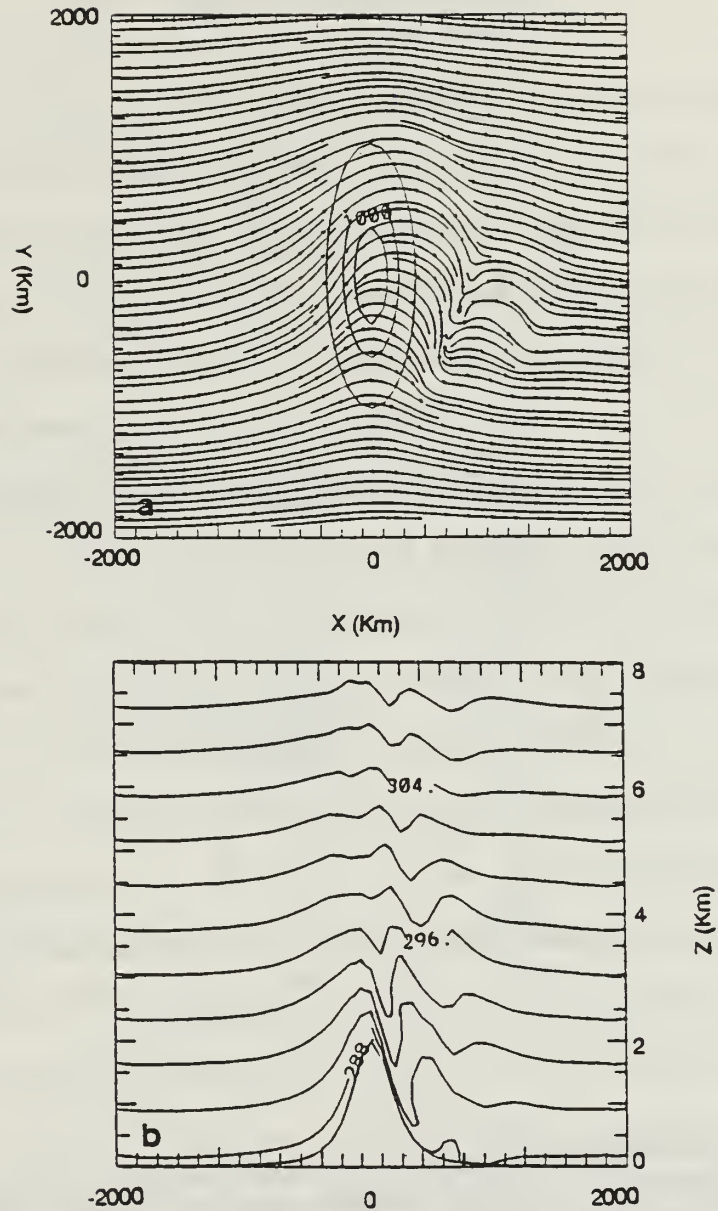


Fig. 3.7 Mountain solutions for a uniform flow over a north-south oriented mountain at $t = 48$ h: (a) Streamlines on $\sigma = 0.9975$; (b) Vertical profile (0 to 8 km) of potential temperature ($^{\circ}$ K) along an east-west cross-section through the mountain.

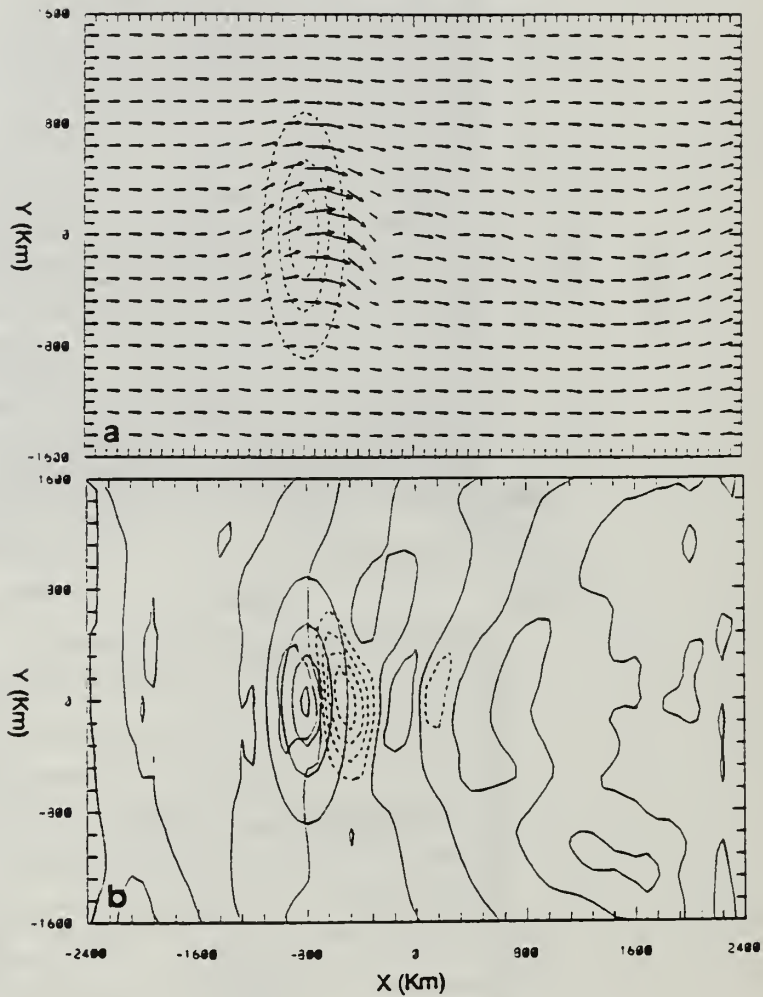


Fig. 3.8 Mountain solutions for a baroclinic flow over a north-south oriented mountain at $t = 72\text{h}$: (a) surface wind vectors with a maximum of 25 m/s ; and (b) divergence field for the surface wind, contour interval $0.2 \times 10^{-4} \text{ s}^{-1}$ with positive (negative) values in dashed (solid) lines.

IV. FRONTAL SOLUTION

The frontal system is a very special phenomena in the atmosphere. It extends up to 4000 km in one (along-front) direction and can have a small-scale dimension of 100 km or less in the cross-front direction. Thus, the frontal system is characterized by a large length scale in the along-front direction and a much smaller length scale in the cross-front direction. This anisotropic property of fronts allows the use of two-dimensional models for frontal studies.

Many theoretical studies of fronts have been made (Stone 1966, Williams 1967, Williams and Plotkin 1968, Hoskins and Bretherton 1972, Hoskins 1975). These studies indicate that the fronts can be simulated by semi-geostrophic theory. The semi-geostrophic equations have been used widely in the last two decades in the studies of fronts or flows over mountains. Recently, Synder *et al.* (1991) did a comparison between a primitive-equation model and a semi-geostrophic model for baroclinic frontal development. They found that the primitive-equation simulation had a distinctively different structure than the semi-geostrophic simulation in the mature frontal stage. The semi-geostrophic model always produced a symmetric structure in the across-front direction and it did not occlude, while the primitive-equation model was able to capture the cyclonic wrapping of isotherms and a bent-back frontal structure at the surface. They indicated that the semi-geostrophic model errors arose in the treatment of terms involving the ageostrophic vorticity.

Miller (1948) defined and derived the intensity of frontogenesis as the time-rate of change of the gradient of a scalar property, e.g., potential temperature. This definition was used by many researchers (Reed and Sanders 1953; Sanders 1955 and Bosart 1970) to study the structure of frontal systems. Following Miller's definition,

the intensity of the frontogenesis can be defined as the time-rate change of the horizontal temperature gradient of an air parcel in x,y,p space,

$$\begin{aligned}
 d(|\nabla\theta|)/dt = |\nabla\theta|^{-1} \{ & -[(\partial\theta/\partial x)^2 (\partial u/\partial x) + (\partial\theta/\partial y)^2 (\partial v/\partial y)] \\
 & -[(\partial\theta/\partial x)(\partial\theta/\partial y)(\partial v/\partial x + \partial u/\partial y)] \\
 & -[(\partial\theta/\partial x)(\partial\theta/\partial p)(\partial\omega/\partial x) + (\partial\theta/\partial y)(\partial\theta/\partial p)(\partial\omega/\partial y)] \\
 & -[(\partial\theta/\partial x)\partial(d\theta/dt)/\partial x) + ((\partial\theta/\partial x)\partial(d\theta/dt)/\partial x)] \}
 \end{aligned}
 \tag{4.1}$$

The last group on the right side of (4.1) gives the diabatic effect, which we have excluded in this study.

The first group on the right side of (4.1) represents the confluent or diffluent effect in a stretching deformation field, in which the cold air and warm air are advected toward each other. In a midlatitude cyclone frontogenesis, the stretching deformation is a leading term in the formation of the warm front (Hoskins and Bretherton 1972).

The second group on the right side of (4.1) describes the effects of shear deformation. This term is important in the cold frontogenesis in a midlatitude cyclone, where cold air is to the northwest and warm air is to the southeast ($\partial\theta/\partial x > 0, \partial\theta/\partial y < 0$, while the wind field has a cyclonic curvature ($\partial v/\partial x > 0, \partial u/\partial y < 0$). In the trough area, this effect has a positive contribution to the frontogenesis of the cold front in the midlatitude cyclone, $-(\partial v/\partial x)(\partial\theta/\partial y) > 0$. In a three-dimensional analysis, the vertical shearing terms, $(\partial u/\partial p)(\partial\theta/\partial x)(\partial\theta/\partial p) + (\partial v/\partial p)(\partial\theta/\partial y)(\partial\theta/\partial p)$, may be included. In geostrophic motion, the sum of these two terms vanishes, which can be shown with the thermal wind relationship. Thus, the contribution of the vertical shearing terms comes from the ageostrophic motion.

terms represent an isentropic warming or cooling due to the horizontal gradient of the vertical motion, such as in a cross-frontal vertical motion pattern.

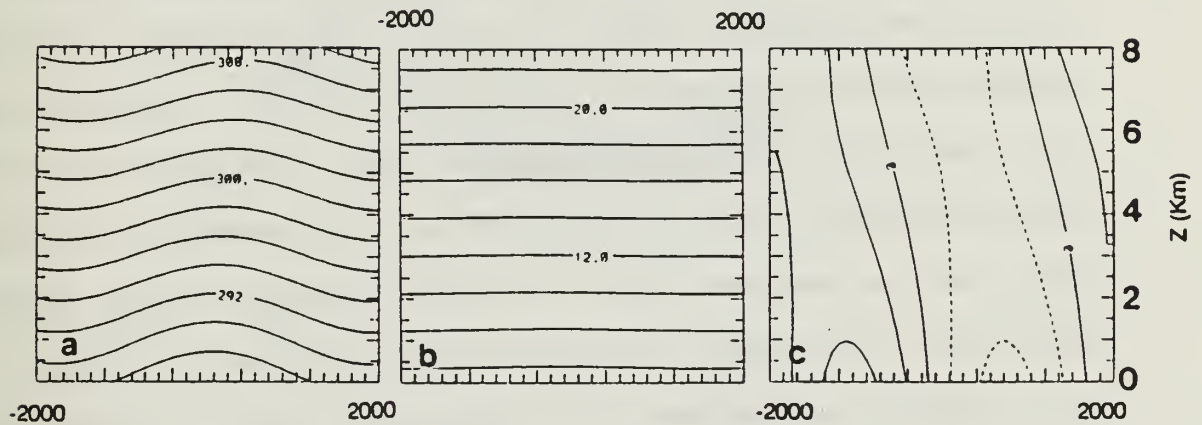


Fig. 4.1 Vertical profile of the initial condition along an east-west cross-section in the middle of the domain for the frontogenesis process: (a) potential temperature ($^{\circ}\text{K}$); (b) u , with contour interval of 2 m/s; and (c) v' , with contour interval is 2 m/s, and positive (negative) values in solid (dashed) lines

A. BAROCLINIC FRONTOGENESIS

In this section, we will present the frontal solution generated by baroclinic instability in our three-dimensional primitive-equation model with no mountains. The grid size of the numerical model is 80 km in a model domain of 4000 km with 51 gridpoints in each direction. The time step of integration is 200 seconds.

1. Initial Conditions

The basic state of the initial field has a vertical wind shear that is constant in the troposphere (0.0025 s^{-1}) and zero in the stratosphere. The initial horizontal temperature gradient is in thermal wind balance with the vertical wind shear. The horizontal wind has a cosine square structure as in Synder *et al.* (1991). The disturbance part contains the quasi-geostrophic Eady wave that has the largest linear growth rate corresponding to the prescribed basic state, with the horizontal shear excluded. The vertical cross-section of the initial potential temperature and the u-component and v-component wind fields are given in Fig. 4.1. Note that the v-component has a disturbance part only. To allow the disturbance to develop, cyclic boundary conditions are applied in the east-west direction.

2. Evolution of a Frontal System

By $t = 96 \text{ h}$, the front is well developed (Fig. 4.2). The warm front is oriented in the east-west direction ahead of the low due to the horizontal shear of the basic flow. The cold front is oriented more in the north-south direction and extends from the cyclone center. The wind field (Fig. 4.2b) has northward pre-frontal winds and post-frontal northwesterlies behind the cold front. This frontal structure is similar to the one in Hoskins (1976) and Synder *et al.* (1991).

A d-value for a two-dimensional model was defined by Williams *et al.* (1992) to measure the frontal intensity,

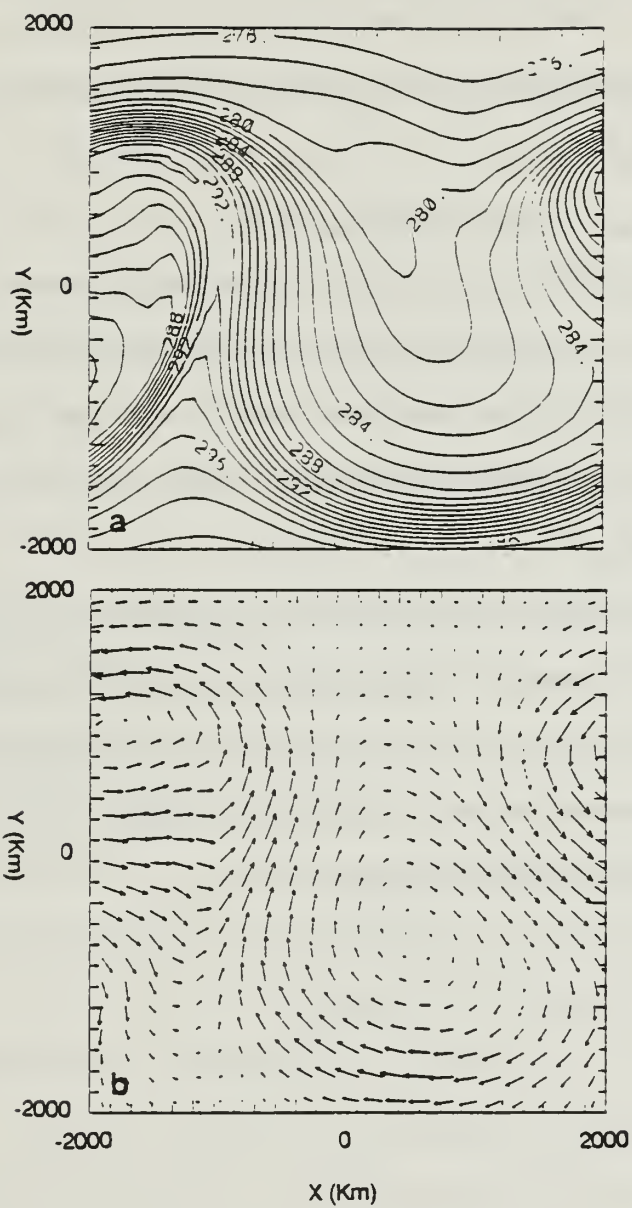


Fig. 4.2 Frontal system on the sea-level surface at $t = 96$ h: (a) potential temperature ($^{\circ}\text{K}$); and (b) wind vectors with maximum of 29 m/s.

$$d = |\Delta_x \theta| / \max |\partial \theta / \partial x|, \quad (4.2)$$

where the $\Delta_x \theta$ is the maximum east-west temperature difference in the initial state. In the three-dimensional frontogenesis case, we modify this definition to include the variation in the y-direction.

$$d = |\Delta_y \theta| / [(\partial \theta / \partial x)^2 + (\partial \theta / \partial y)^2]^{1/2}, \quad (4.3)$$

where $\Delta_y \theta$ is the maximum north-south temperature difference in the initial state, and $\partial \theta / \partial x$ and $\partial \theta / \partial y$ are the local temperature gradients. The d-value is a measure of the minimum frontal scale, and along with the vorticity field, will be used to describe the frontal variations when the system passes over mountains.

B. SUMMARY

Frontogenesis due to a baroclinic wave has been intensively studied during the past decades. It presents a realistic frontal structure with a southwesterly flow and northwesterly in the pre-frontal and post-frontal areas, respectively. The frontal system that is developed by this frontogenesis process will be used in the next chapter for studying the mountain influences on it.

V. INFLUENCE OF MOUNTAINS ON A FRONTAL SYSTEM

As reviewed in the introduction, the mountain influences on a frontal system have been studied by many researchers (Bannon 1983, 1984b; Davies 1984; Schumann 1987; Zehnder and Bannon 1988; Blumen and Gross 1987a; Williams *et al.* 1992). However, most of these works focused on two-dimensional investigations (Bannon 1983, 1984; Davies 1984; Zehnder and Bannon 1988; Williams *et al.* 1992) or used an idealized front (Davies 1984; Schumann 1987; Blumen and Gross 1987). Schumann (1987) discussed briefly the three-dimensional effects and concentrated on the retardation and acceleration of the front. Blumen (1992) used a shallow-water solution for three-dimensional mountains to show that the front is accelerated on the northern side of the mountain and retarded on the southern side, mainly by the mountain-induced anticyclonic flow.

In our three-dimensional model, variations in the y direction are allowed, and the impinging flow is not confined to be y -independent. When a frontal system approaches the mountain, the impinging flow to the mountain is no longer the mean western flow, but is the wind associated with the frontal circulation. The direction of an impinging flow determines the upstream and downstream sides of the mountain. A realistic cold front has a southerly flow ahead of and a northwesterly flow behind the frontal zone. This property can induce two different mountain circulations, one ahead and the other behind the frontal wind shear as the cold front moves over the mountain ridge. In this chapter, we will see that these frontal-induced mountain circulations play the major role in modifying the frontal structure.

As discussed in Chapter III, the mountain circulation is controlled by the Rossby number and the Froude number (Pierrehumbert 1984), which are

determined by the mountain size, mountain height, and the characteristics of an impinging flow. Because of the large wind speed associated with a frontal system, the Froude number becomes large. For example, Fr is equal to 1.0 for an average wind speed associated with the front with $U = 20 \text{ m/s}$, mountain height $h_m = 2000 \text{ m}$ and Brunt-Vaisala frequency $N = 0.01 \text{ s}^{-1}$. Flow with this value of Fr will have enough momentum to pass over the mountain. However, the incident angle of the flow and the shape of the mountain will also introduce other time-dependent factors in the flow responses.

The mountain influences on an approaching front are studied in this research with different mountain sizes and different mountain orientations. The former determines the characteristic length scale of the response flow and controls the Rossby number. The latter changes the front-mountain crossing angle. To reduce the degrees of freedom, the mountain height is kept the same for all cases.

A. INTRODUCTION OF A FRONTAL SYSTEM INTO A NEW DOMAIN

Before introducing a frontal system into a model domain containing a mountain, the front is formed first in a baroclinic environment as described in Chapter IV. A time-dependent lateral boundary condition treatment (Perkey and Kreitzberg 1976) is used to introduce the developed frontal system into the new domain that contains the mountain. Some noise may occur near the warm front area where a net outflow occurs that may lead to a boundary instability. This problem does not occur in the cold front region because there is only inflow. We apply damping in the warm front area and will concentrate our attention on the cold front.

1. Boundary Condition Treatment

Perkey and Kreitzberg (1976) developed a time-dependent lateral boundary scheme for limited-area, primitive-equation models. This tendency blending method mixes the tendency of the outer domain model and the tendency of the inner domain model by using a linear weighting factor near the lateral boundary. In our study, the tendency in the upstream lateral boundary of the mountain model is updated with the boundary values saved every hour from the front-only experiment. We overlap five grid points in the upstream lateral boundary,

$$\text{Tend}(I) = W(I) * \text{Tend}_m(I) + (1.0 - W(I)) * \text{Tend}_f(I),$$

where $\text{Tend}(I)$ is the new tendency for each variable at the grid point I , $\text{Tend}_m(I)$ is the tendency of the current model containing the mountain, and the $\text{Tend}_f(I)$ is the tendency during the frontogenesis process. $W(I)$ is the weighting coefficient at the mass point defined as $W(I) = 0.2 * (I - 1)$, $I < 6$, i.e. $W(I)$ will be 0.0, 0.2, 0.4, 0.6, 0.8 at the five upstream boundary columns. Since the grid points are on the Arakawa C-grid, the grid position of variables u, v are staggered from the mass point. An interpolation of the weighting coefficient is used for the u and v points.

The tendency Tend_f is kept constant during each hour and updated every hour. Since the mountain height is nearly zero at the boundary, this blending procedure can be carried out on the sigma coordinates.

Zero tendency is imposed on the north, south and the east lateral boundaries, which causes some small amplitude noise due to the reflection of outgoing waves. However, the noise will not affect the results in the center part of the domain during a limited period of integration.

2. Frontal Structure in The New Domain

The migration of the frontal system into the new domain described above might reduce the intensity of the front slightly due to the boundary damping. To have a clear comparison of the frontal system with and without the mountain, the frontal structure in the new domain without a mountain is examined. The d -value on the lowest level of the model every 6 h are shown in Fig. 5.1, which gives intensities and positions of the front. Fig. 5.2a is the potential temperature at sea level after 54 h integration in the new domain without the mountain. The warm front is not far ahead of the cold front since the boundary is right ahead of the cold front and thus the domain contains only a small portion of the warm front. The surface wind field in Fig. 5.2b shows that the frontal wind shear has been retained, although it has been weakened. Cold front positions (Fig. 5.3) sketched from the calculated d -values in Fig. 5.1 indicate a steady eastward motion. The speed of the frontal movement is roughly 12.5 m/s. This diagram will be compared later with the frontal positions in the presence of the mountains.

B. EXPERIMENTAL APPROACH

1. Mountain Structure and Model Configuration

The mountain profile in this study is the same as in Chapter III, which is the Smith (1980) mountain profile. To prevent the formation of a transient leeside trough by an initial impulsive flow, the maximum mountain height is increased slowly in the first 24 h of integration by using the following formula:

$$\underline{h}_m(t) = H_m \sin^2(t\pi/48), \quad t < 24 \text{ h}, \quad (5.1)$$

where H_m is the final maximum mountain height, and $\underline{h}_m(t)$ is the maximum mountain height at time t . The size of the mountain is varied by changing the a_{0x}

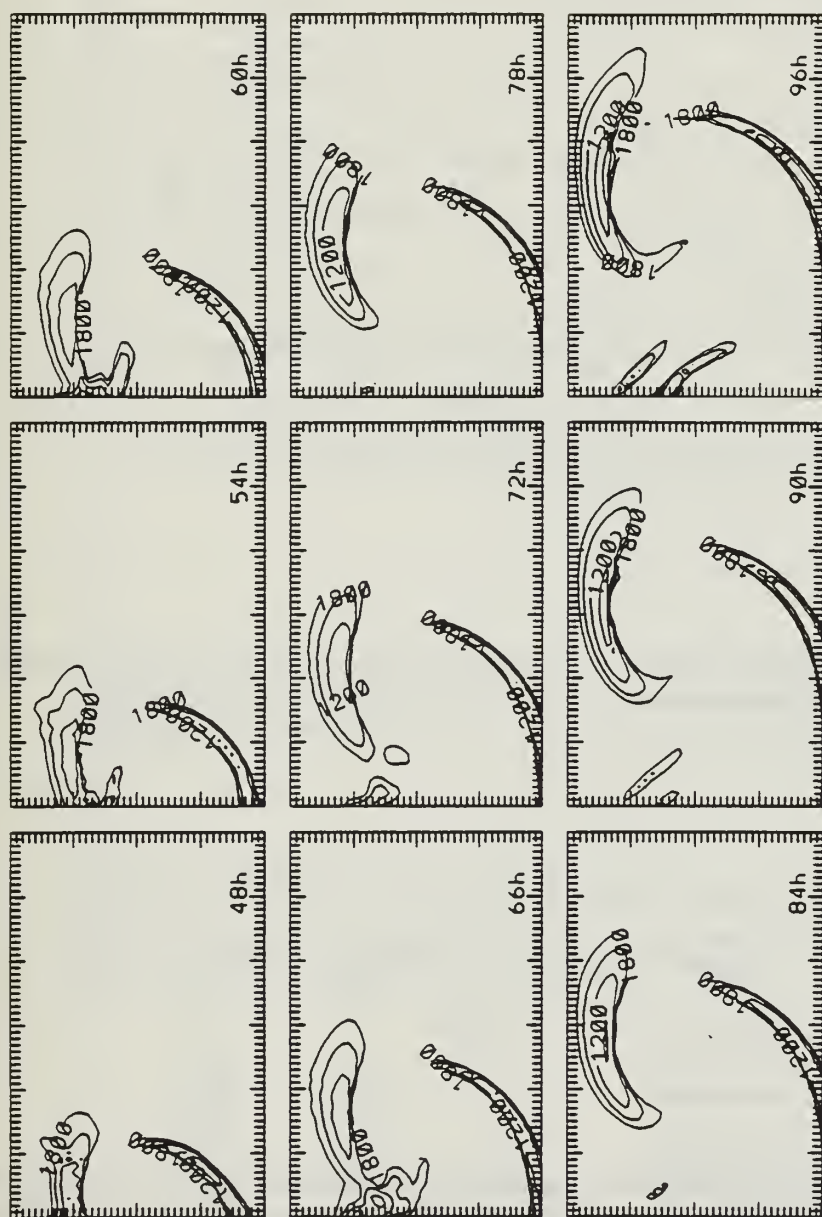


Fig. 5.1 Time evolution each 6 h, from 48 h to 96 h, of the d-value (contour interval 300 km) of a frontal system introduced to a new model domain

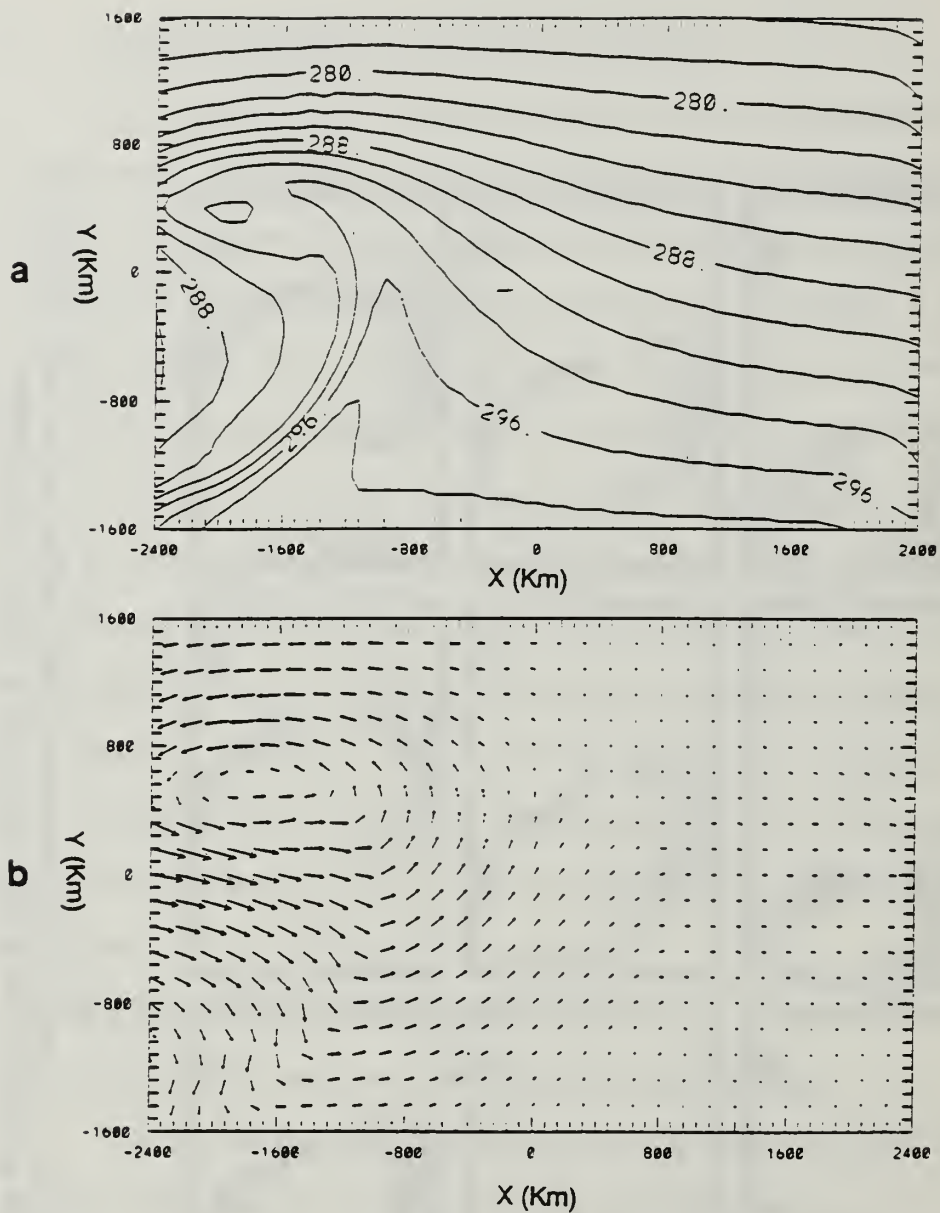


Fig. 5.2 Frontal system in the new domain with no mountain at $t = 54$ h: (a) sea-level potential temperature ($^{\circ}\text{K}$), and (b) sea surface wind with a maximum vector of 32 m/s.

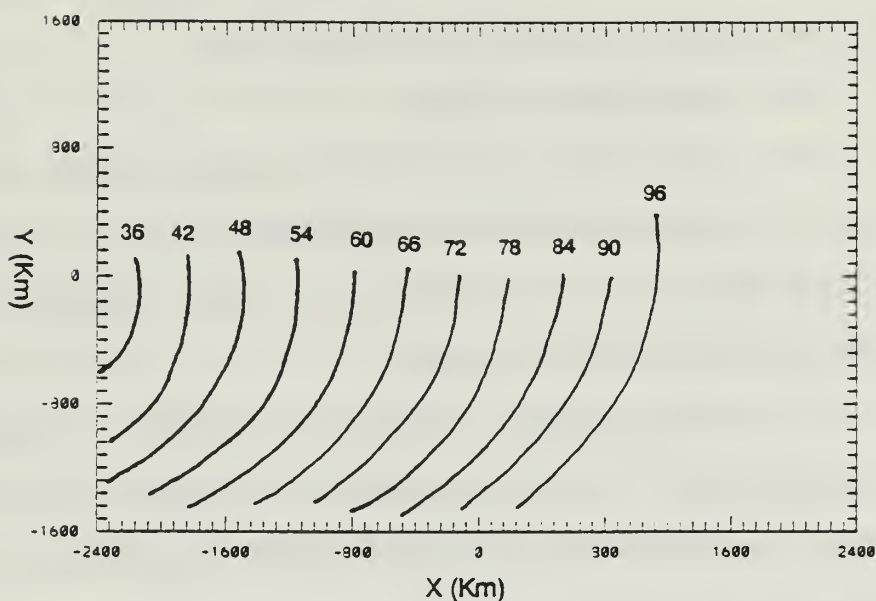


Fig. 5.3 Position of the cold front without a mountain determined by tracing the minimum d-value. Time interval is 6 h, the leftmost position is at 36 h and the rightmost one is at 96 h.

TABLE 1 SUMMARY OF MOUNTAIN SCALES FOR ALL CASES.

Case	$a_{x0}(\text{km})$	$a_{y0}(\text{km})$	rotation	comment
0	--	--	---	No mountain
1	720	720	--	Large-scale circular mountain
2	240	240	--	Mesoscale circular mountain
3	720	240	$\pi/2$	East-west oriented
4	240	720	0	North-south oriented,
5	240	720	$\pi/4$	Parallel to the front

The variables a_{x0} and a_{y0} are the mountain scale in x and y directions, respectively. Rotation is the angle between the north and the major axis of an elliptical-shaped mountain.

and a_{0y} in Eq. (3.1), where $0.766a_{0x}$ is approximately the half-width. The grid size of the numerical model is 80 km, the model domain is 4800 km in the x and 3200 km in the y directions and the integration time step is 200 s.

2. Description of Cases

Five experiments that are summarized in Table 1 are carried out to probe the influence of different mountain characteristics on a cold front. These cases are designed to understand how a cold front is influenced by mountains with different sizes, shapes and orientations.

The first case is designed to investigate the large-scale circular mountain influences. The mountain scale is 720 km in both x and y directions, i.e., a circular mountain. The Rossby number computed from the basic flow is within the semi-geostrophic approximations. Thus, this case will show whether the mountain flow would change when a more realistic front passes, and it will be compared with results from previous semi-geostrophic studies (Bannon 1984b; Davis 1984). The results of this experiment will be also compared to the three-dimensional semi-geostrophic model by Blumen and Gross (1987b).

The second case will examine the influence of a mesoscale circular mountain (240 km) on the moving cold front. The flow response will be more ageostrophic as was found on the lee side of a mesoscale mountain. The front is expected to be more profoundly affected by the ageostrophic mountain circulation. Since the horizontal mountain size is much smaller than the first case, the period of time that the mountain will have an influence on the front is much shorter. The purpose of this case is to see the effects of different sizes of the mountains.

An elliptical-shaped mountain with the major axis parallel to the basic flow is designed for the third case, which has mountain scales $a_{0x}=720$ km and

$a_{0y}=240$ km. This is an east-west oriented mountain ridge that is large scale in the x-direction and mesoscale in the y-direction. The size and shape of this mountain is comparable to the Alps where many observations have been obtained. If a front moves from west to east, it will take a longer time to pass this mountain ridge as opposed to the previous case of a mesoscale circular mountain. Given the longer interaction period, the front will experience more influences from the mountain.

The fourth case has a mountain shape with $a_{0x}=240$ km and $a_{0y}=720$ km. This elliptical-shaped mountain is oriented in the north-south direction so that the major axis of the mountain is normal to the basic flow. Although this mountain is more like a two-dimensional obstacle to the basic advection current, the cold front, due to its northeast-southwest orientation, is not parallel to the mountain ridge.

In the last case, the elliptical-shaped mountain is rotated 45 degrees, which makes the major axis of the mountain nearly parallel to the approaching front. This configuration resembles most closely the previous two-dimensional frontal-mountain studies and the results will be compared with them.

For each of the five cases, the results are first described, and then the dynamics associated with the frontal variations are investigated by studying the frontogenesis forcing function. The discussion is followed by a short summary for each case.

C. DISCUSSIONS OF RESULTS

1. Case 1: Large-scale Circular Mountain

a. Analysis of The Results

A large-scale mountain with characteristic lengths $a_{0x} = a_{0y} = 720$ km is used in this experiment. The mean advective flow is $U = 5$ m/s at the

lowest level and the vertical wind shear equals to $2.5 \times 10^{-3} \text{s}^{-1}$. If the basic flow at the lowest level is used as the characteristic value, then $Fr = 0.25$ and $Ro = 0.069$, which is within the range of semi-geostrophic and quasi-geostrophic approximations.

The time evolution of the frontal position and intensity (d-value) is shown in Fig. 5.4. The frontal intensity decreases when the cold front is moving up the mountain ($t = 48 \text{ h}$ and $t = 54 \text{ h}$). The northern part of the front weakens significantly at $t = 54 \text{ h}$. The cold front intensifies and extends northward as it moves downslope ($t = 60 \text{ h}$ and $t = 66 \text{ h}$). A slight distortion on the horizontal frontal structure is also found in this period. The maximum intensity is reached as the front begins to leave the mountain area at $t = 78 \text{ h}$. The front experiences another weakening when it moves about 1000 km downstream of the mountain and then recovers its intensity and horizontal structure when it moves away from the mountain influences.

The horizontal temperature and wind fields (Fig. 5.5) show in detail the changes of the frontal structure due to the mountain influences. Before the cold front arrives on the mountain, the flow impinging on the obstacle is dominated by the southwesterly pre-frontal wind and an anticyclonic curvature in the flow is observed over the mountain (Fig. 5.5a). A local maximum in the wind speed is found at the mountain top. Consistent with the flow field, the vorticity field (Fig. 5.5b) has an anticyclonic vorticity over the northwestern slope and anticyclonic vorticity over the top and southeastern slope. A vorticity maximum on the left boundary indicates that the cyclone and the associated fronts are transported into the domain through the boundary. The vertical velocity pattern (not shown) is almost anti-symmetric with respect to the center of the mountain. The upward motion on the southwest slope and the downward motion on the northeast slope of



Fig. 5.4 Time evolution each 6 h from $t = 48$ h to $t = 96$ h of the d-value (km) of a front passage over the large-scale circular mountain in Case 1

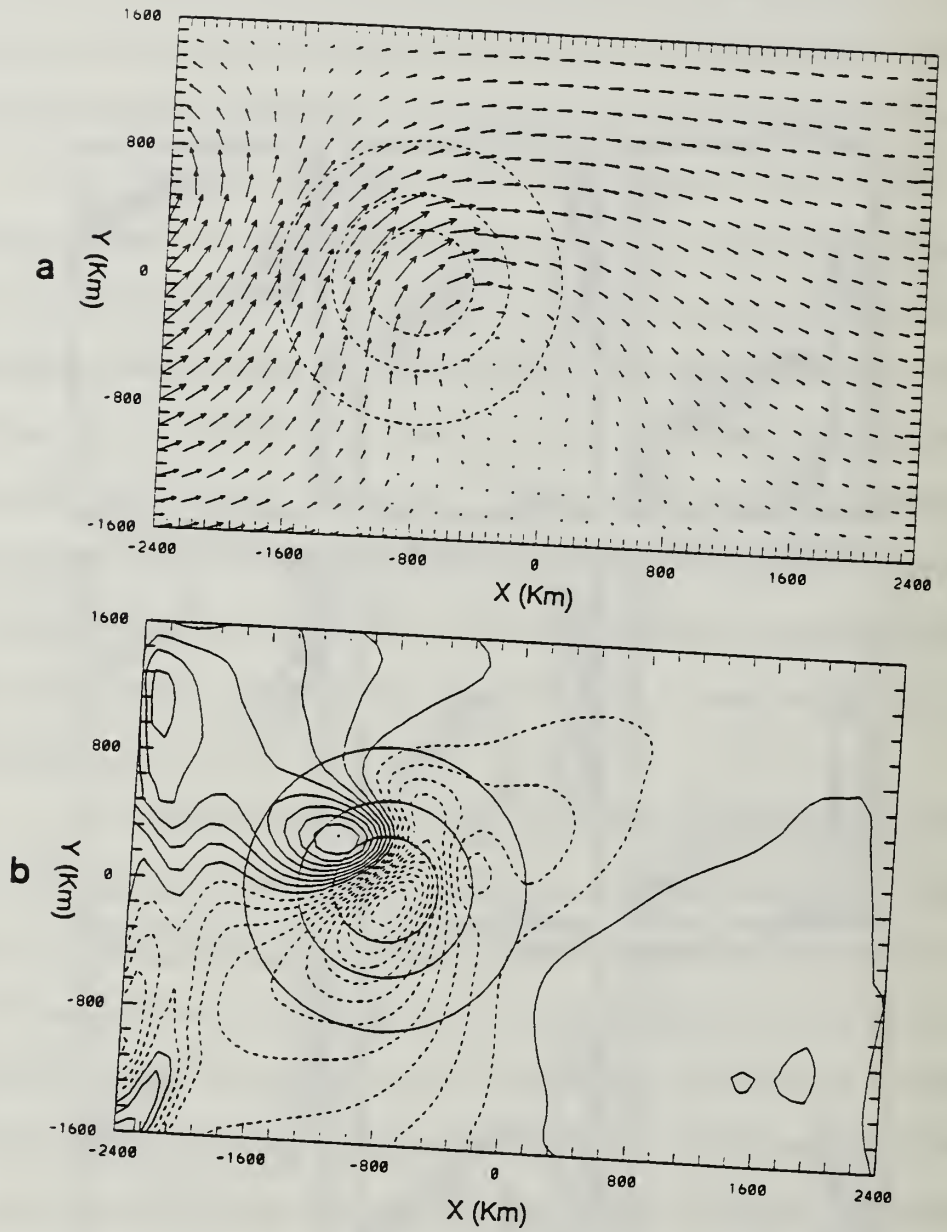


Fig. 5.5 Frontal system approaching large-scale circular mountain at $t = 24$ h in Case 1 on the level of $\sigma = 0.99$: (a) wind field, with contour interval 5 m/s; (b) vorticity, with contour interval of $0.55 \times 10^{-5} \text{ s}^{-1}$, maximum value $= 0.45 \times 10^{-4} \text{ s}^{-1}$ and minimum value $= -0.7 \times 10^{-4} \text{ s}^{-1}$

the mountain implies that the orientation is consistent with the direction of the southwesterly pre-frontal wind. This mountain circulation is similar to the semi-geostrophic mountain solution by Blumen and Gross (1987b) except the prevailing wind in this study is associated with the pre-frontal southwesterlies rather than the mean basic flow in their study.

The cold front weakens as it arrives and moves up the mountain (Fig. 5.6) at $t = 48$ h. Both the horizontal temperature gradient (Fig. 5.6a) and the wind shear (Fig. 5.6b) over the mountain area are not as large as in the remainder of the cold front, which still possesses a significant temperature gradient. The northern part of the post-frontal flow penetrates the weakened frontal zone, converges with the over-mountain pre-frontal flow to form a maximum wind speed north of the mountain top.

After the northern part of the front has moved to the eastern slope at $t = 60$ h, the horizontal temperature gradient increases and extends to the north (Fig. 5.7a). The post-frontal flow, which has a significant component in the east-west direction, experiences a splitting upstream of the mountain (Fig. 5.7b). Most of the flow moves over the mountain to the east and only a small portion of the northwesterly flow moves to the south.

As the northern part of the cold front moves down the leeside slope at $t = 72$ h, its intensity is further increased (Fig. 5.8a). Since the prevailing wind over the mountain is mainly the westerly flow behind the front, the wind speed maximum is shifted downstream to the eastern slope (Fig. 5.8b). The strong wind on the leeside pushes this part of the front eastward so that the surface front is deformed slightly. The front continues intensifying within the convergence zone on

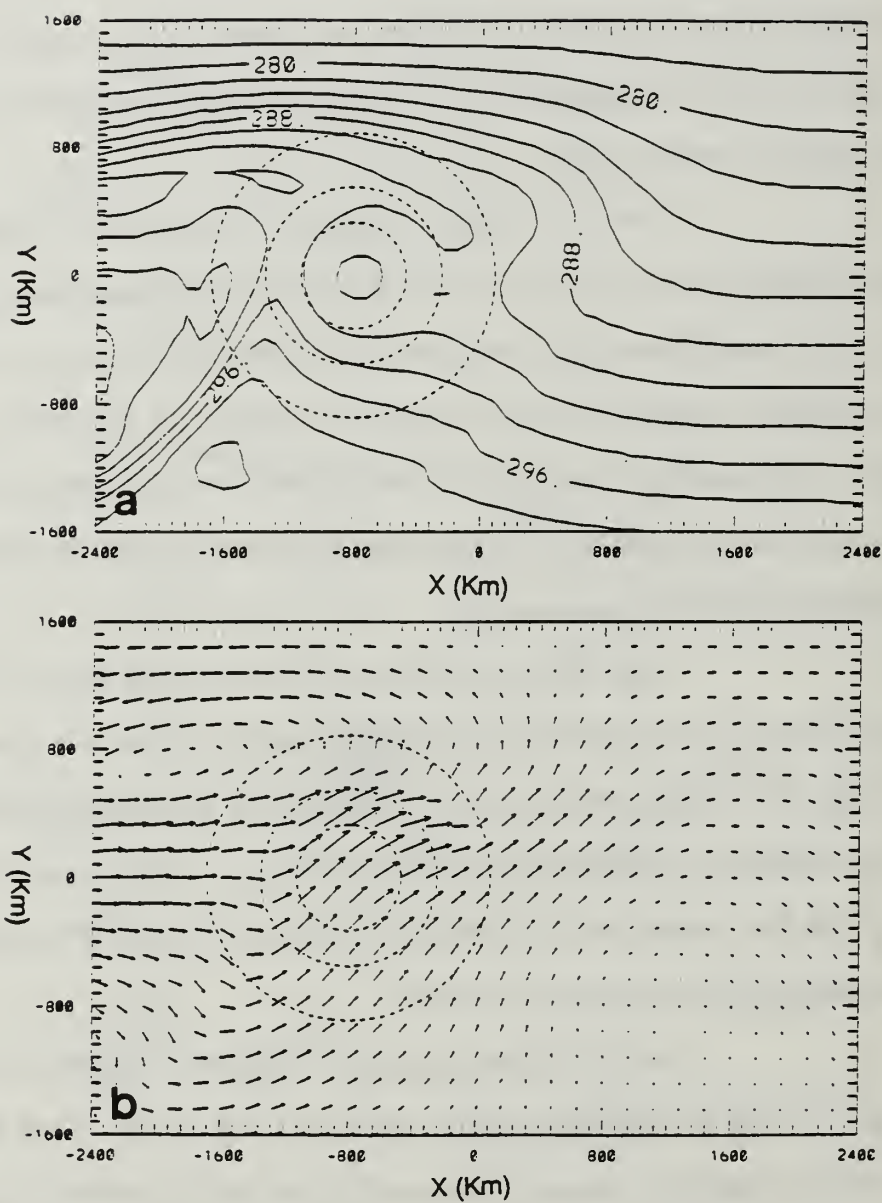


Fig. 5.6 Frontal system over large-scale circular mountain at $t = 48$ h: (a) sea-level potential temperature ($^{\circ}\text{K}$); and (b) terrain surface wind with the maximum wind speed 36 m/s

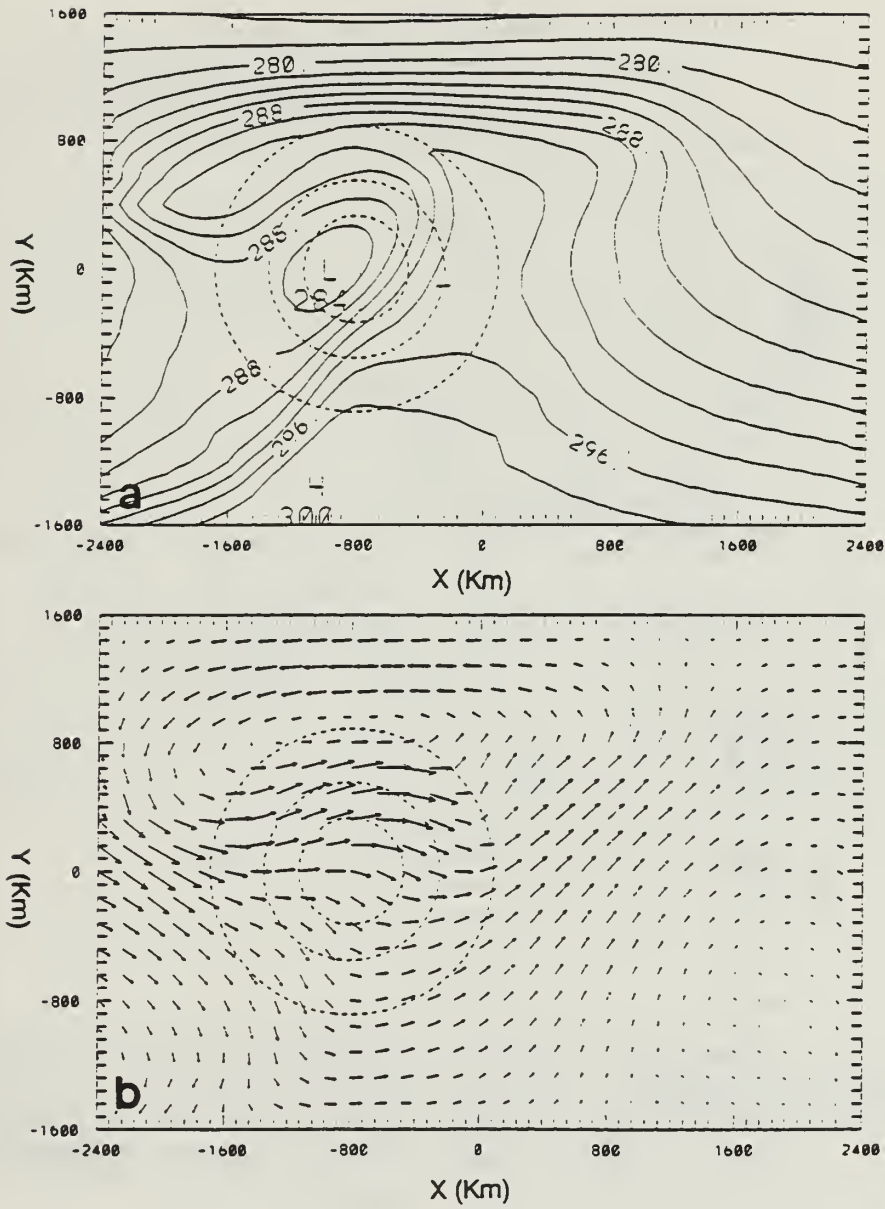


Fig. 5.7 As in Fig. 5.6 except for $t = 60$ h, and maximum surface wind of 38 m/s.

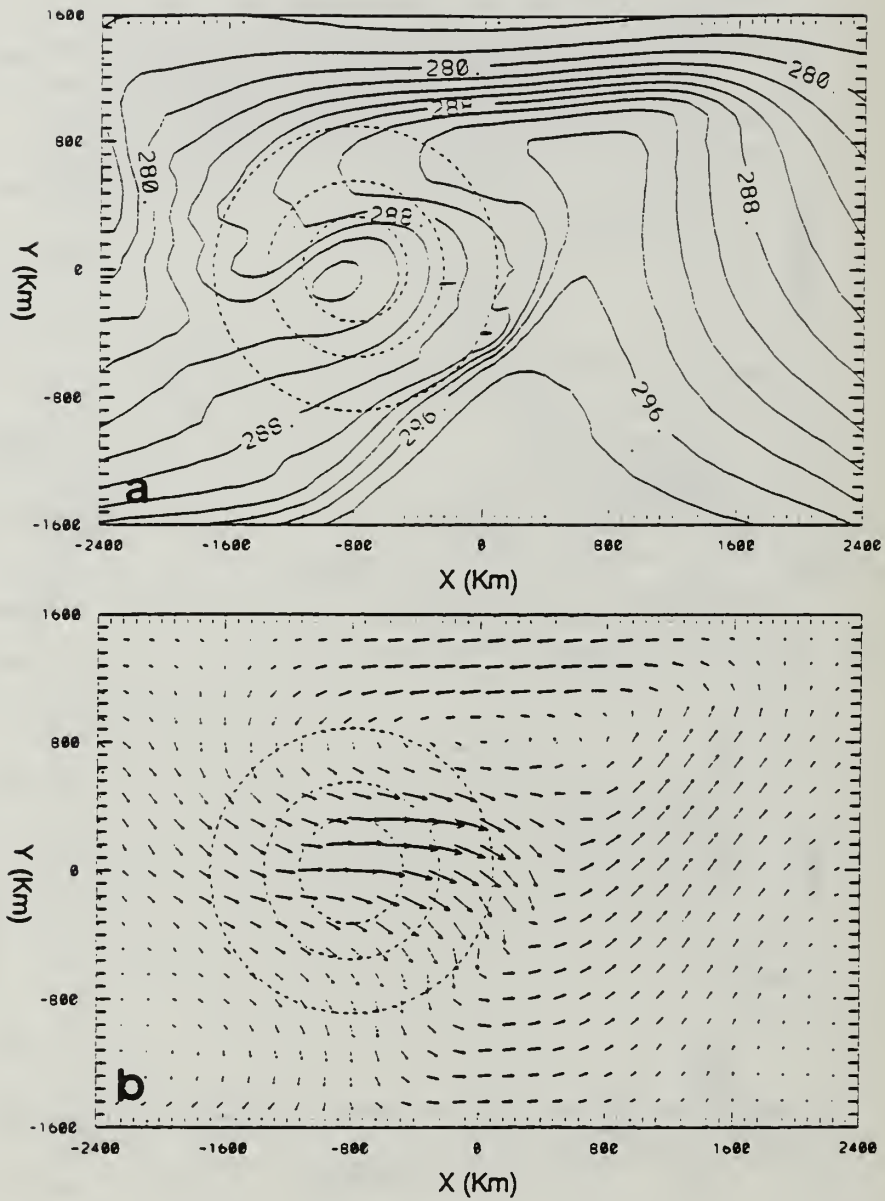


Fig. 5.8 As in Fig. 5.6 except for $t = 72$ h, and maximum surface wind of 48 m/s.

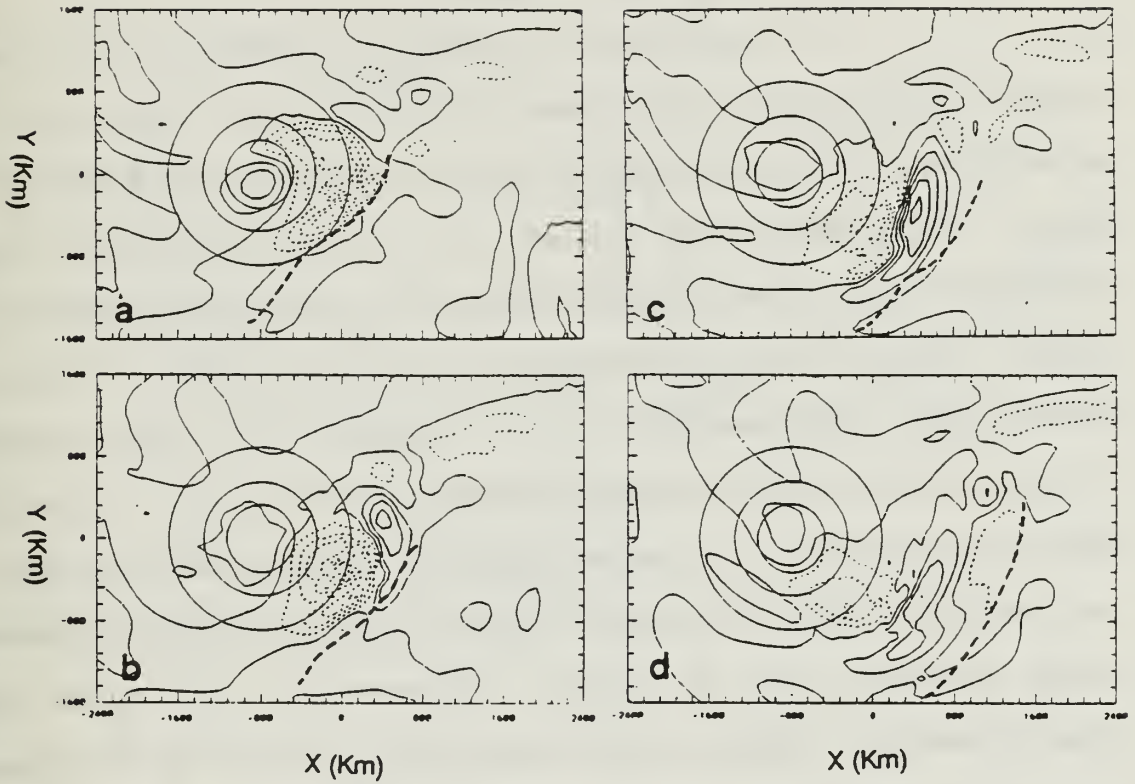


Fig. 5.9 Divergence (contour interval = $0.2 \times 10^{-4} \text{s}^{-1}$) field for (a) $t = 72 \text{ h}$, (b) $t = 78 \text{ h}$, (c) $t = 84 \text{ h}$ and (d) $t = 90 \text{ h}$. Dashed line indicates convergent zone and solid line indicates divergent zone. The heavy dashed line is the cold front position.53

the leeside. These convergent and divergent zones and the cold front positions after the front moves to the east of the mountain are shown in Fig. 5.9.

b. Frontogenetic Forcing

To understand the dynamics associated with the frontal change, the frontogenetic forcing terms during the frontal passage over the mountain are computed at the model's lowest level where the frontal intensity is the largest. Among all the terms contributing to the total frontogenetic forcing discussed in Chapter IV, the horizontal deformation term always dominates near the surface. This term can be further separated into the stretching term and the shearing term. The stretching term is associated with vertical stretching accompanied by the mean horizontal convergence or divergence. The shearing effect changes the frontal temperature gradient by the horizontal wind shear in each direction. When an air column moves over the mountain, the frontogenetic forcing contributed from the mountain circulation is via the vortex tube stretching/shrinking. Therefore, the stretching term dominates the frontogenetic forcing. When the air goes around the mountain, the flow changes its direction and the shearing term will have a contribution to the frontogenesis.

At $t = 48$ h, the northern part of the front reaches the mountain (Fig. 5.6). The horizontal deformation term, which dominates the frontogenetic forcing, is shown in Fig. 5.10a. The major impinging flow at this time is still the pre-frontal wind, which causes a frontogenesis on the northeastern quadrant of the mountain. However, this frontogenetic forcing induced by the mountain is small and the maximum frontogenetic forcing is associated with the front. After the front passes the mountain crest at 60 h (Fig. 5.10b), the post-frontal flow impinges on the mountain and induces a frontogenetic forcing on the eastern

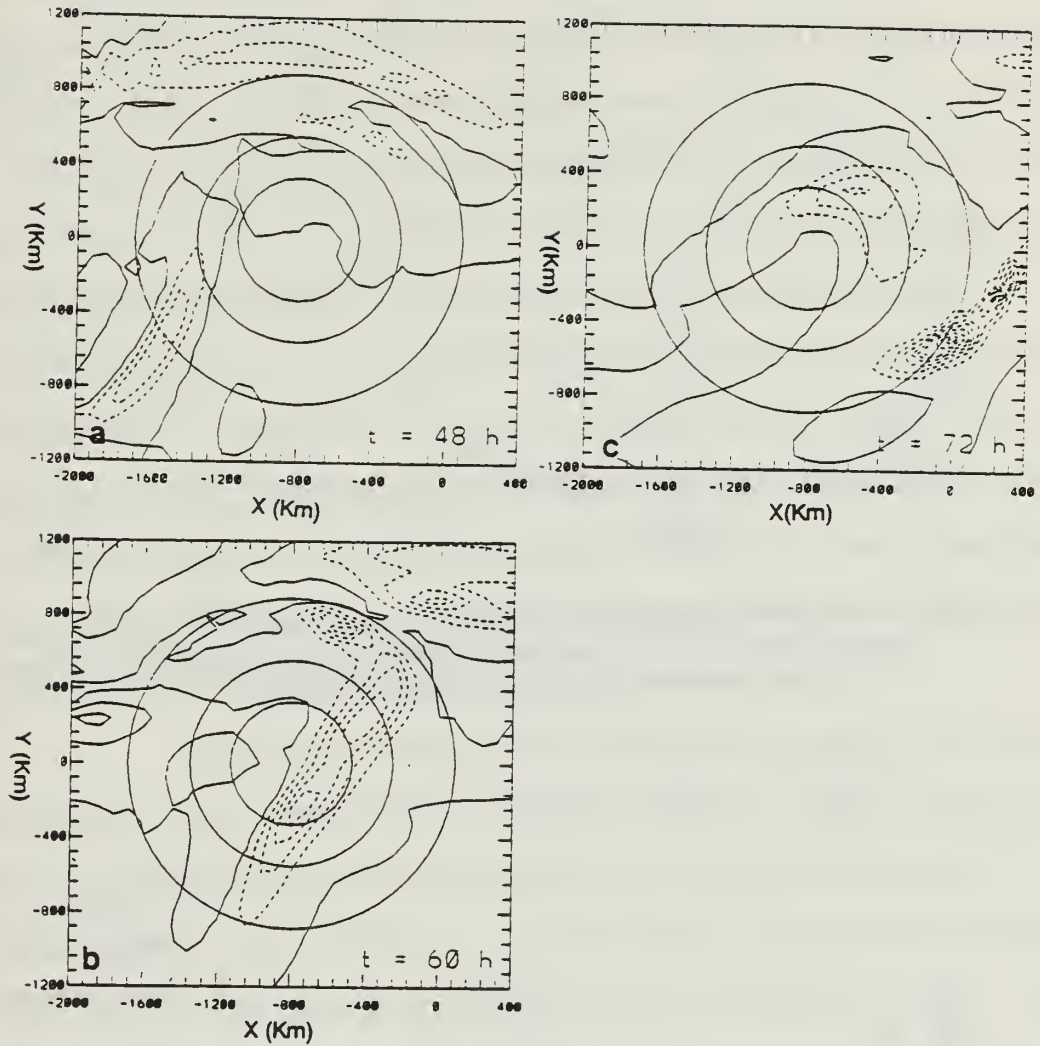


Fig. 5.10 Horizontal deformation forcing ($\circ \text{K}^2 \text{m}^{-2} \text{s}^{-1}$) on level $\sigma = 0.99$. in the region of frontogenesis (dashed lines) and in the region of frontolysis (solid line) at : (a) $t = 48 \text{ h}$ with minimum values of -0.16×10^{-13} associated with the cold front and -0.25×10^{-14} in the mountain area; (b) $t = 60 \text{ h}$, maximum forcing on northeastern slope with a minimum value of -0.59×10^{-14} ; and (c) $t = 72 \text{ h}$, with maximum forcing (-0.2×10^{-12}) located at the cold front region.

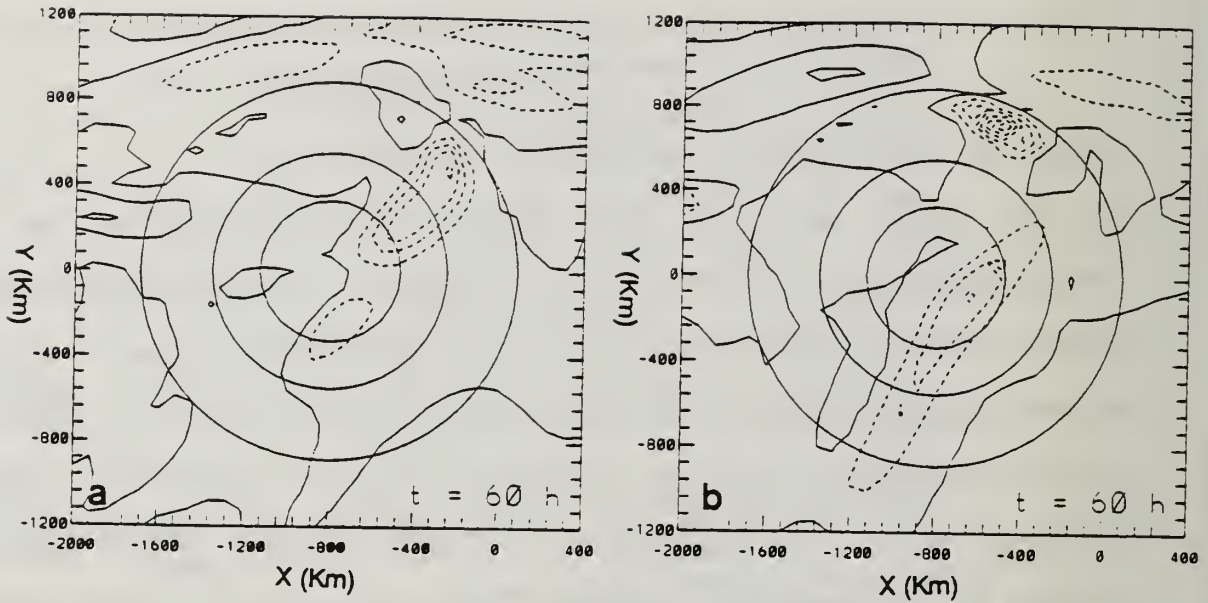


Fig. 5.11 (a) Stretching and (b) shearing deformation ($\circ K^2 m^{-2} s^{-1}$) at $t = 60$ h. The sum of these terms is the total deformation forcing function shown in Fig. 5.10 b. Contour interval 0.5×10^{-14} in both (a) and (b)

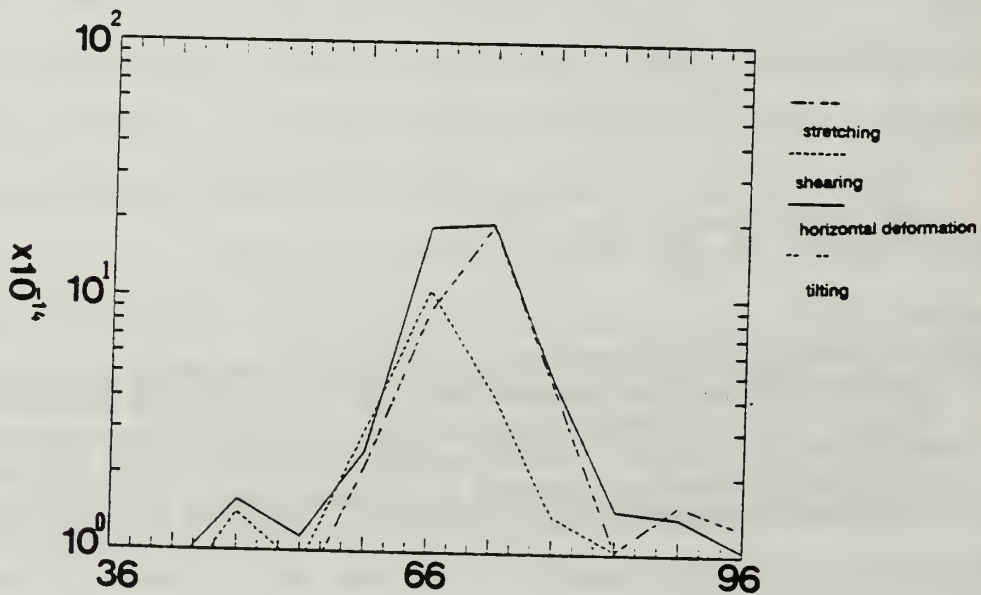


Fig. 5.12 Time (h) evolution of the maximum stretching, shearing, total horizontal deformation and tilting forcing at $\sigma = 0.99$ during the cold front passage over a large scale circular mountain (Case 1). Ordinate has a logarithm scale (unit: $\circ K^2 m^{-2} s^{-1}$)

slope. At this time, this mountain-induced leeside frontogenetic forcing is comparable to the frontogenetic forcing associated with the original front. This horizontal deformation forcing at 60 h is contributed equally from the stretching and shearing terms (Fig. 5.11), i.e. the contributions are equally from the flow going over and around mountain. The combination of these two forcings extends the original front to the north as a superposition effect. By $t = 66$ h (Fig. 5.10c), the maximum frontogenetic forcing moves to the southeastern side of the mountain, and the horizontal deformation forcing is still contributed equally from stretching and shearing deformation forcings. Fig. 5.12 shows the time evolution of these different forcing items. Beyond 66 h, the major contribution to the deformation forcing comes from the stretching deformation term, which indicates the major flow goes over the mountain. This is because the larger wind speed associated with the post-frontal wind has higher momentum to go over the mountain.

Blumen and Gross (1987b) computed the frontogenesis forcing function based on the semi-geostrophic mountain solution. Their computation indicates that the tilting term contributes as much or more than the divergence term (the stretching term). This is different from the present result as different wind fields were used and the shearing deformation was not computed by them. The calculation under the semi-geostrophic mountain flow limits the motion in the large scale and reduces the stretching and shearing effects.

c. Summary

This first case shows the effect of a large-scale mountain on an approaching front. This experiment is carried out to compare the results with previous semi-geostrophic studies. As the front approaches the mountain, the impinging flow to the mountain changes from the basic westerly current to the wind

associated with the front. This is the major difference from previous studies even though the mountain scale and the mean flow speed is within the semi-geostrophic approximation. The frontogenetic forcing from the mountain receives a large contribution from this incident flow associated with the front. When the cold front is on the upwind slope, the major flow that impinges on the mountain is dominated by the pre-frontal southwesterly wind. A weak frontolysis occurs on the southwestern slope and a frontogenesis on the northeastern slope. However, this pre-frontal frontogenetic forcing induced by the mountain has little effect on the front, because the mountain is large and the cold front has not reached this frontogenesis area. When the cold front has moved over the mountain, the impinging flow is dominated by the post-frontal northwesterly wind and produces strong downslope wind on the lee side of the mountain. Therefore, the maximum frontogenetic forcing of the mountain now occurs on the eastern side of the mountain. This forcing generates the local front-like temperature gradient and extends the cold front more northward as a superposition effect. The strong downslope wind pushes the front forward rapidly and deforms the horizontal frontal structure slightly.

2. Case 2: Meso-scale Circular Mountain

a. Analysis of The Results

The shape of the mountain in this case is the same as in Case 1 except that the horizontal size ($a_{0x} = a_{0y} = 240$ km) is reduced to study the influence of a mesoscale mountain on the front. The mean advection speed, vertical shear, Coriolis parameter and Brunt-Vaisala frequency are all the same as in the first experiment. The Rossby number of this mean flow, based on the surface wind, is 0.21 and the Froude number is 0.25.

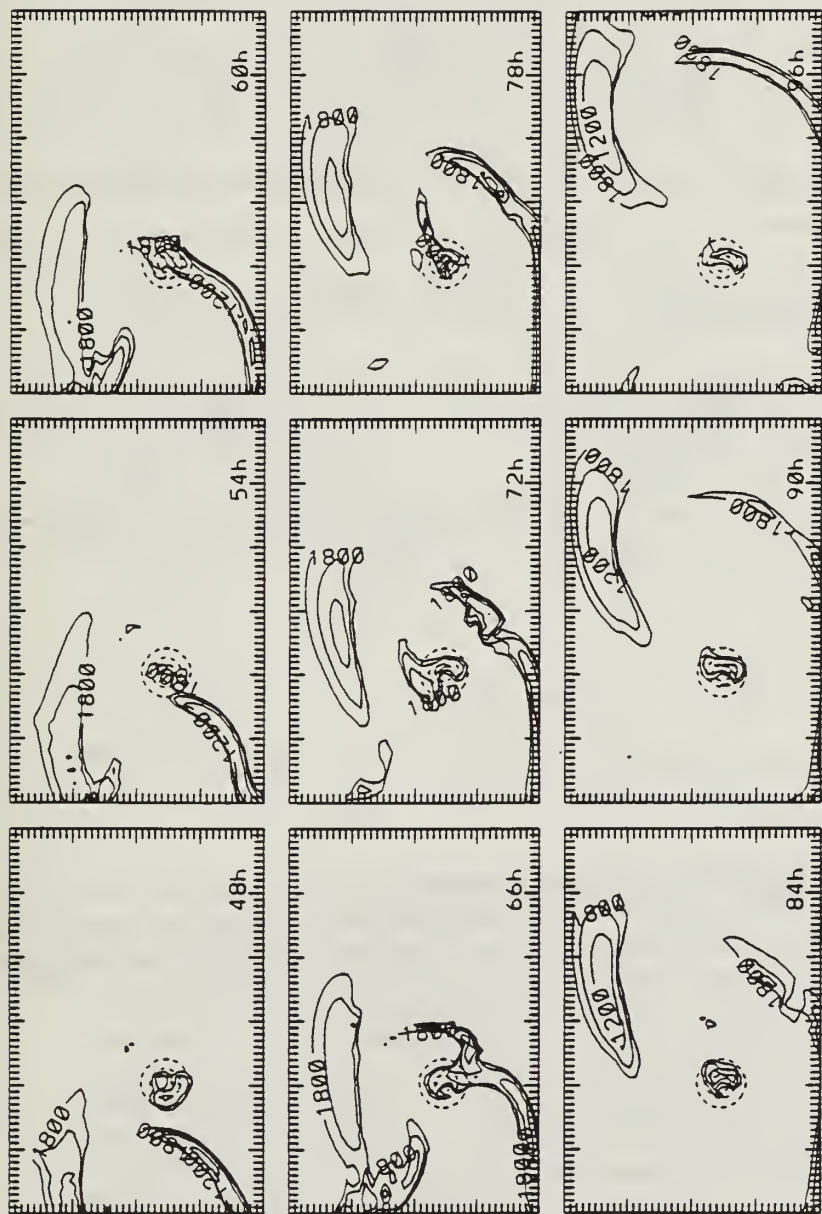


Fig. 5.13 Time evolution each 6 h, from 48 h to 96 h, of the d-value (contour interval 300 km) of a frontal passage over a large-scale circular mountain in Case 1

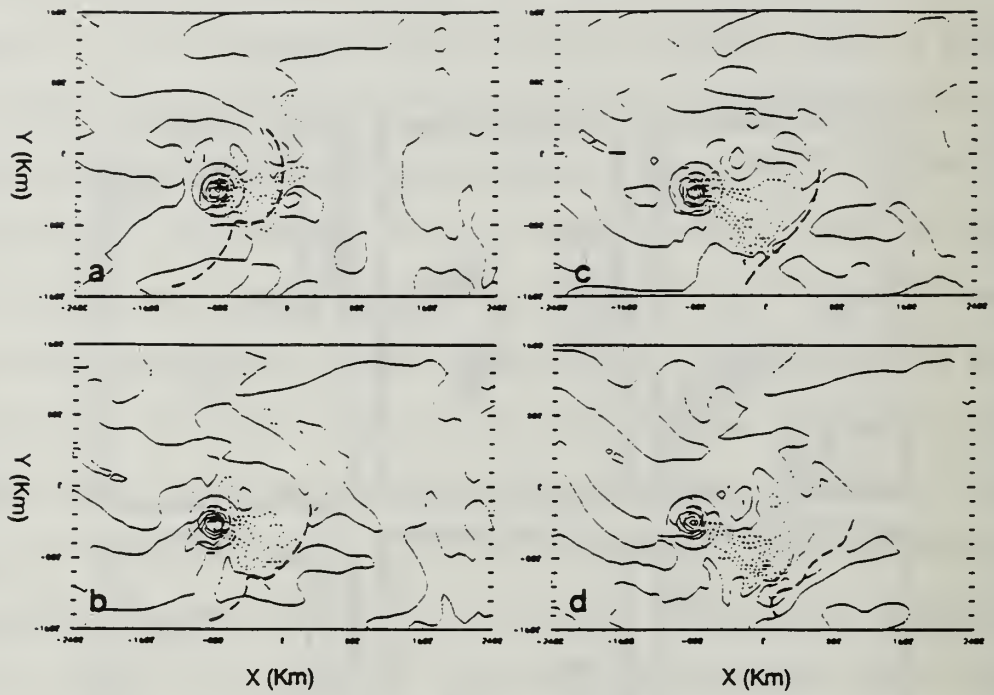


Fig. 5.14 Divergence field (contour interval $0.2 \times 10^{-4} \text{ s}^{-1}$) for (a) $t = 66 \text{ h}$, (b) $t = 72 \text{ h}$, (c) $t = 78 \text{ h}$ and (d) $t = 84 \text{ h}$. Dashed line indicates convergent zone and solid lines indicate divergent zone. The heavy dashed line is the cold front position.

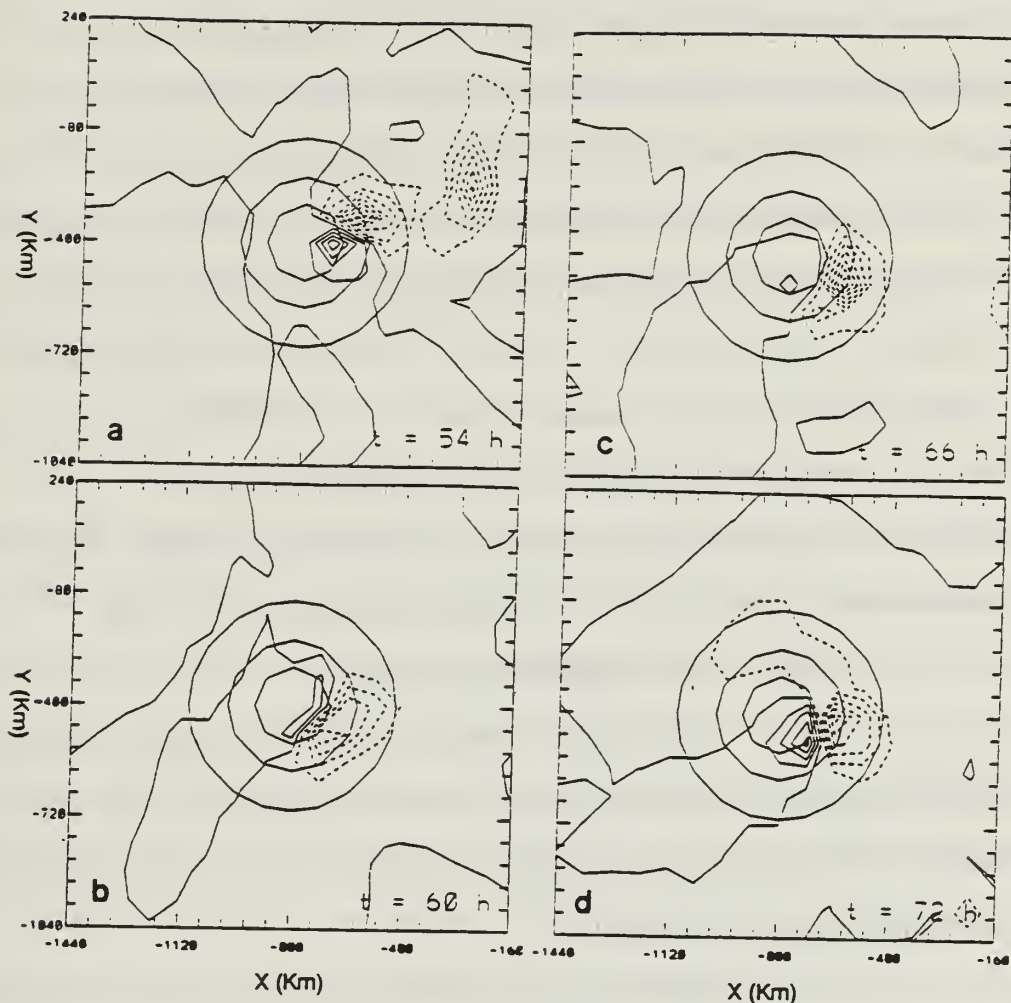


Fig. 5.15 Frontogenesis (dashed lines) and frontolysis (solid lines) regions from horizontal deformation forcing ($^{\circ}\text{K}^2\text{m}^{-2}\text{s}^{-1}$) on level $\sigma = 0.99$ for the mesoscale circular mountain: (a) $t = 54$ h, with minimum value of -0.98×10^{-13} and maximum value of 0.63×10^{-13} , contour interval = 0.14×10^{-13} , (b) $t = 60$ h, with a maximum of 0.73×10^{-13} and a minimum of -0.23×10^{-12} , the contour interval 0.4×10^{-13} , (c) $t = 66$ h, with maximum value of 0.14×10^{-12} , minimum value of -0.75×10^{-12} and the contour interval is 0.8×10^{-13} , and (d) $t = 72$ h, with maximum value of 0.46×10^{-12} , minimum value of -0.63×10^{-12} and the contour interval = 0.8×10^{-13} .

The time evolution of the d -value, showing the frontal intensity and position is given in Fig. 5.13. The mountain effects on the front in this case are similar to the previous case as their shapes are the same, even though the scale of this mountain is only one third of the large-scale mountain. The cold front is again weakened and intensified on the upslope and downslope, respectively. The frontogenesis region on the southeastern slope deforms the front more substantially than that in the first case (Case 1, $t = 66$ h), but this is again due to the superposition effect. The intensification is further enhanced as the front moves out from the mountain and passes over the convergence area ($t = 72$ h). A second phase of weakening on the frontal intensity is also found when the front is influenced by the divergent zones farther downstream (Fig. 5.14c).

b. Frontogenetic Forcing

The smaller mountain scale is the major difference between this case and the previous large-scale mountain experiment. The smaller mountain scale with the same mountain height has a steeper slope, which implies a stronger downslope wind on the leeside.

The frontogenetic forcing function before and after the front passes over the mountain is shown in Fig. 5.15. The diagram contains only the central part of the total model domain for better viewing. Compared to the case of the large-scale mountain, the maximum magnitude of the frontogenetic forcing here is five to ten times larger. This is due to the fact that the small-scale mountain has a steeper slope and produces stronger wind field changes and associated divergence effects. Both frontogenesis and frontolysis regions occur on the leeside slope with the former located downstream from the latter. This is different from the large-scale mountain case in which the frontolysis is on the upwind side and the

frontogenesis is on the leeside, i.e., anti-symmetric with respect to the mountain crest. Since the mountain scale is small, the mountain-induced maximum wind is shifted downstream to the lee slope rather than on the mountain crest as in a large-scale mountain. This is also observed in the flow over a two-dimensional mountain in Williams *et al.* (1992). The mountain-induced frontogenesis is contributed equally in order of magnitude from the stretching and the shearing terms when the front is in the mountain vicinity (Fig. 5.16).

c. Summary

As in the previous large-scale mountain case, the prevailing wind near this mesoscale mountain is dominated by the frontal-associated wind instead of the mean wind. Compared to the large-scale circular mountain case, the interaction with the barrier generates a stronger convergence/divergence field on the lee side due to the steeper mountain slope and produces stronger frontogenetic forcing on the leeside of the mountain. Since the time that a front experiences the frontogenetic forcing by the mesoscale mountain is shorter than in the large mountain case, the net effects are similar. The frontolysis region is also located on the leeside, just upstream of the frontogenesis region. This is because the mountain-induced maximum wind is shifted downstream on the lee-side slope as opposed to its location on the crest in the large-scale mountain case. Larger frontal distortion appears in this case as the mountain size is smaller compared to the total front. After the front has moved away from the mountain, its structure is restored. The final displacement is about the same as for the large mountain case and is ahead of the front without the mountain.

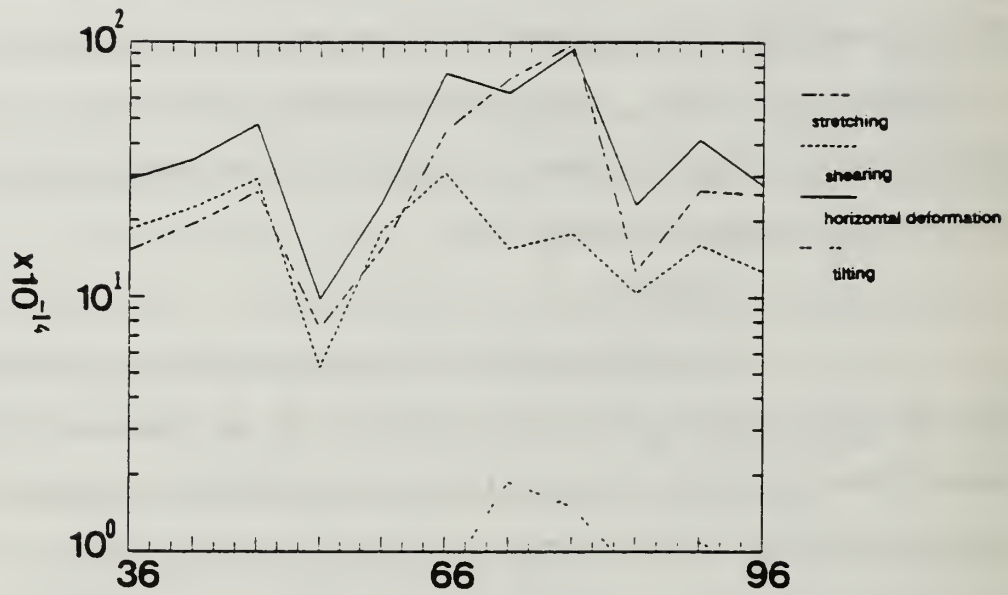


Fig. 5.16 Time (h) evolution of the maximum stretching, shearing, total horizontal deformation and tilting forcing at $\sigma = 0.99$ during the cold front passage over a mesoscale circular mountain (Case 2). Ordinate has a logarithmic scale (unit: $^{\circ}\text{K}^2\text{m}^{-2}\text{s}^{-1}$)

3. Case 3: East-west Oriented Mountain Ridge

a. Analysis of The Results

The east-west oriented mountain has a large characteristic length $a_{0x}=720$ km in the x-direction and a mesoscale length $a_{0y}=240$ km in the y-direction. This mountain profile is similar in size and shape to the Alps.

Due to the east-west oriented mountain shape, the cold front takes a longer time to pass over the mountain (Fig. 5.17). Consequently, the influences on the front are more pronounced, and a significant distortion of the horizontal frontal structure occurs during its passage over the mountain.

Before the front arrives, the prevailing wind on the mountain is dominated by the pre-frontal southerly flow. At $t = 36$ h (Fig. 5.18), the maximum in the anticyclonic flow crossing the mountain is on the northern slope of the mountain, which is the leeside. A low temperature center is found on the mountain top. Due to the significant over-mountain flow, the adiabatic cooling is more pronounced than it is in the circular mountain case. However, the maximum in temperature is found on the lee-side where the downslope winds are strong. These characteristics are similar to the foehn generated by the downslope wind on the northern slope of the Alps as sketched by Smith (1987) in Fig. 1.2. The temperature disturbances shown on the upwind and downwind slopes of the mountain at $t = 48$ h and $t = 54$ h in Fig. 5.17 are due to the quasi-steady mountain solution for a stratified fluid induced by the weaker pre-frontal flow. These temperature disturbances create the superposition effect on the front when it arrives.

When the cold front arrives at the mountain at $t = 60$ h (Fig. 5.19), the post-frontal northwesterly flow is split into a strong eastward along-

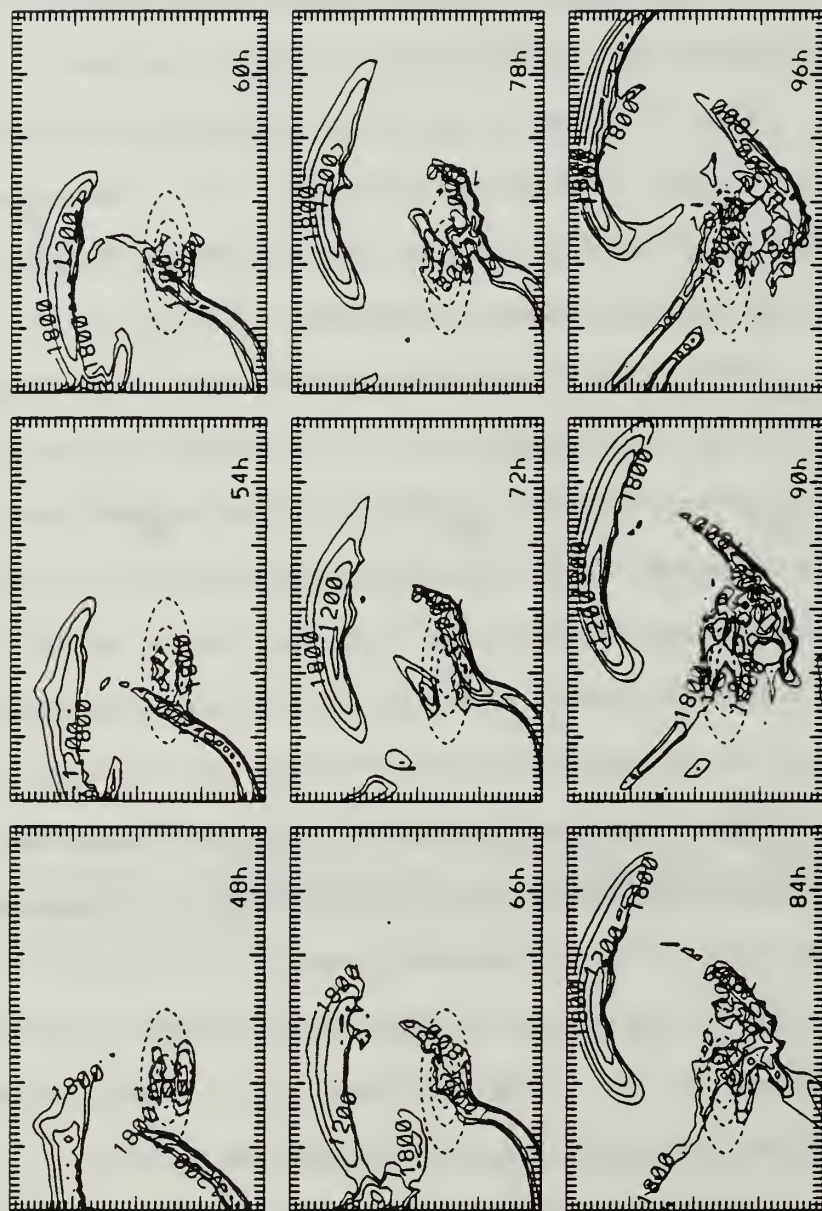


Fig. 5.17 Time evolution each 6 h from $t = 48$ h to $t = 96$ h of the d-value (km) of a front passage over the east-west oriented mountain in Case 2

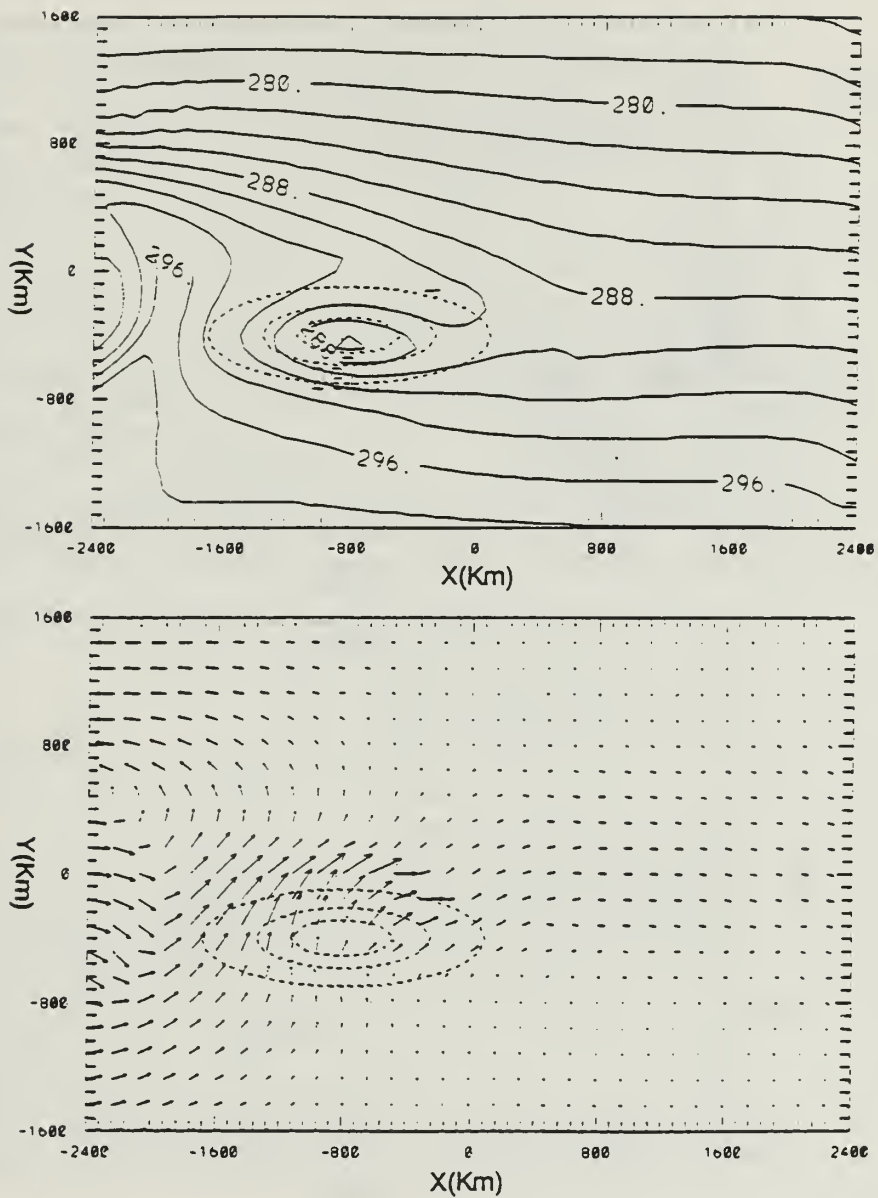


Fig. 5.18 Frontal system over the east-west oriented mountain at $t = 36h$: (a) sea-level potential temperature ($^{\circ}K$); and (b) terrain surface wind with the maximum wind speed of 35 m/s

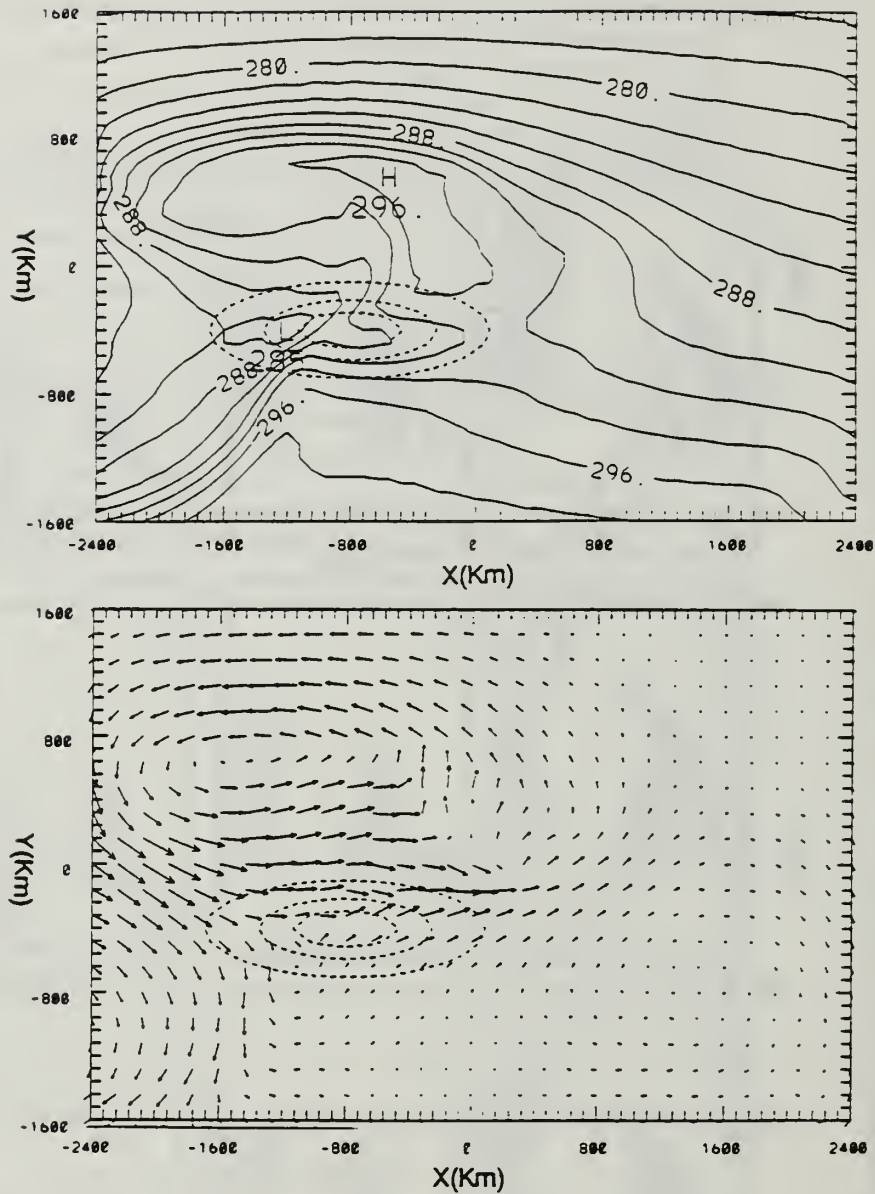


Fig. 5.19 Frontal system over the east-west oriented mountain at $t = 60h$: (a) sea-level potential temperature ($^{\circ}K$); and (b) terrain surface wind with the maximum wind speed 38 m/s

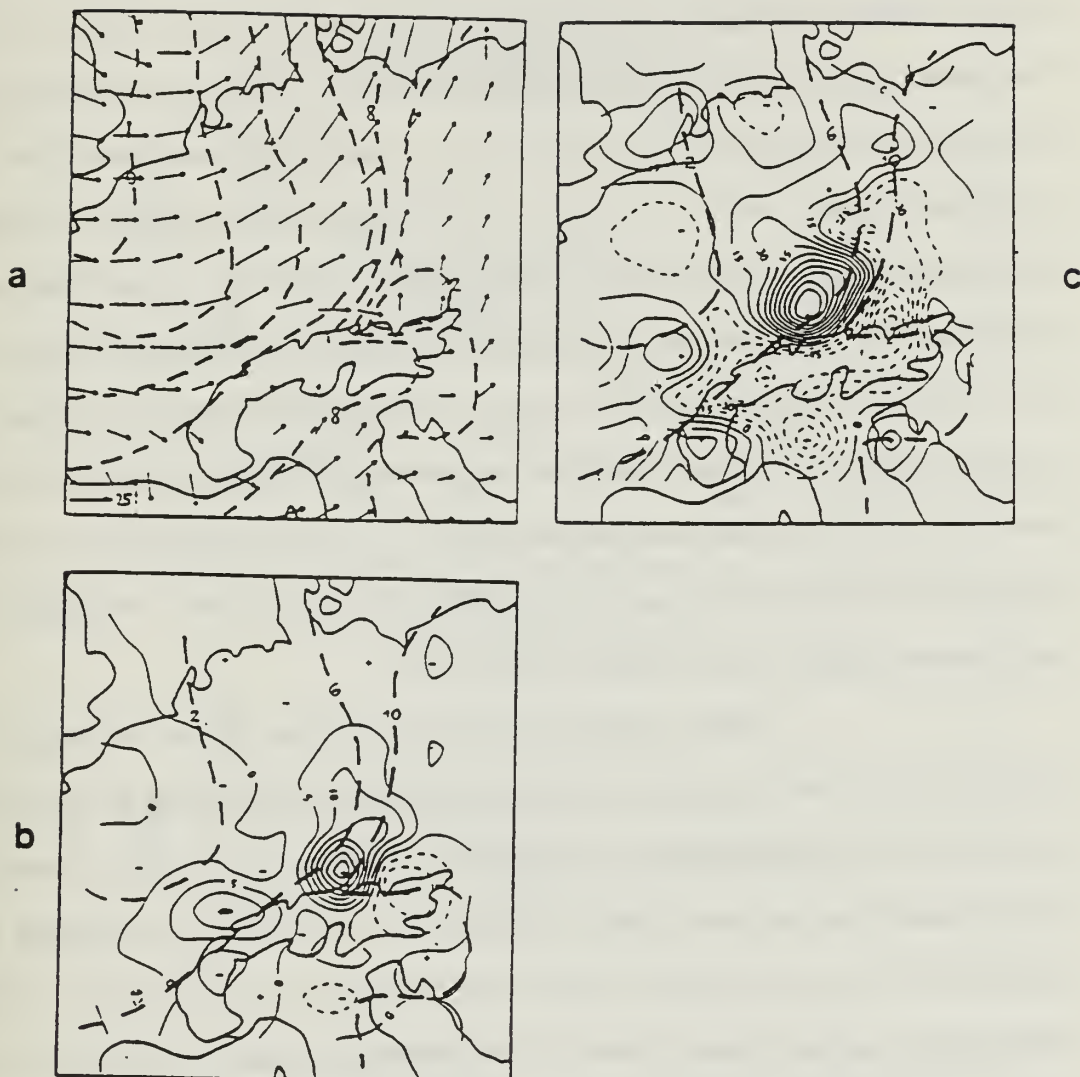


Fig. 5.20 Analysis at 850 hpa on 12 UTC October 8. from Fig. 4 of Kurz(1990) (a): Winds (ms^{-1}) and isotherms (dashed, $^{\circ}\text{C}$); (b) frontogenesis function FH (in $10^{-10} \text{Km}^{-1} \text{s}^{-1}$); and (c) omega-forcing (in $10^{-17} \text{m}^{-1} \text{s}^{-3}$).

mountain flow and a southward flow (Fig. 5.19b). This flow splitting behind the front is commonly observed in the Alps as sketched by Smith (1987) in Fig. 1.2 c. The combination of the over-mountain pre-frontal flow and the along-mountain post-frontal flow causes the occurrence of a maximum convergent zone on the northwestern slope of the mountain. This wind field pattern also resembles observations (Fig. 5.20) by Kurz (1990) for a front approaching Alps from a similar direction as the simulated front relative to the idealized mountain barrier in Fig. 5.19. The wind field in Fig. 5.20a also has a maximum convergence zone on the northern slope of the Alps, due to the combination of the pre-frontal flow over the mountain from the south and the post-frontal flow from the west. The numerical simulation indicates the temperature gradient of the cold front is weakened on the northwestern slope of the mountain (Fig. 5.19a).

When the front is at about the center of the mountain at $t = 66$ h (Fig. 5.21), a frontal region develops on the northeastern slope of the mountain due to the mountain-induced stretching deformation forcing of the pre-frontal flow. In the meantime, the post-frontal wind from the northwest is impinging almost normal to the terrain contour at the northwest corner of the mountain. Thus, a frontogenesis region is also induced on the southwestern slope, which is the lee-side for this post-frontal flow. The horizontal frontal structure is thus deformed by the combination of the frontogenesis regions on the northeastern slope and southwestern slope. This will be shown more clearly by the frontogenetic forcing and the divergence field in the next section.

When the northern part of the front has moved to the eastern slope at $t = 72$ h (Fig. 5.22), the post-frontal westerly wind dominates and the maximum frontal region shifts to the southeastern side of the mountain. The

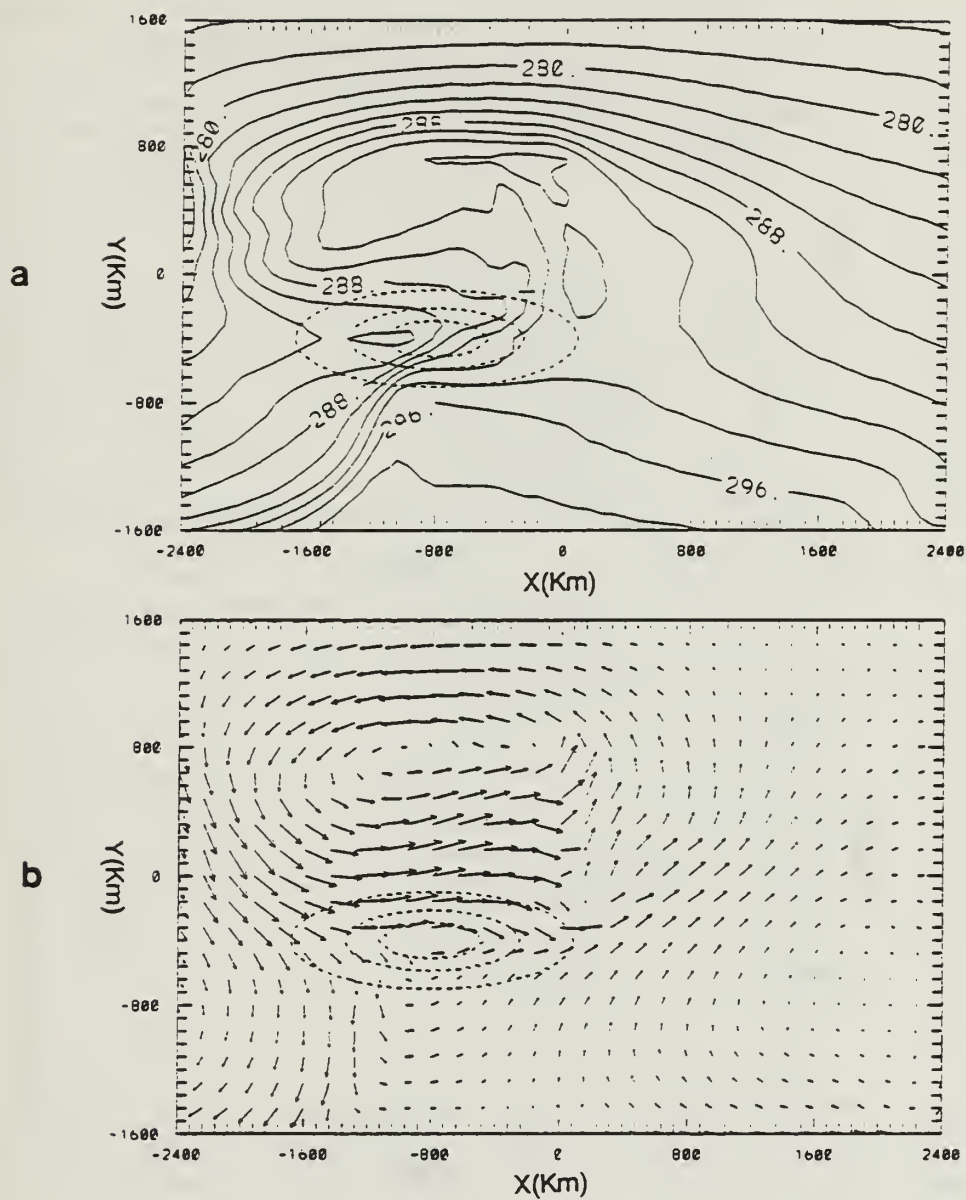


Fig. 5.21 Frontal solution for Case 3 at $t = 66$ h when the cold front is on the mountain, (a) sea-level temperature (b) surface wind vector (maximum = 43 m/s)

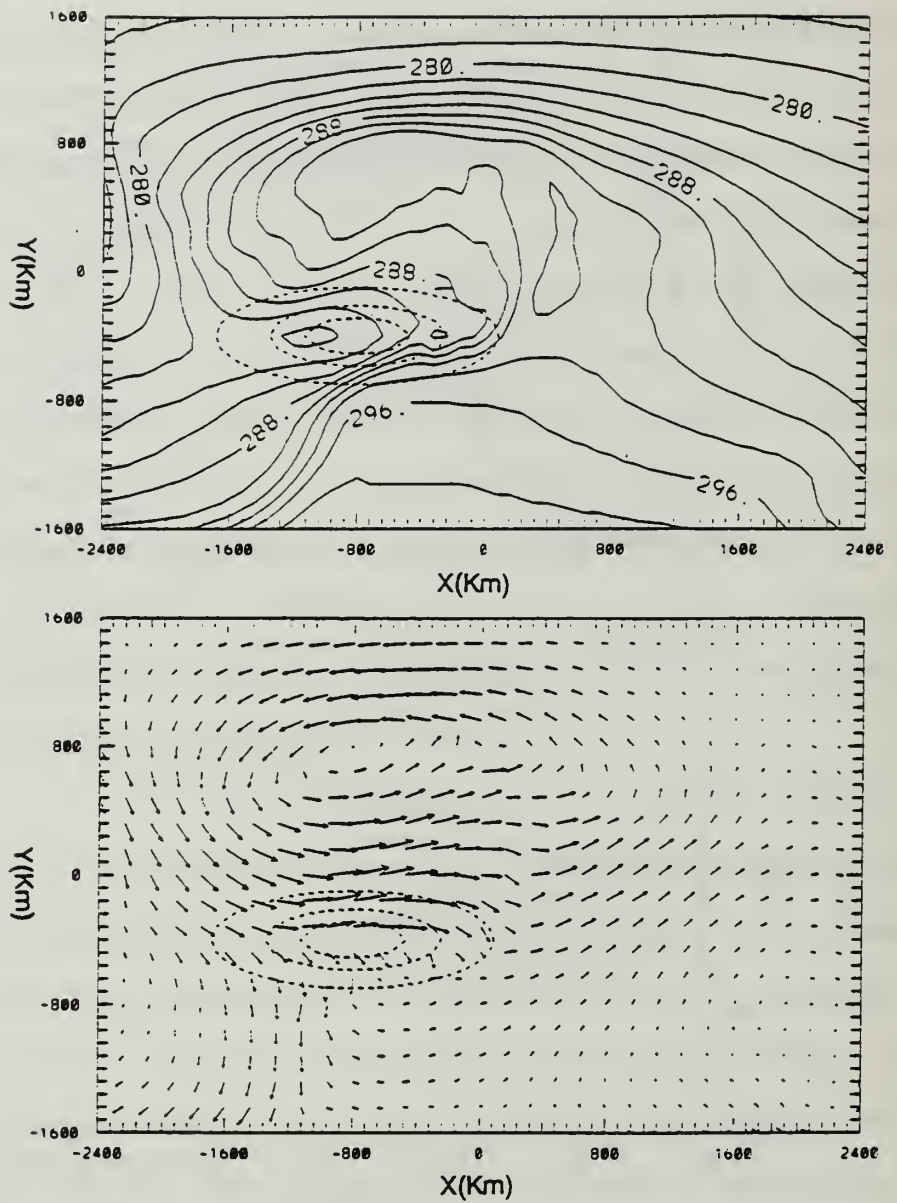


Fig. 5.22 As in Fig. 5.21, except for $t = 72$ h.

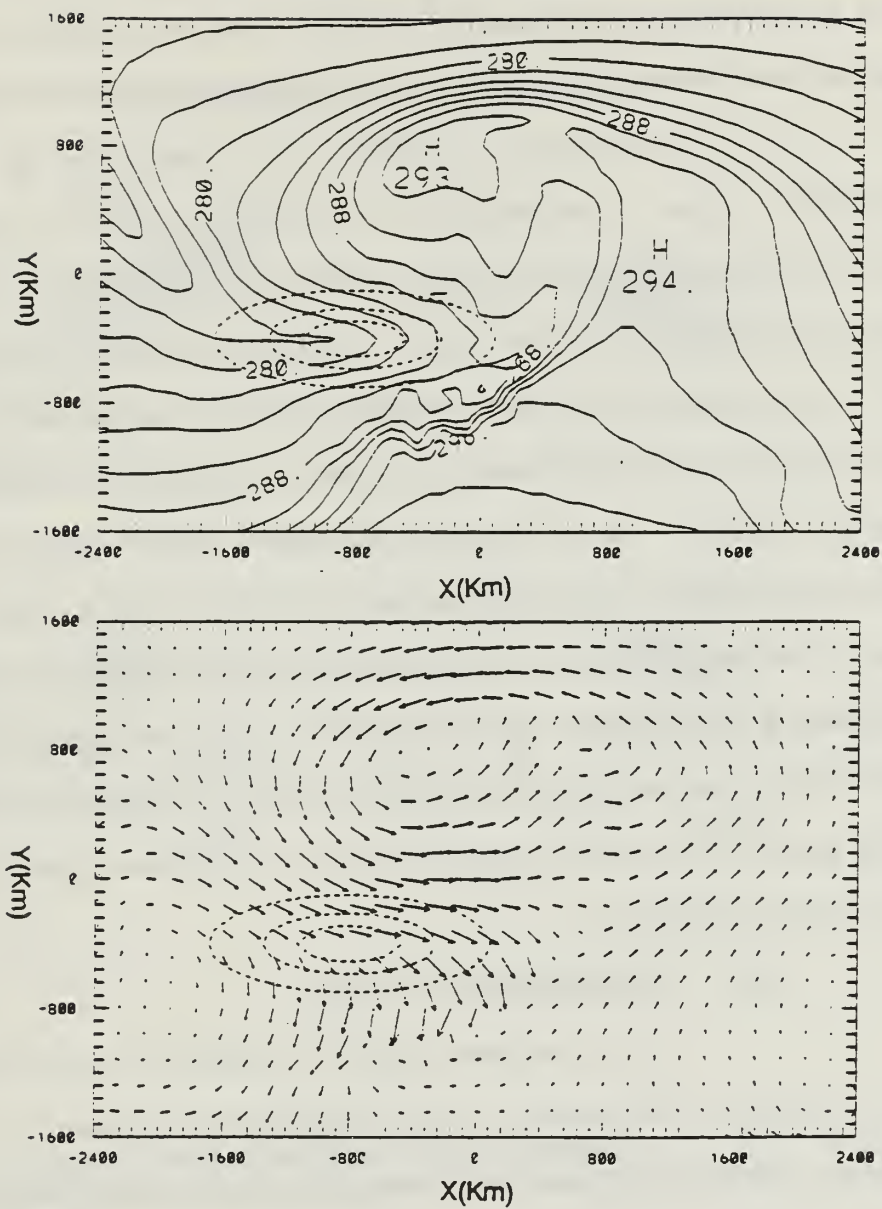


Fig. 5.23 As in Fig. 5.21, except for $t = 84$ h when the front is away from the mountain.

temperature gradient in the front is further intensified (Fig. 5.22a) and a larger wind shear is associated with the front (Fig. 5.22b). Since the maximum frontal intensity stays on the southern slope, the front is deformed to be parallel to the mountain.

The front continues to be intensified as it leaves the southeastern region of the barrier at $t = 84$ h (Fig. 5.23). A major difference between this case and previous cases is that the strong downslope winds on the lee side are more toward the south rather than toward the east in other cases. Since east is the direction of advection, the front in this case moves much slower toward the east. Because the front stays longer within the lee-side convergence zone, its intensity is larger. The convergence/divergence fields along with the frontal positions for different times are shown in Fig. 5.24. By $t = 96$ h (Fig. 5.17), when the fronts in the previous cases have all weakened to their original intensities, the front in this case is still enhanced. It is not until $t = 108$ h (not shown) when the front leaves the lee-side convergent zone that the frontal structure is restored to its original pattern. In this case, there has been a net increase in the frontal intensity due to the mountain effect.

b. Frontogenetic Forcing

As in previous cases, the maximum frontogenetic forcing occurs generally on the leeside of the impinging flow associated with the frontal circulation. Due to the shape of the mountain and its orientation with respect to the frontal circulation, the frontogenetic processes (Fig. 5.25) are more complicated than in the previous cases. The horizontal deformation term corresponding to the flow at $t = 54$ h is shown in Fig. 5.25 a. At this time, the prevailing flow toward the mountain is the southwesterly pre-frontal flow and this leads to a maximum forcing on the northeastern slope. At $t = 60$ h (Fig. 5.25b), the position of the maximum

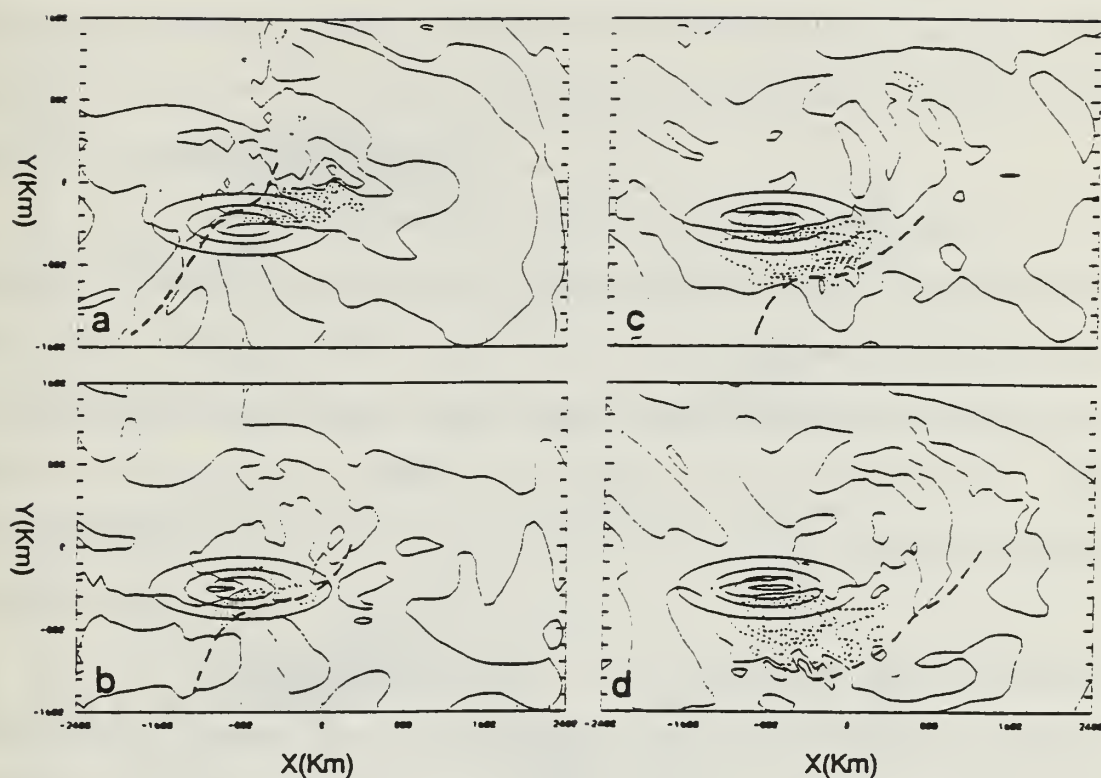


Fig. 5.24 Case 3. Divergence fields (contour interval = $0.2 \times 10^{-4} \text{s}^{-1}$) and cold front positions (heavy dashed line) at (a) $t = 66 \text{ h}$, (b) $t = 72 \text{ h}$, (c) $t = 78 \text{ h}$ and (d) $t = 84 \text{ h}$.

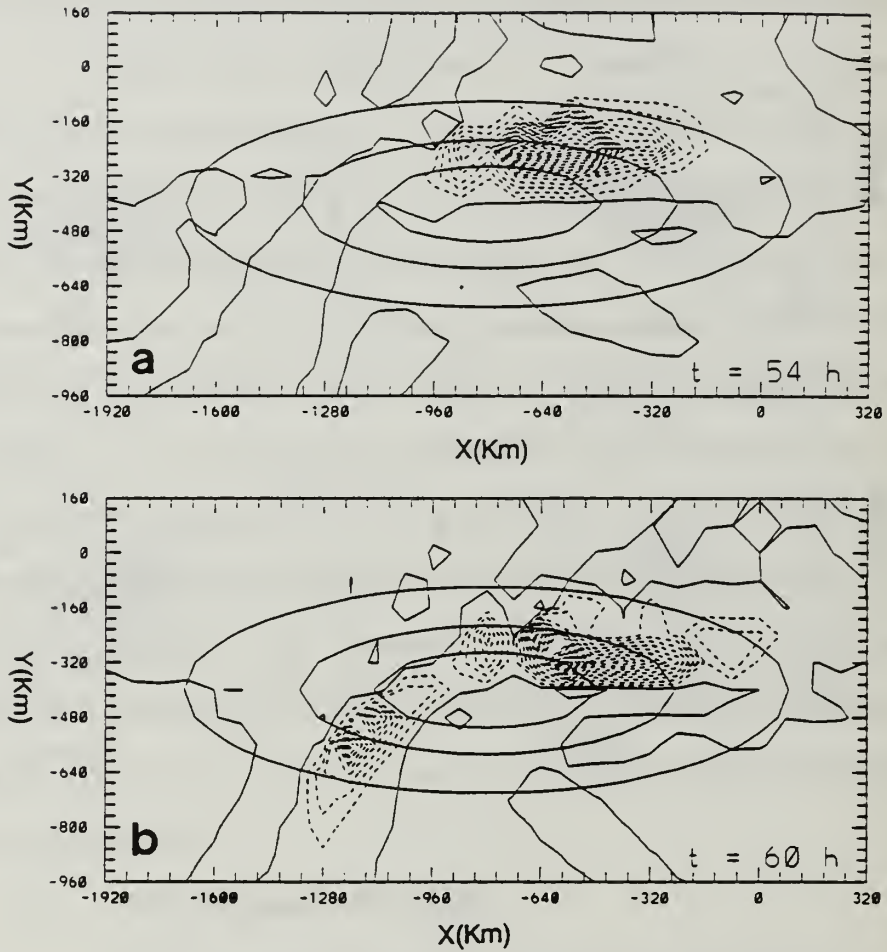


Fig. 5.25 Horizontal deformation forcing ($\circ K^2 m^{-2} s^{-1}$) on level $\sigma = 0.99$. in the region of frontogenesis (dashed lines) and in the region of frontolysis (solid line) at : (a) $t = 54$ h with minimum values of -1.3×10^{-13} associated with the cold front and -0.25×10^{-14} in the mountain area, contour interval = 0.1×10^{-12} ; (b) $t = 60$ h, maximum forcing on northeastern slope with a minimum value of -0.31×10^{-12} , contour interval = 0.1×10^{-12} .

forcing on the northern side moves slightly eastward. At the same time, another frontogenesis region on the southwestern slope of the mountain is induced by the post-frontal northwesterly that is impinging on the northwestern corner of the mountain. Therefore, this second frontogenesis region is located exactly on the leeside of this impinging flow.

The frontogenesis region on the northern slope in this simulation resembles the frontogenesis function computed from the observational data by Kurz (1990) as shown in Fig. 5.20b. In Kurz's explanation, the cold air is advected from the west against the warm foehn air on the northeastern slope that is created by the downslope motion on the leeside of the pre-frontal flow. This increases the temperature gradient on the northern slope. The explanation can also be applied here.

The major contribution to the frontogenetic forcing in this case is the stretching forcing (Fig. 5.26). The shearing deformation is about an order of magnitude smaller than the stretching forcing. Therefore, the magnitude of the stretching deformation forcing is nearly identical to that of the horizontal deformation forcing. The magnitude of the tilting term in this adiabatic experiment is much smaller than the other terms (Fig. 5.26).

The divergence field (Fig. 5.24) has a convergent zone on the lee-side corresponding very well with the frontogenetic forcing in Fig. 5.26. Therefore, the major mechanism of frontogenetic forcing is contributed by the convergence associated with mountain-induced motion, i.e. the stretching deformation effect. This frontogenesis region on the southern slope was not reported in Kurz's (1990) analysis. One possible reason is the lack of sufficient data. The other possible reason is that the Alps are not an elliptical-shaped mountain (see

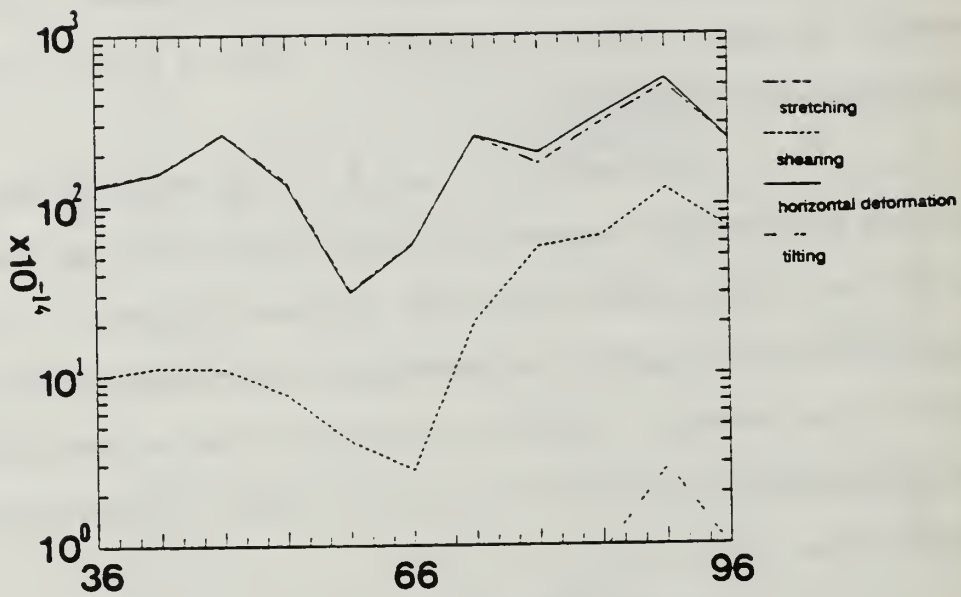


Fig. 5.26 Time (h) evolution of the maximum stretching, shearing, total horizontal deformation and tilting forcing at $\sigma = 0.99$ during the cold front passage over the east-west oriented mountain (Case 3). Ordinate has a logarithmic scale (unit: $^{\circ}\text{K}^2\text{m}^{-2}\text{s}^{-1}$).

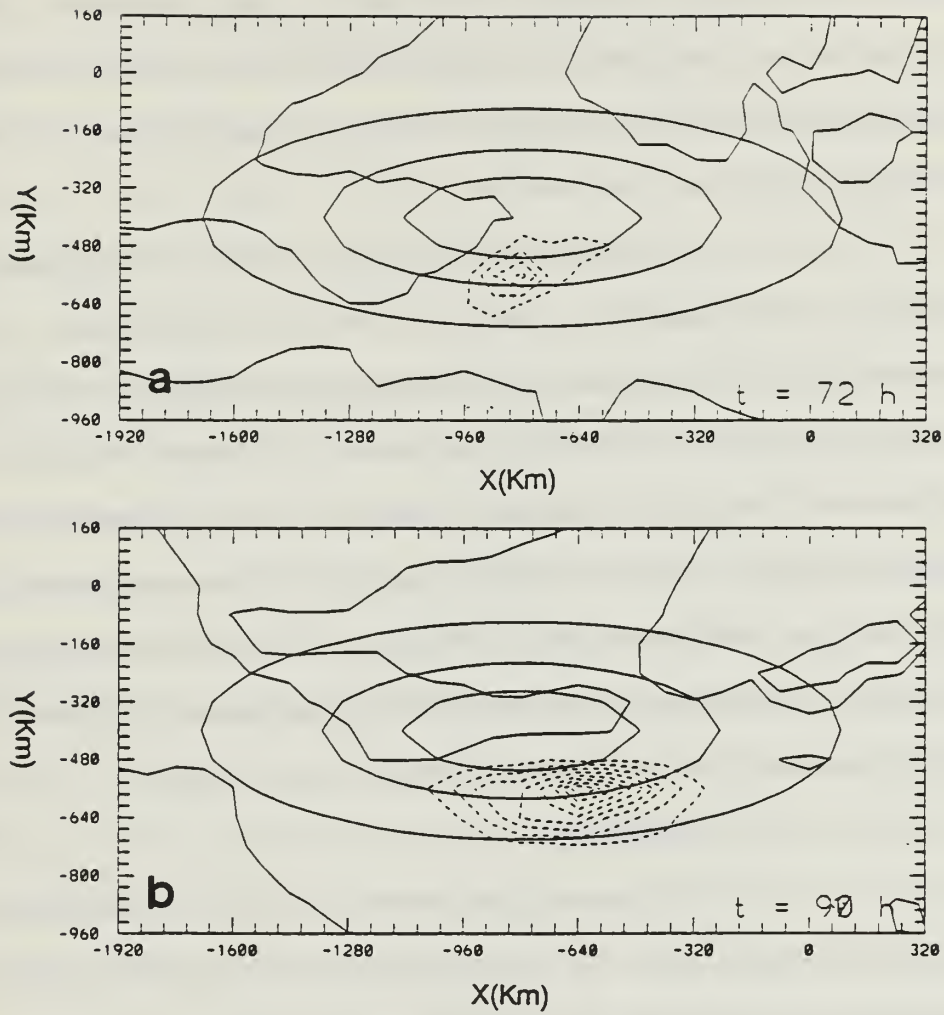


Fig. 5.27 Horizontal deformation as in Fig. 5.25, except for (a) $t = 72 \text{ h}$, contour interval = 0.6×10^{-12} (unit: $^{\circ}\text{K}^{-2}\text{m}^{-2}\text{s}^{-1}$)

Fig. 5.20), especially where the terrain in the southwestern end of the Alps turns toward the southwest direction and curves counterclockwise. This shape of topography may contribute to a large shearing deformation that may offset the stretching term on the southern side of the Alps. A simulation with detailed terrain profiles is needed for further study.

After the front has passed over the mountain crest, the dominating post-frontal flow pushes the maximum deformation forcing to the southern slope of the mountain. The frontogenetic forcing at $t = 72$ h and $t = 90$ h are shown in Fig. 5.27. The frontogenetic forcing at $t = 90$ h is shifted farther to the southeastern slope and is more intense than at $t = 72$ h. The stretching term still dominates and is one order of magnitude larger than the shearing term (not shown). The divergence field shown in Fig. 5.24 indicates more clearly the regions where the front would experience the frontogenesis and frontolysis. The frontolysis is much smaller than that in the frontogenesis during the entire period.

c. Summary

The orientation of the mountain in this case makes the mountain a long barrier for the wind in the north-south direction. Even before the front arrives, a frontogenetic forcing is created on the northern slope of the mountain due to the pre-frontal southerly wind that goes over the mountain and produces a strong downslope wind. This is consistent with the observation of a frontal passage during an IOP (Intensive Observation Period) of the German experiment over the Alpine region (Kurz 1990). Meanwhile, the post-frontal northwesterly wind impinging on the northwestern corner of the mountain subsequently induces another leeside frontogenesis region on the southern slope of the mountain. When the front is on the mountain, the dominant wind effect is due

to the post-frontal wind that has a component parallel to the mountain and a component going over the mountain. This post-frontal wind contributes to the horizontal deformation part of the frontogenetical forcing and induces frontogenesis forcing on the southeastern part of the mountain. The frontogenesis processes generated on different regions of the mountain cause the frontal structure to be deformed in several directions by the superposition with the approaching front.

In previous more idealized studies such as Blumen and Gross (1987b), Blumen (1992) and Schumann (1987), the deformation of the front near the mountain was explained by the mountain-induced anticyclonic circulation on the mean flow that accelerates the front on the northern slope and decelerates it on the southern slope. Blumen (1992) also suggested that a weak front may act more like a passive scalar, while a strong front may have some 'interactions' with the mountain. In reality, a cold front may have a horizontal wind speed up to 25 - 30 m/s on the surface, which is much larger than the mean flow. In the present numerical simulation, it is the frontogenesis process that occurs at different locations due to the varying prevailing winds associated with the significant pre- and post-frontal flows that deform the horizontal frontal structure. This can be seen clearly by the time history of the d -value distribution (Fig. 5.17). After the front has moved away, there is a front-like disturbance left behind on the slope.

At $t = 72$ h, the northern part of the front is about 350 km ahead of the front in the case with no mountain. The central part of the front is 350 km behind and the southern part is at about the same place as it is in the case with no mountain. Due to the orientation of this mountain, the major downslope wind is toward the south and the frontal position is behind other cases with the mountains. This horizontal frontal distortion, plus the acceleration and retardation, are commonly observed in the Alps region (Smith 1987).

4. Case 4: North-south Oriented Mountain Ridge

a. Analysis of The Results

The mountain in this experiment is north-south oriented with the horizontal scales $a_{0x}=240$ km and $a_{0y}=720$ km in the x and y directions, respectively. The major axis of the mountain is normal to the mean flow, but the front is oriented in the northeast-southwest direction, which is not parallel to the mountain.

The time evolution of the frontal d-value (Fig. 5.28) has a weakening of the intensity as the front arrives on the mountain at $t = 54$ h. A significant acceleration of the translation speed apparently occurs when the front passes over the mountain crest, and on the eastern side of the mountain between the period of $t = 60$ h and $t = 72$ h. There is also a second phase of weakening on the frontal intensity east of the mountain between $t = 84$ h and 96 h.

The frontolysis and frontogenesis on the western and eastern slopes of the mountain, respectively, can also be seen in the temperature fields (Fig. 5.29a and Fig. 5.30a). When the northern part of the front reaches the mountain at $t = 54$ h, the horizontal temperature gradient on the western slope is weakening. As soon as the front passes over the mountain crest, the horizontal temperature gradient is recovered on the eastern slope (Fig. 5.30a). The surface wind field (Fig. 5.29b) has an anticyclonic turning and has a maximum wind speed of 38 m/s on the leeside of the mountain. This anticyclonic flow is highly ageostrophic (not shown) as in the two-dimensional mountain study (Williams *et al.* 1992).

By $t = 72$ h, the front has moved away from the mountain but its intensity continues to increase (Fig. 5.28) and it is pushed rapidly eastward by the strong downslope wind. By $t = 84$ h, the front has left the lee-side convergent zone

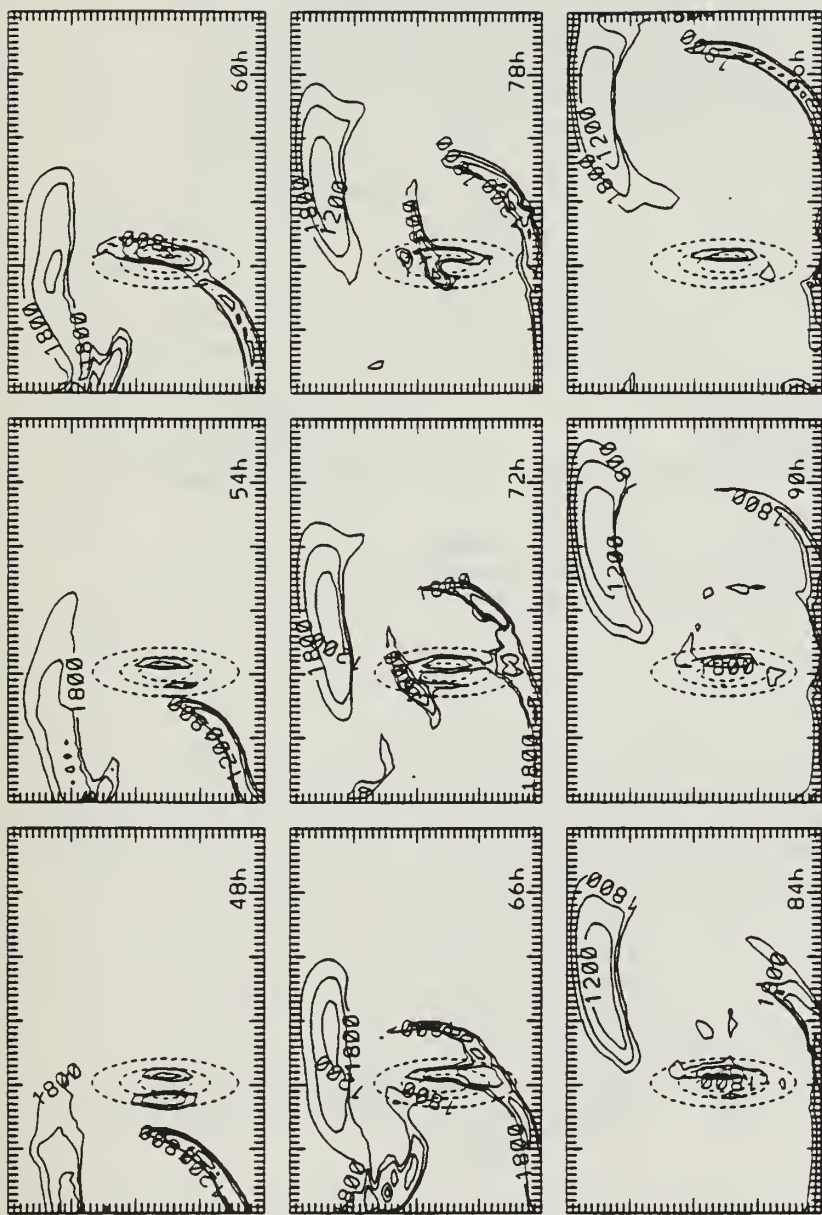


Fig. 5.28 Time evolution each 6 h from $t = 48$ h to $t = 96$ h of the d-value (km) of a front passage over the north-south oriented mountain in Case 4.

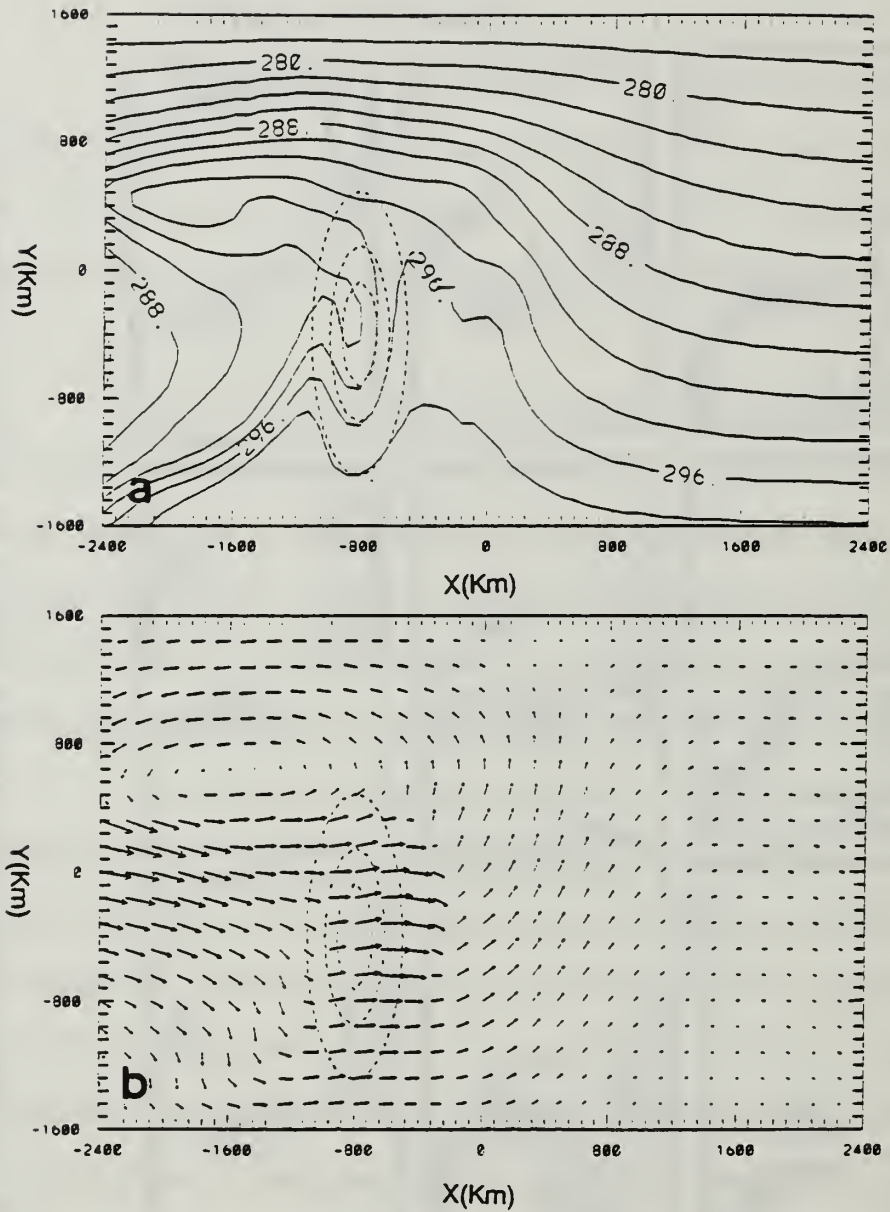


Fig. 5.29 Frontal system over the north-south oriented mountain (Case 4) at $t = 54$ h: (a) sea-level potential temperature ($^{\circ}\text{K}$); and (b) terrain surface wind with the maximum wind speed of 38 m/s.

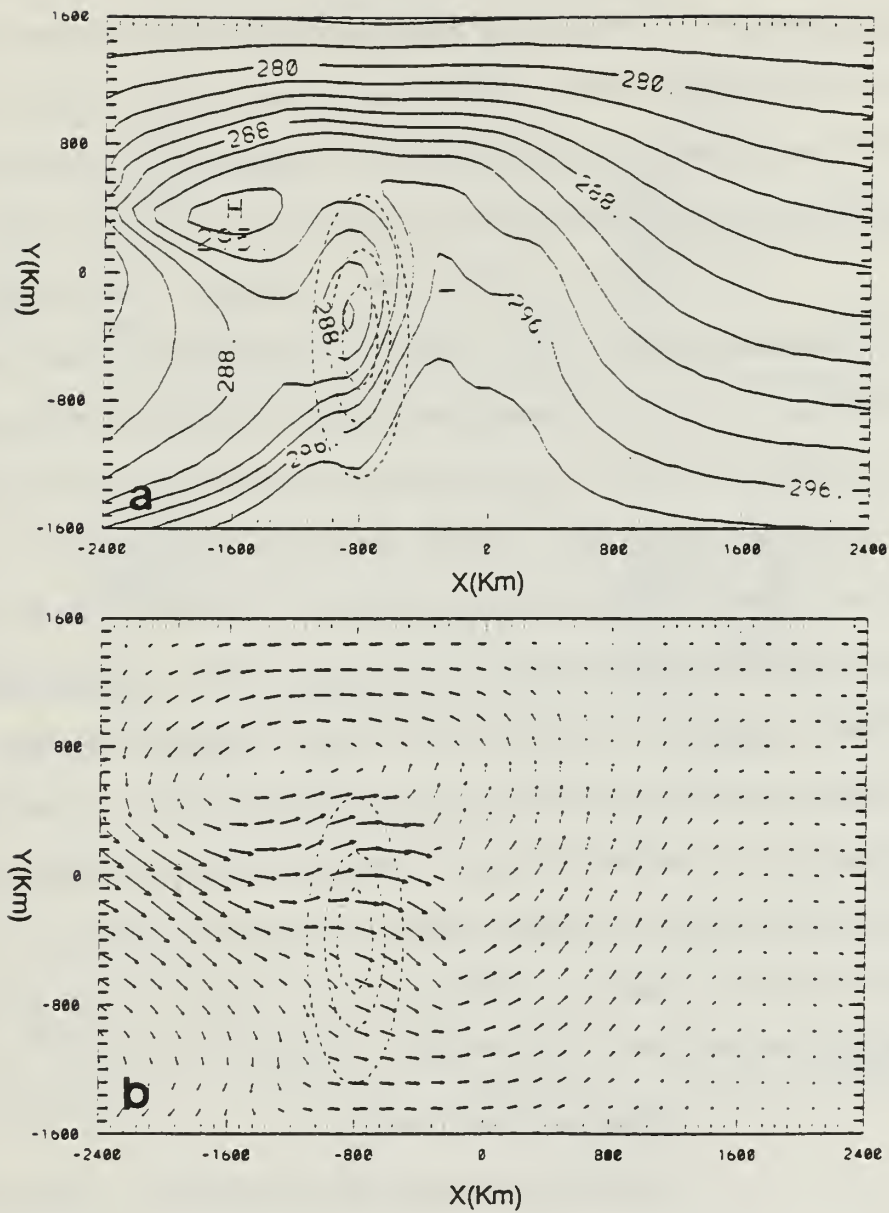


Fig. 5.30 Frontal solution for Case 4 as in Fig. 5.26 except for $t = 60$ h and maximum wind vector = 40 m/s.

and entered the divergent zone farther downstream (Fig. 5.31) so that its intensity starts to decrease. At $t = 96$ h, the front has left the divergent zone and its intensity returns to the original value. The divergence field shown in Fig. 5.31 is similar to the flow over the same mountain in Fig 3.8b. Therefore, the mountain-induced flow is essential to explain the dynamics associated with the frontal changes.

Vertical cross-sections of potential temperature (Fig. 5.32a) and y-component velocity v' (Fig. 5.32b) reveal a leeside wave that is slightly tilted to the upstream. The large horizontal temperature gradient in the frontal zone has a position that is consistent with the frontal v' wind shear at the foot of the upslope (Fig. 5.32a and Fig. 5.32g). When the front moves up the mountain, the temperature gradient is weakened and reaches the minimum values when the front is on the top of the mountain (Fig. 5.32c and Fig. 5.32i). Meanwhile, even though the frontal temperature is reduced substantially on the upwind slope, its existence and position can still be identified by the horizontal shear on north-south wind. After passing over the top, the frontal wind shear moves downslope rapidly to the bottom of the mountain, and holds until the temperature gradient recovers. This is consistent with the results of Williams *et al.* (1992) for the two-dimensional mountain.

b. Frontogenetic Forcing

The horizontal deformation term of the frontogenetic forcing for $t = 54$ h and 60 h is shown in Fig. 5.33. At $t = 54$ h, the front has reached the mountain and the prevailing wind is dominated by the pre-frontal southwesterlies. This pre-frontal flow induces frontolysis on the east side slope just beyond the mountain crest and frontogenesis further downstream. This is similar to the mesoscale circular mountain circulation case because the mountain dimensions in

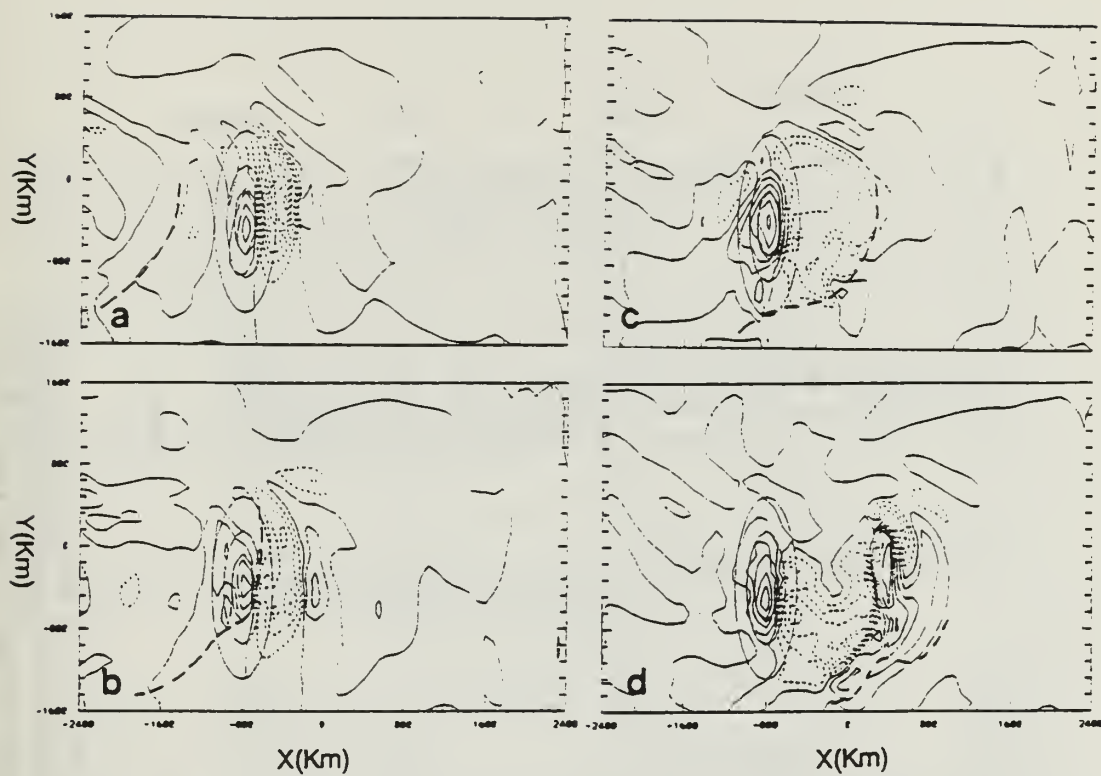


Fig. 5.31 Divergence fields and cold front positions (heavy dashed line) for Case 4: (a) $t = 48$ h, (b) $t = 60$ h, (c) $t = 72$ h and (d) $t = 84$ h, with contour interval $= 0.2 \times 10^{-4} \text{ s}^{-1}$.

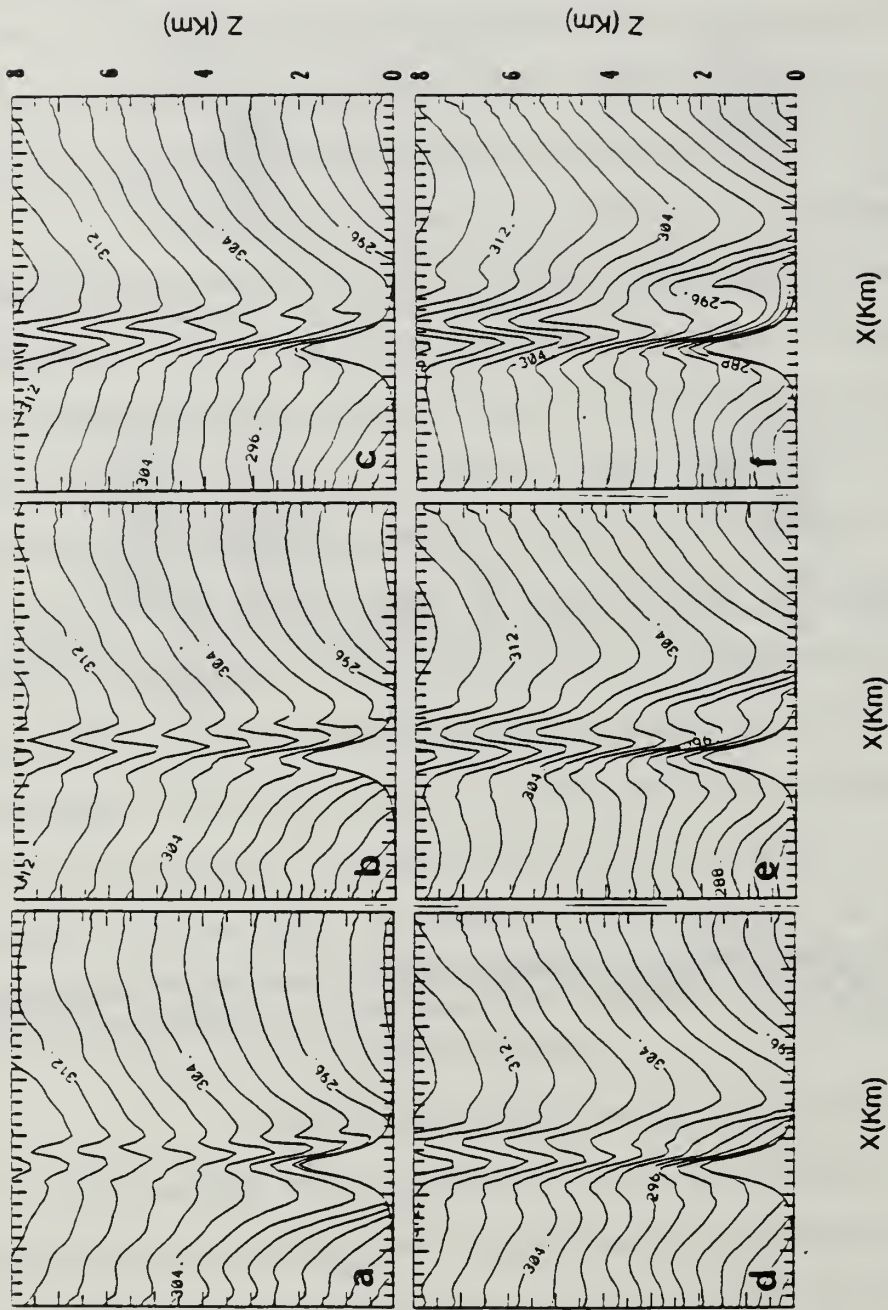


Fig. 5.32 Vertical cross-section through the center of the north-south oriented mountain for potential temperature (panels a to f) and v' (panels g to l), during the frontal passage. The horizontal domain is 5600 km with tick markers at 80 km. Panels (a) to (f) for the potential temperature and (g) to (l) for the north-south wind v' correspond to $t = 48, 54, 60, 66, 72$ and 84 h, respectively. The contour interval is 2° in panels (a) to (f), 3 m/s in panels (g) to (k), and 6 m/s in panel (l). Positive v' is toward the north.

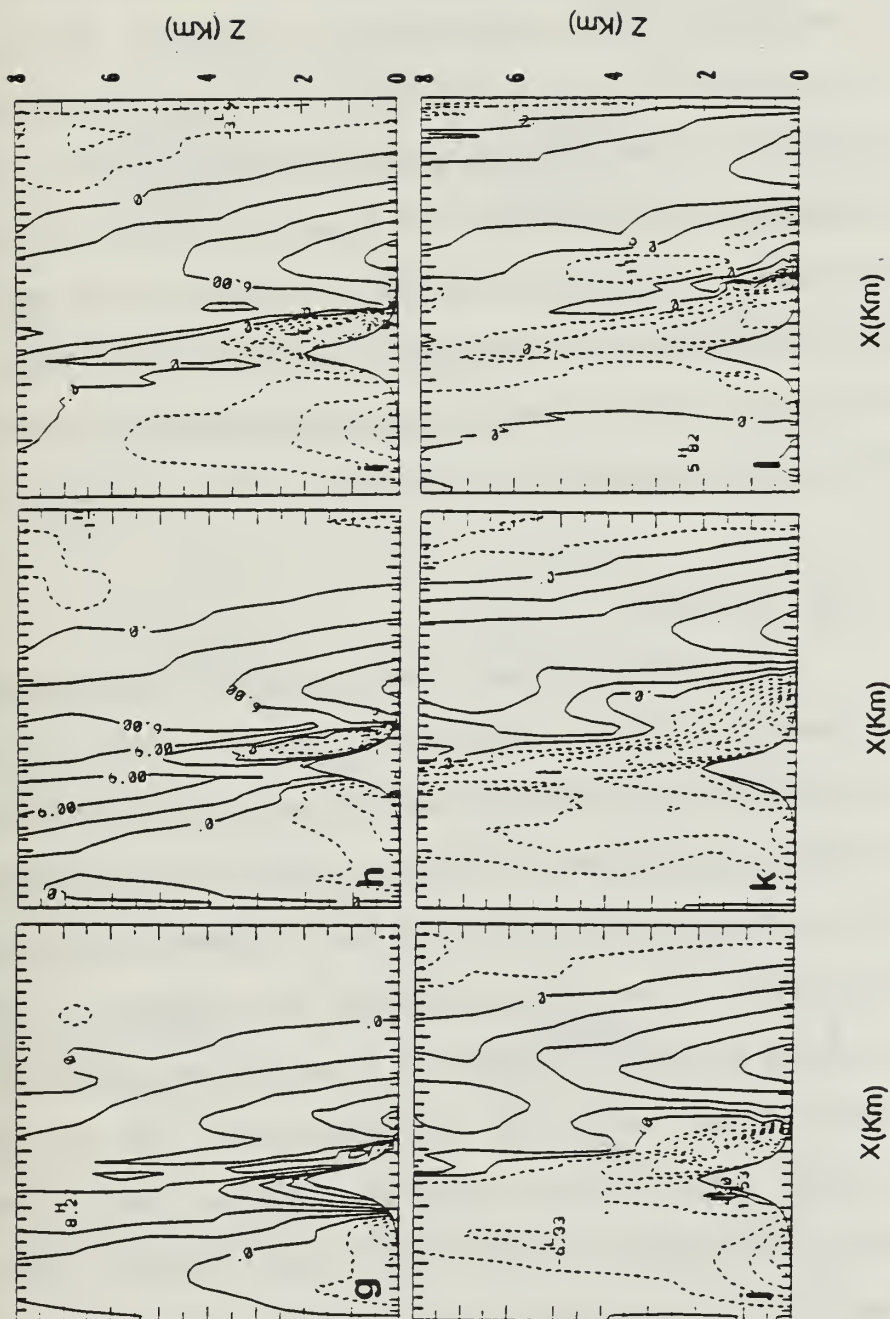


Fig. 5.32 (Continued)

the x-direction are the same for these two cases. The major contribution to the frontogenesis on the eastern slope comes from the stretching deformation, which indicates that the frontal forcing is mainly due to the convergence. The divergence field for $t = 54$ h is given in Fig. 5.31a. This diagram corresponds very well with the frontogenetic forcing and shows more clearly the region where the front experiences frontolysis/frontogenesis. At $t = 72$ h, the front has moved away from the mountain rapidly, but the mountain circulation is still under the influence of the post-frontal wind. The pattern of frontogenetic forcing on the eastern slope of the mountain is similar to the forcing at $t = 54$ h. Another frontogenesis region on the northwestern corner (Fig. 5.33e and f) is induced by the around the mountain effect of the post-frontal flow.

c. Summary

Due to the north-south orientation of the mountain relative to the front, the results in this case are similar to the two-dimensional studies (Williams *et al.* 1992). First, the frontogenesis effect generated by the pre-frontal flow is weak so that it has little effect on the front. Second, the post-frontal wind is nearly normal to the mountain ridge so that the major frontolysis/frontogenesis is aligned with the mountain ridge, which is similar to the two-dimensional studies. When the front moves to the eastern slope, it is deformed to be aligned with the mountain orientation, i.e. north-south, by superposition with the leeside frontogenesis region. After the front leaves the mountain area, the original northeast-southwest orientation is restored (Fig. 5.28). However, two large temperature gradient areas remain in the mountain vicinity on the northwest corner and along the eastern slope. The former area is generated by the shearing deformation while the latter is induced by the stretching deformation.

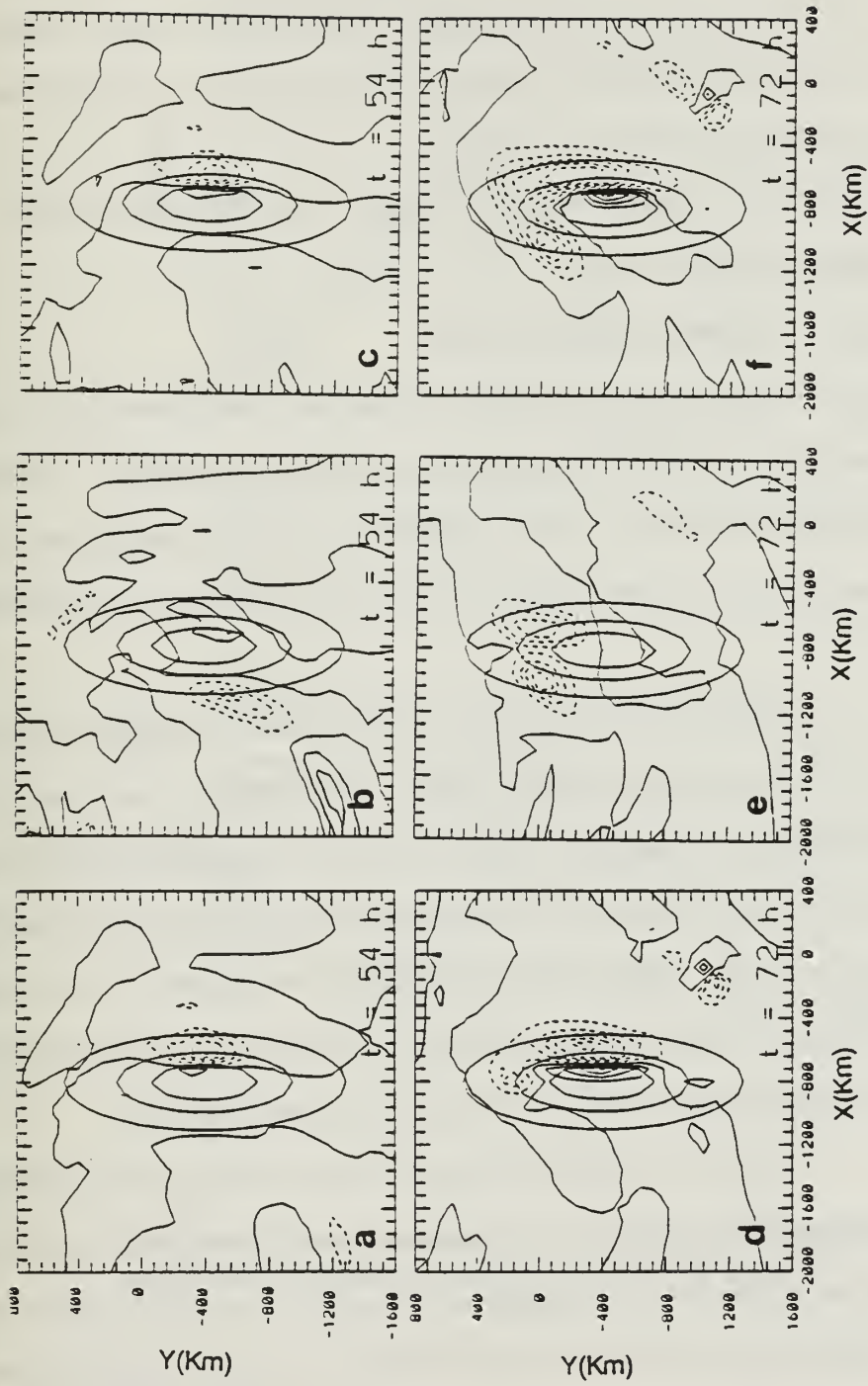


Fig. 5.33 Frontogenetic forcing terms at $t = 54$ h, (a) to (c) and at $t = 60$ h, (d) to (f). (a) and (d) are the stretching deformation, (b) and (e) are shearing deformation, and (c) and (f) are the total horizontal deformation forcing (sum of a and b or d and e). contour interval is 0.25×10^{-13} (Unit: $\text{K}^2 \text{m}^{-2} \text{s}^{-1}$)

The final position of the front is at about the same location as in Cases 1 and 2 and is about 800 km ahead of the frontal position without the mountain. This is because the front is pushed eastward by the post-frontal flow that induces strong downslope winds on the leeside.

5. Case 5: Mountain with The Major Axis Parallel to The Approaching Front

a. Analysis of The Results

The mountain structure in this case is the same as in Cases 3 and 4, except that the orientation of the mountain is rotated 45 degrees. Therefore, the orientation of the mountain is nearly parallel to the approaching cold front. This configuration should be most similar to a front passing over a two-dimensional ridge.

Before the front reaches the mountain, the southwesterly pre-frontal flow is parallel to the mountain ridge. Consequently, the front is not influenced by the mountain during this stage, and the corresponding diagrams will not be shown. The incident flow to the mountain is from the southwest end and this wind component is small. The induced anticyclonic flow is more like a quasi-geostrophic solution of the mountain circulation. The maximum ageostrophic wind is located on the mountain top and is symmetric to the mountain crest.

When the cold front arrives at the mountain, the horizontal temperature gradient of the front on the western slope is weakened. The post-frontal northwesterly flow has an anticyclonic curvature over the mountain ridge (Fig. 5.34b), which reduces the frontal wind shear and causes a westerly flow to penetrate the weakened frontal zone. When the cold front passes over the

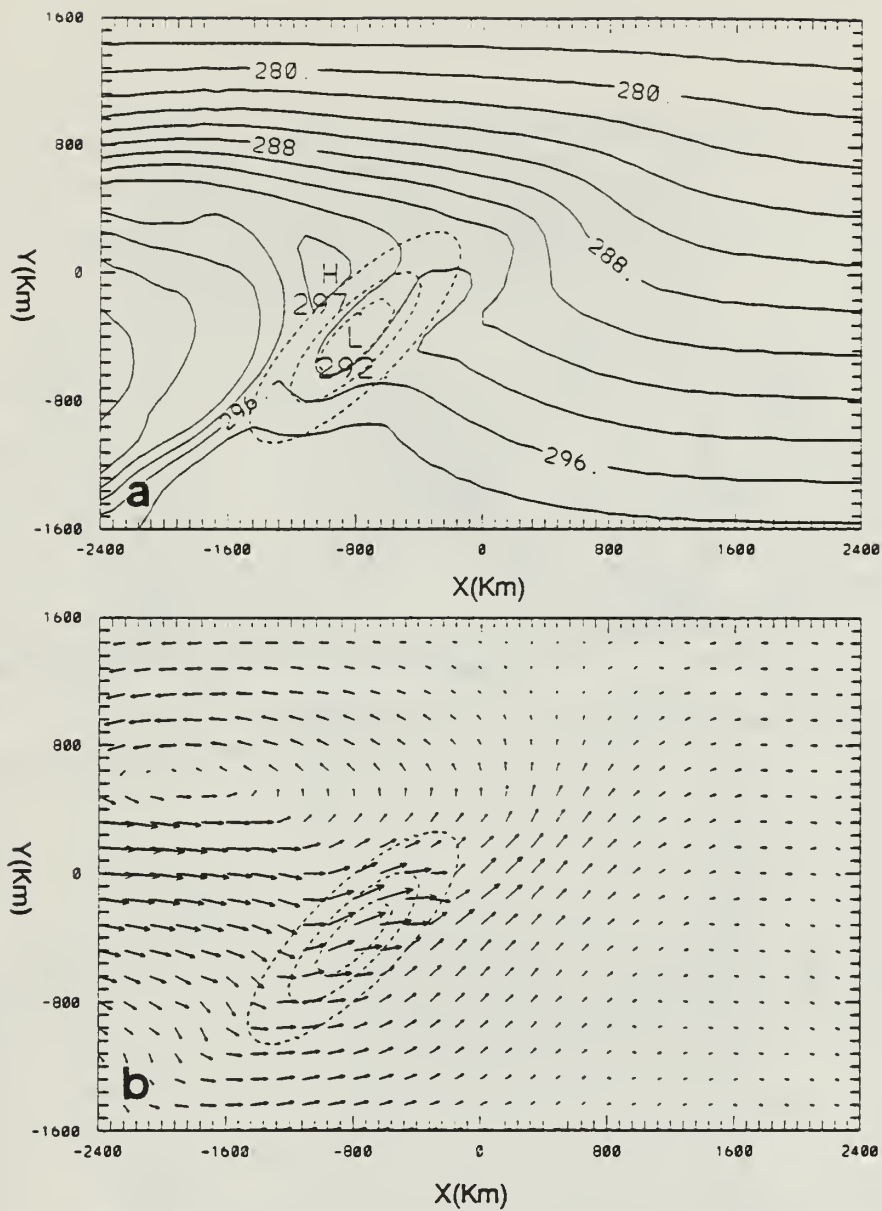


Fig. 5.34 Case 5. Frontal solution at $t = 50$ h: (a) sea-level temperature ($^{\circ}\text{K}$); (b) surface wind vector (maximum vector = 34 m/s).

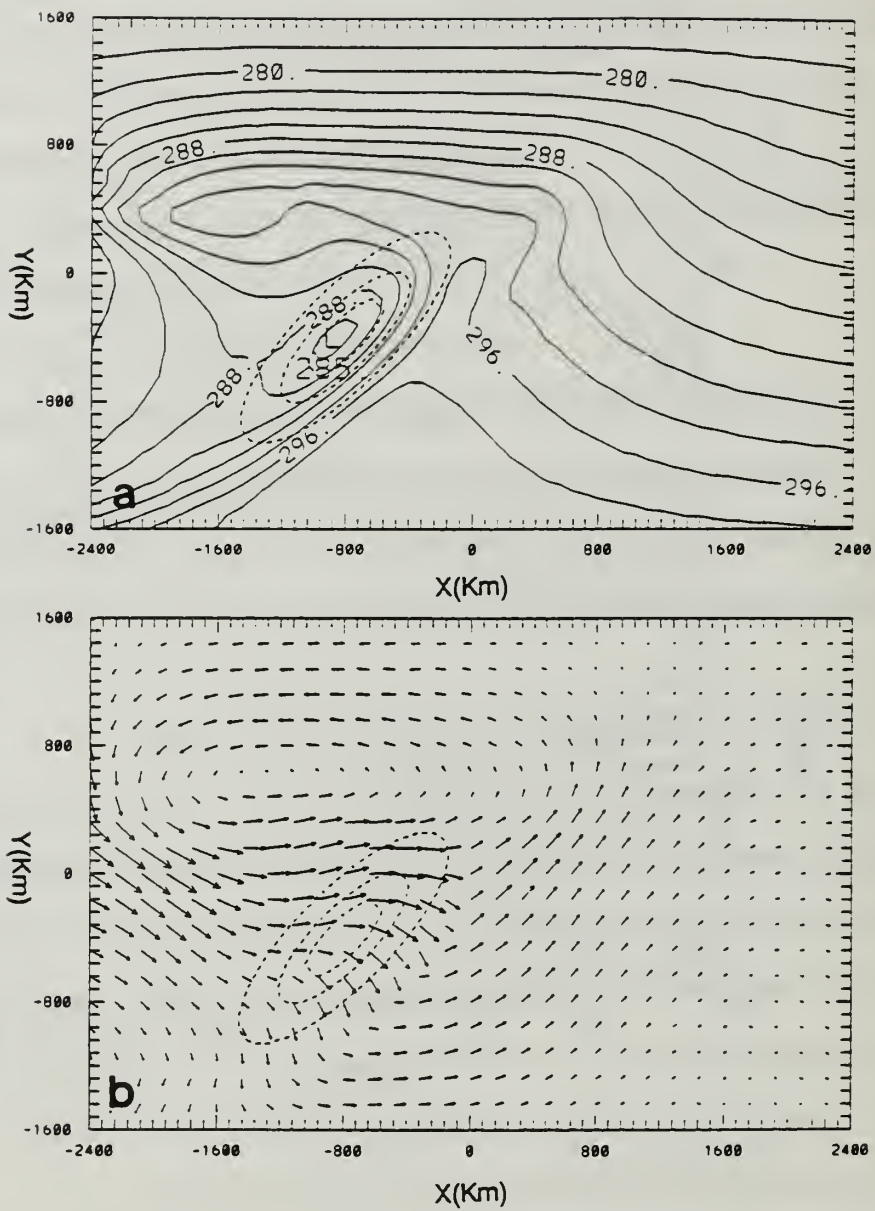


Fig. 5.35 As in Fig. 5.34, except for $t = 60$ h and maximum vector = 40 m/s.

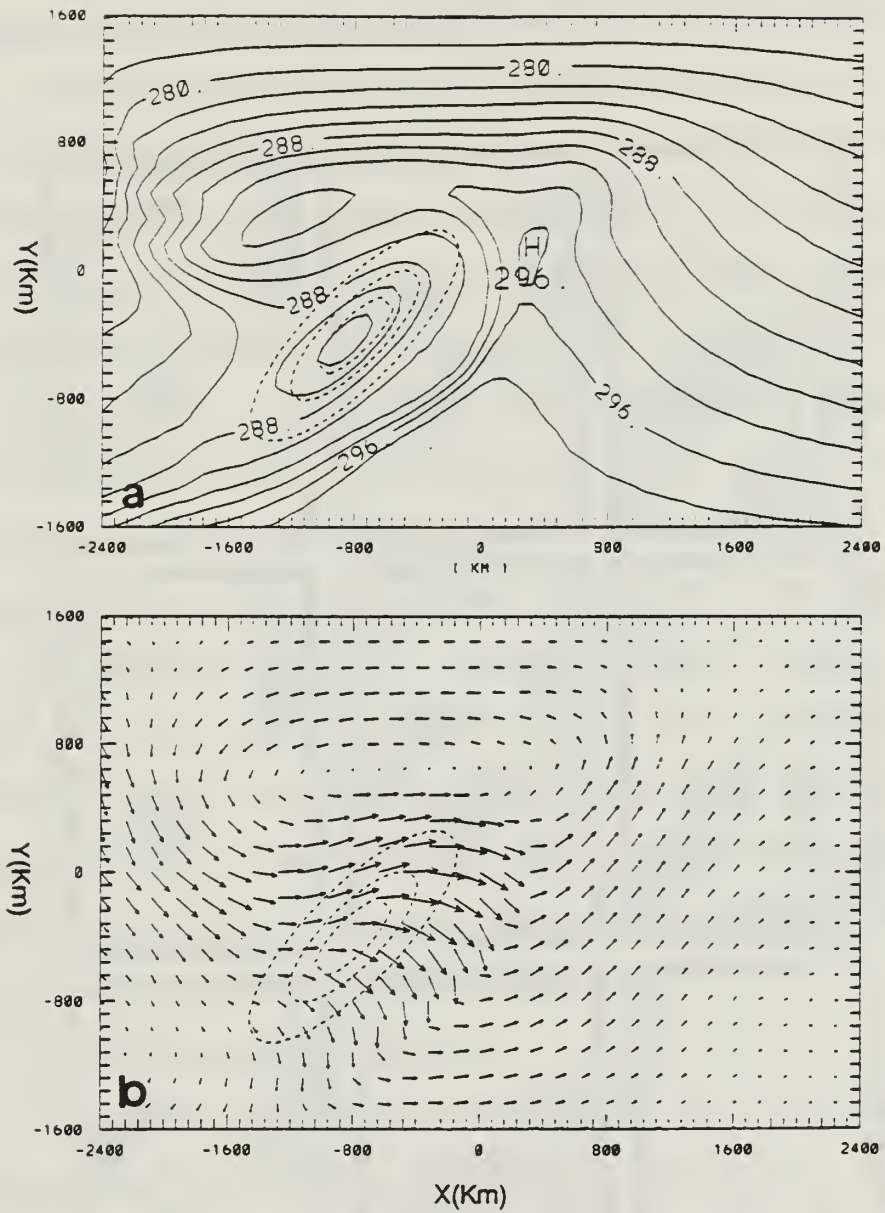


Fig. 5.36 As in Fig. 5.35, except for $t = 66$ h and maximum vector = 41 m/s.



Fig. 5.37 Time evolution each 6 h from $t = 48$ h to $t = 96$ h of the d-value (km) of a front passage over the northeast-southwest oriented mountain in Case 5.

mountain at $t = 60$ h, its intensity is recovered and further increased (Fig. 5.35a). The wind shear associated with the front is enhanced by the strong downslope wind (Fig. 5.35b). Since the lee-side frontogenesis is aligned with the original frontal orientation, the front does not experience much deformation at this stage. At $t = 66$ h, the central part of the front is pushed slightly faster by the downslope wind than the southern part (Fig. 5.36), and the front is distorted slightly. The frontal strength is intensified significantly. As in other cases, the front continues to intensify within the convergent zone downstream from the mountain until it reaches the divergent zone further downstream. Finally, when the influence of the mountain is weak, the front is restored to its original intensity. This time evolution of the frontal intensity and positions is summarized in Fig. 5.37. The cold front experiences little distortion in passing over this mountain. However, the acceleration of the cold front after passing over the mountain is significant. The second phase in the frontal weakening at $t = 90$ h occurs in the divergent zone farther downstream of the mountain (Fig. 5.38). This is because the northwesterly post-frontal flow is nearly normal to the major axis of the mountain and causes a significant and broad convergence area on the leeside.

b. Frontogenetic Forcing

The dynamics associated with this case are very similar to the previous case and will be discussed only briefly in terms of the horizontal deformation term of the frontogenetic forcing. When the front is located right on the eastern slope of the mountain at $t = 60$ h, the dominant wind is the post-frontal flow from the west that has an angle to the contour of the mountain (Fig. 5.35). The horizontal deformation forcing indicates a strong frontogenesis by the mountain on the leeside (Fig. 5.39). The frontolysis experienced by the front on the upwind slope

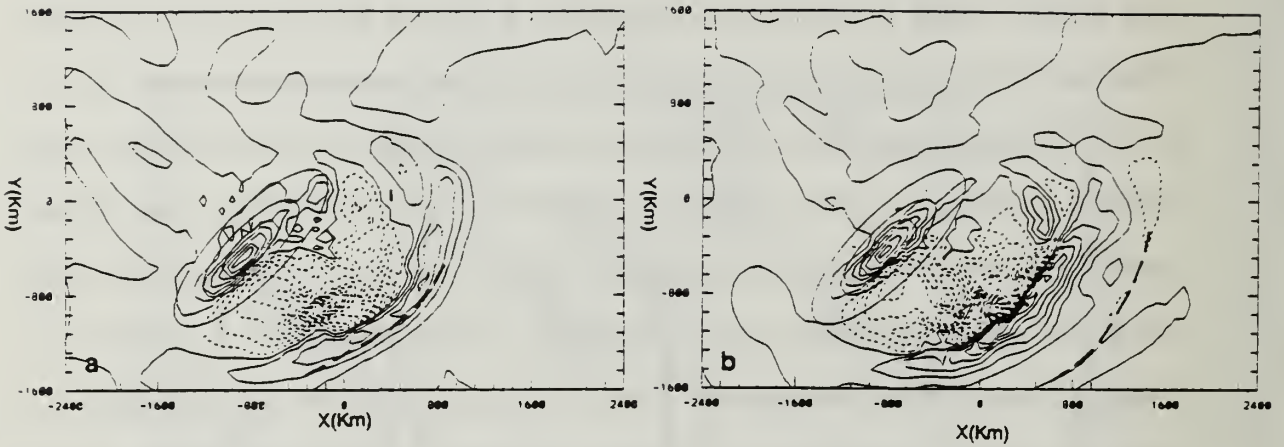


Fig. 5.38 Divergence (Contour interval = $0.2 \times 10^{-4} \text{s}^{-1}$) field for (a) $t = 84 \text{ h}$, (b) $t = 90 \text{ h}$. Dashed line indicates convergent zone and solid line indicates divergent zone. The heavy dashed line is the cold front position

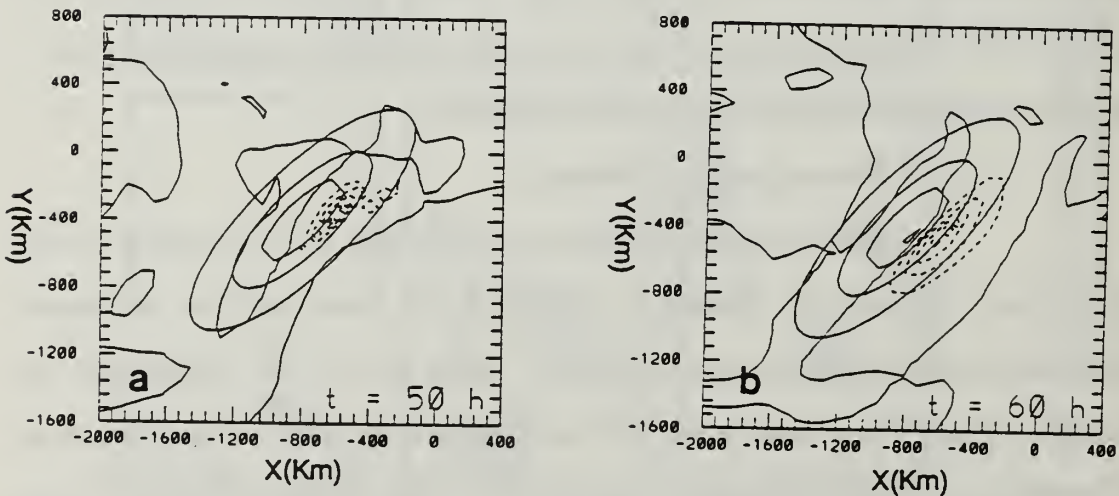


Fig. 5.39 Horizontal deformation forcing ($^{\circ} \text{K}^2 \text{m}^{-2} \text{s}^{-1}$) on level $\sigma = 0.99$. in the region of frontogenesis (dashed lines) and in the region of frontolysis (solid line) at : (a) $t = 50 \text{ h}$ with minimum values of -0.11×10^{-12} ; (b) $t = 60 \text{ h}$, maximum forcing on northeastern slope with a minimum value of -0.35×10^{-12} .

has a magnitude that is much smaller than the leeside frontogenesis. This forcing is contributed mainly from the stretching terms associated with the flow over the mountain (not shown).

c. Summary

Results in this case with the long-axis of the mountain nearly parallel to the front are similar to Case 4 and can be compared closely with previous two-dimensional studies. The major difference from Case 4 is that the front experiences smaller deformation in this case when it is on the mountain. Because the original frontal orientation is the same as the orientation of the mountain, the lee-side frontogenesis region is parallel to the front. This confirms that frontal deformation is mainly a result of the superposition effect, as shown by the d-value diagrams in Fig. 5.37. As in Case 4, the front moves about 800 km ahead of the front without the mountain after 96 h.

D. SUMMARY

We have investigated the influence of three-dimensional topography on a passing cold front with different shapes, scales and orientations of the mountains. In general, the cold front experiences a weakening on the upwind slope and an strengthening on the leeside slope. The frontolysis/frontogenesis is due to the superposition effect and the mountain-induced forcing. The superposition effect occurs when the cold center is over the mountain, which establishes a temperature gradient on the upwind side that opposes the temperature gradient of the cold front. Therefore, the intensity of the cold front on the upwind side is reduced, and conversely, the temperature gradient on the leeside is enhanced. This superposition effect has no net effect on the frontal intensity after the front has passed. The mountain-induced forcing indicates that the divergence upstream of the wind

maximum will reduce the temperature gradient by the stretching deformation and convergence downstream of the wind maximum will increase the temperature gradient. These divergence areas are consistent with earlier studies, which mainly have been in the two-dimensional framework. The major difference we obtained here is that it is the varying wind directions of the horizontal wind associated with the front that impinges on the mountain, rather than the mean advection flow, which will determine the locations of the upwind side and the leeside, and the magnitudes of the forcing.

The mountain flow is dominated by the pre-frontal southwesterly wind before the cold front reaches the mountain, and the mountain induces a frontogenetic forcing on the northern or northeastern slope. Because the wind direction rotates clockwise, the maximum forcing position also moves clockwise as the cold front approaches. After the front has passed over the mountain crest, the prevailing flow is dominated by the post-frontal northwesterlies. The maximum forcing position moves rapidly to the southern or southeastern slope of the mountain. As an illustration of how the frontogenetic forcing changes when the prevailing wind changes, the location of maximum frontogenetical forcing is plotted as the polar angle relative to the center of the mountain for all cases (Fig. 5.40). The most significant position change occurs in Case 3 for the east-west oriented mountain. Variations of the position angle for Case 4 and Case 5 are not pronounced since the orientation of the mountain is nearly parallel to the front. The magnitudes of the forcing decrease as the front climbs the mountain, reach a minimum when the front is on the top of the mountain and increase when the front moves to the leeside convergent zone. The forcing decreases again when the front moves to the divergent zone farther downstream.

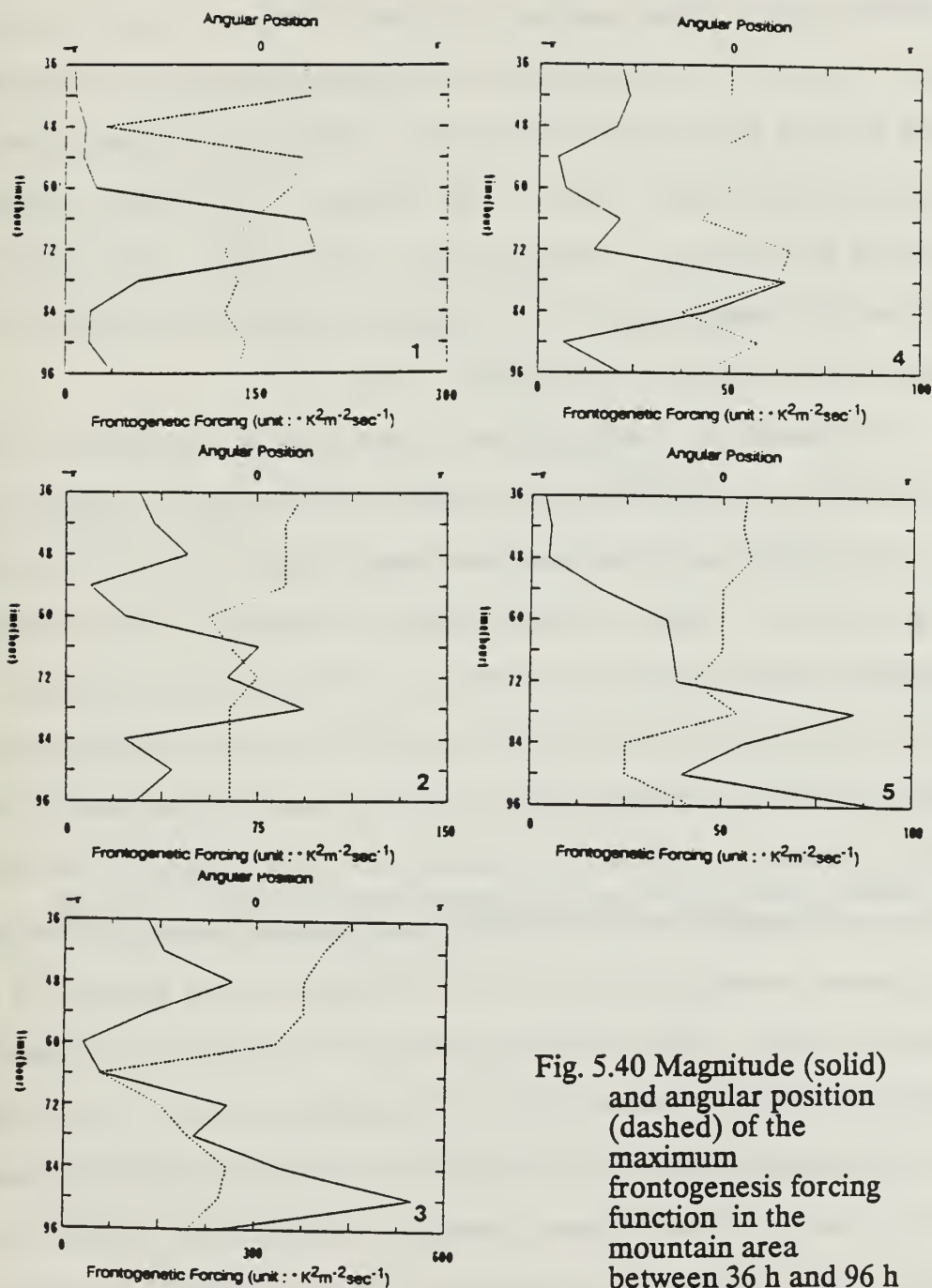


Fig. 5.40 Magnitude (solid) and angular position (dashed) of the maximum frontogenesis forcing function in the mountain area between 36 h and 96 h for Cases 1 to 5.

The horizontal coordinate is the forcing magnitude along the bottom (unit : $10^{-14} \text{ K}^2 \text{ m}^{-2} \text{ s}^{-1}$), and angular position along the top.

The frontogenetic forcing function is dominated by the horizontal deformation term, which may be separated into stretching deformation and shearing deformation terms. The stretching deformation becomes large when the flow is forced to go over the mountain, and the shearing deformation is large in regions where the flow goes around the mountain. The dominant effect depends on the wind speed and incident angle to the mountain. For circular mountains, the stretching and shearing deformation play equal parts. For elliptical-shaped mountains, the stretching deformation dominates because most of the flow is forced to go over the long axis of the mountain.

The maximum frontal intensities, as measured by the d -values, for the five mountain cases and the control case without the mountain are compared in Fig. 5.41. Note that in our three-dimensional study, the frontal intensity is not the same along the front. Before the fronts reach the mountain, all of the fronts are intensifying (decreasing d -values) slightly due to the baroclinic environment. After $t = 48$ h, the intensity for the front in the control case without a mountain decreases slightly due to internal diffusion in the model and reaches a quasi-steady state after $t = 54$ h. Cases 1, 2, 4 and 5 generally have similar trends. The front first experiences frontolysis on the upwind side and frontogenesis on the leeside. The frontogenesis extends downstream from the leeside and is followed by a weak frontolysis region. This leeside frontogenesis and frontolysis are induced by the convergence/divergence associated with the leeside gravity wave. After the fronts leave the mountain area at $t = 96$ h, all of the frontal intensities are approximately the same, and have about the same intensity as the control case without a mountain. In these four cases, the same amount of intensity change occurred over the mountain irrespective of the mountain size, shape and orientation.

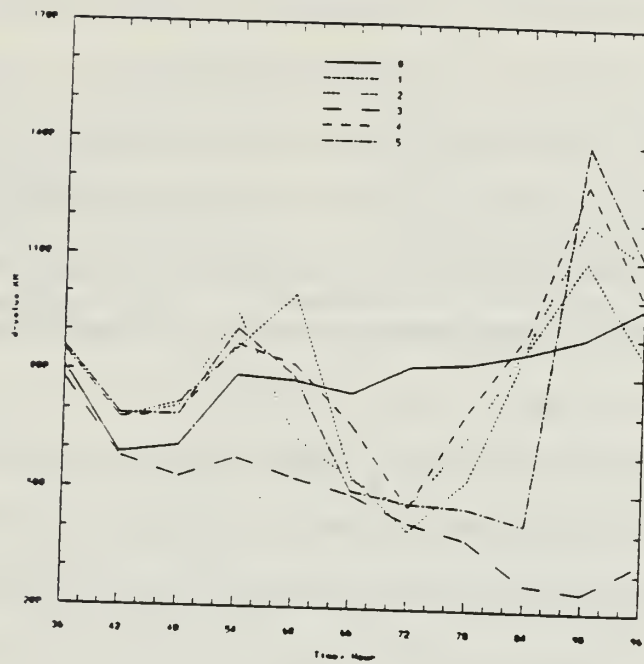


Fig. 5.41 Maximum frontal intensity (d-value, Km) of each of cases (value 0 refers to the no-mountain case) from $t = 36$ h to $t = 96$ h

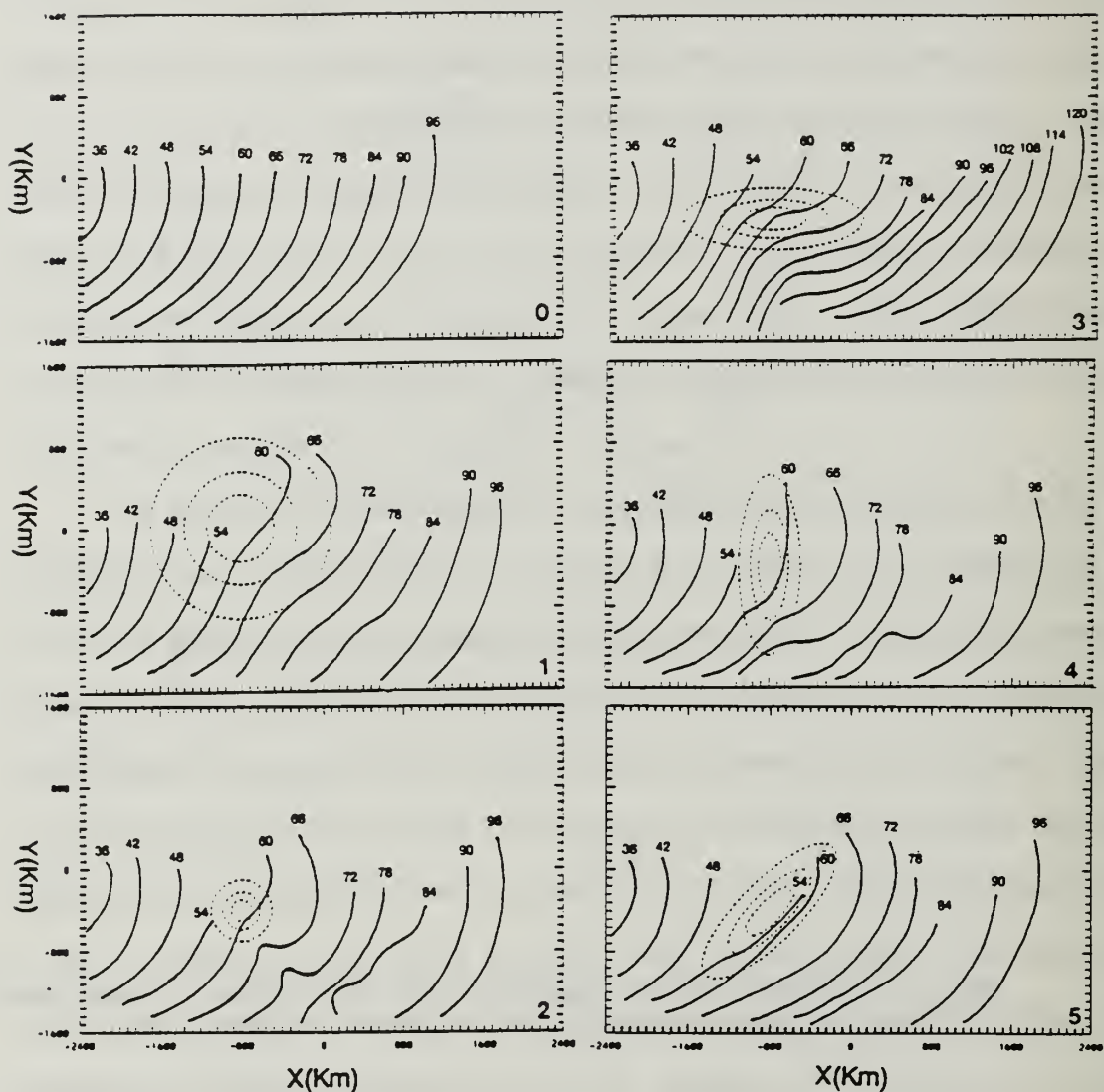


Fig. 5.42 Time evolution of the cold front positions for all cases determined by tracing the minimum d -value. Dashed lines indicate the contours of the mountain starting from 500 m, and with an interval of 500 m. Case 0 is the case with no mountain. Note that case 3 has been integrated to $t = 120$ h.

The frontal positions for all cases based on the positions of the minimum d -values, are sketched in Fig. 5.42. Except Case 3, all fronts with the mountain included experience two major acceleration periods. The first one occurs between 60 h and 72 h when the fronts move down the lee-side slope. The second period occurs between 78 h and 90 h when the fronts are within the divergent region. For better comparison among the cases, these positions are plotted in a single diagram in Fig. 5.43 for three times. At $t = 48$ h, the fronts have not yet been influenced by the mountain. At $t = 72$ h, the northern parts of the fronts have passed the mountain and moved 350 to 400 km ahead of the front without the mountain. This displacement is due to the advection by the large downslope wind on the leeside. At $t = 96$ h, the fronts are 800 km ahead of the front without the mountain, except for Case 3.

In the two-dimensional model of Williams *et al.* (1992), the frontal displacement is the same with and without the mountain. In the semi-geostrophic two-dimensional study of Zehnder and Bannon (1988), the frontal position after passing over the mountain is about 100 km ahead of the no-mountain case. The main reason for this discrepancy is that the mature front in the two-dimensional study of Williams *et al.* (1992) has a significant wind speed in the north-south direction that reaches 30 m/s, while the cross-front wind speed is only 13 m/s (Fig. 5.44). It is the cross-front wind that induces the strong downslope winds. In the present study, the frontal structure is more realistic and it is three-dimensional. The post-frontal wind has a large component normal to the mountain that generates much stronger downslope winds than in the two-dimensional study. This strong lee-side wind pushes the front much farther forward.

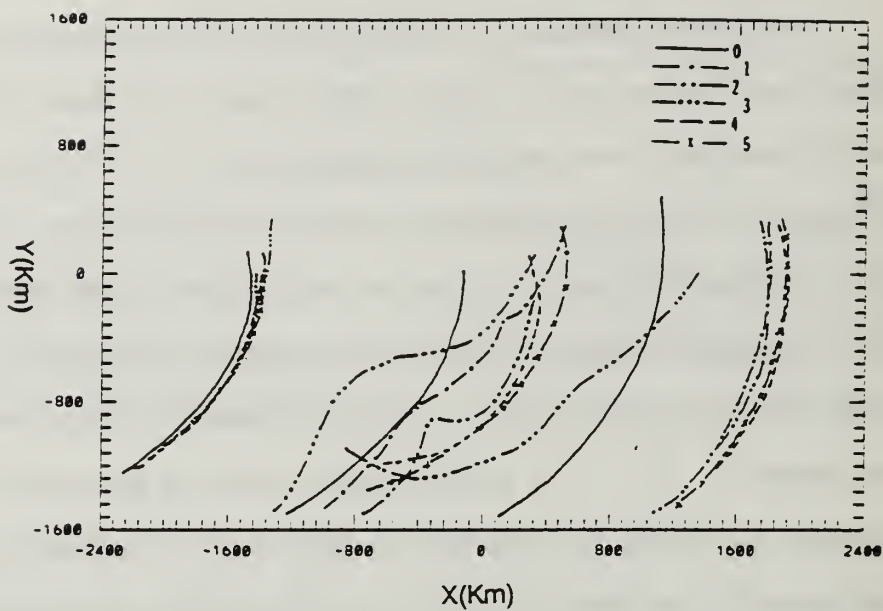


Fig. 5.43 Frontal positions for the six cases grouped at $t = 48$ (left group), 72 (central group) and 96 h (right group).

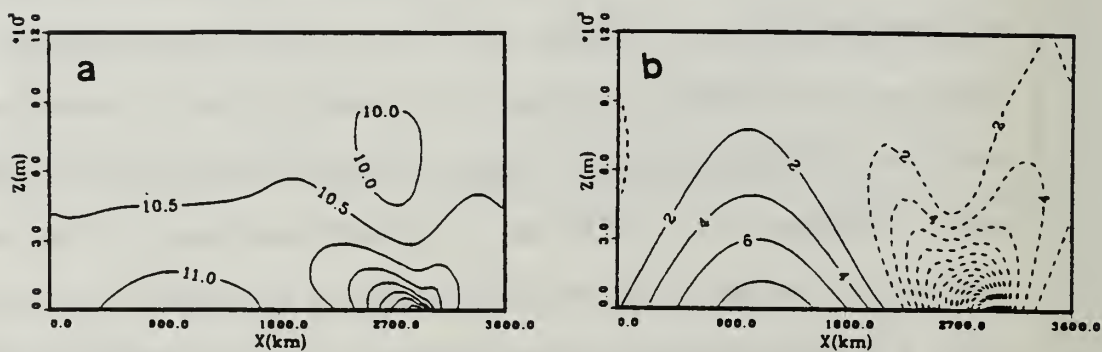


Fig. 5.44 Two-dimensional frontal solutions for (a) cross-frontal wind u (m/s), and (b) along-frontal wind v (m/s) from Williams *et al.* (1992).

Hoinka (1987) computed the frontal speeds on the windward side of Alps, across the Alps, and on the leeside to be about 8 m/s, 3 m/s and 17 m/s respectively. Davies and Phillips (1984) have described the mesoscale movement of the cold front across Switzerland and estimated a speed of about 5 m/s for the translation. The frontal speed for Case 3 computed here is based on the position diagram shown in Fig. 5.42. Since the front moves at different speeds in different parts, only a very rough estimate can be obtained. On the southwestern slope of the mountain where the front experiences the largest retardation, the frontal speed is 5.5 m/s. Over the mountain top, the frontal speed is 8.8 m/s. On the northeastern slope of the mountain where the front moves the fastest, the frontal speed is 16.6 m/s. These values are comparable with observed speeds in Hoinka (1987) and Davies and Phillips (1984). However, all of the frontal speeds are rough estimates.

Case 3 has a unique result due to orientation of the mountain and the front. Although some frontogenesis occurs associated with the pre-frontal regions, the major frontogenesis region is on the southern slope of the mountain. In other cases, the downslope wind has a major component toward the east, which is in the same direction as the basic flow advection. This downslope wind pushes the front faster toward the east. However, the strong downslope wind in Case 3 has a major component toward the south, instead of toward the east. Thus, the frontal position in Case 3 lags behind the other cases and allows the front to remain longer under the mountain influence. The averaged speed of the front in Case 3 is the same as the front without the mountain, which is slower than the other four cases. Only in Case 3 does the mountain have a net effect in increasing the frontal intensity.

In these experiments, the frontal distortion by the mountains has been shown to agree with some observational data and with earlier studies on mountain effects

on an idealized front. As opposed to previous dynamical studies, we found that the frontal distortion is mainly due to the superposition effect of the original front and the maximum frontogenesis region located on the leeside mountain slopes. There is no frontal distortion in Case 5 where the mountain is oriented in the same direction as the front so that the frontogenesis region on the leeside slope of the mountain is parallel to the front. When the front reaches there, its intensity is enhanced but the structure is not deformed. When the front leaves the mountain area, a temperature gradient disturbance is left behind at the same place. Due to more complicated frontogenesis regions, the front in the east-west mountain case (Case 3) appears to have the largest deformation.

VI. SUMMARY AND CONCLUSION

Observational studies have indicated that frontal systems change in intensity, speed and horizontal structure as they pass over mountains. Many analytical and numerical studies on the mountain influence on a front have been carried out. However, previous research has mostly focused on two-dimensional, or idealized fronts. In this dissertation, previous studies on the dynamical influence of the mountains on fronts have been extended to three-dimensional mountains with a realistic frontal system. A three-dimensional hydrostatic, adiabatic, primitive equation model has been used to achieve this objective. The frontal system has been spun up in the model in a baroclinically unstable atmosphere. Effects of mountain size, shape and orientation are examined, while keeping the height of the mountain at 2 km and the mean flow always westerly for simplicity.

In the three-dimensional numerical experiments here, it is found that the frontal structure is modified by the mountain in a more complex manner because of the more realistic frontal structure that is retained in the experiment. As in previous studies, the frontal intensity in the present study weakens on the upslope and strengthens on the downslope, respectively. During the frontal passage over the mountain, the impinging flow onto the mountain is dominated by the horizontal wind associated with the front, rather than that associated with the mean basic flow. Before the cold front reaches the mountain, the flow impinging on the mountain is predominantly the pre-frontal southwesterlies. After the front reaches the mountain, the dominant flow shifts to the post-frontal northwesterly. Since the impinging flow to the mountain changes during the frontal passage, the maximum

frontogenetic forcing shifts its position from the northern slope to the eastern slope and then to the southern slope. This is different from the previous three-dimensional studies (Blumen and Gross 1987b, Schumann 1987) in which the mean flow advects the idealized front and dominates the response to the mountain. In the two-dimensional studies, most of these complex flow-mountain interactions are excluded.

Horizontal wind fields and the frontogenesis forcing function are further examined to study the dynamics associated with the frontal changes over three-dimensional mountains. The most significant contribution to the frontogenetic forcing comes from the horizontal deformation terms, which include the stretching and shearing deformations. The stretching deformation is related to the convergent/divergent forcing discussed in the previous paragraph. The frontogenetic forcing is dominated by the stretching deformation when the air parcels are forced to go over the mountain. The shearing deformation, which has not been discussed in previous studies, has a significant contribution when the impinging flow goes around the mountain. The around-the-mountain flow induces horizontal wind shear that contributes to the modification of the temperature gradient of the front. Whether the flow goes over or around the mountain depends on the mountain size, flow speed and incident angle. For a circular mountain, shearing and stretching deformations contribute equally to the total horizontal deformation forcing, while the stretching term dominates for an elliptical-shaped or long mountains. These results differ from that of Blumen and Gross's (1987b) three-dimensional study, where the tilting term is larger or comparable to the convergence term. In their study, the frontogenetic forcing is computed based on the semi-geostrophic mountain solution that has no horizontal wind shear associated

with the front. The magnitude of the total frontogenetic forcing reaches a minimum when the front is on the mountain crest and a maximum when the front is at the base of the mountain on the leeside.

The maximum frontal intensities are traced during the integration for all the experiments and compared with the control experiment without mountain. The general trends in frontal intensity changes in these cases are similar to each other, with the frontal intensity weakening first when the front is on the upslope and strengthening to maximum value on the leeside. After the front moves away from the mountain, the intensity is reduced farther downstream and then recovers slightly. The locations where front experiences intensification and weakening correspond very well to the mountain-induced convergence/divergence region. The final intensity is generally similar and is comparable to the control experiment without a mountain, except for the east-west oriented mountain. Thus, the mountains have little net effect in this numerical model on the frontal intensity after some distance downstream from the mountain. These results are consistent with the two-dimensional study by Williams *et al.* (1992), and indicate that the mountain influence is a local effect in the dynamics of a dry model. However, the frontal intensity is increased after passing over the east-west oriented mountain in Case 3. In that case, the major downslope wind generated by the post-frontal flow is more toward the south instead of toward the east as in the other four cases. Therefore, the front experiences less acceleration toward east compared with the other cases. The front also spends more time within the lee side convergent zone and the frontal intensity has a net increase after passing over the mountain.

As the front passes over the mountain, the horizontal structure appears to be deformed. In previous idealized studies (Schumann 1987; Blumen and Gross 1987b

and Blumen 1992), the frontal distortion was conjectured to be the result of differential advection in which the front is accelerated on the northern slope by the mountain-induced anticyclonic flow and decelerated on the southern slope. In the present study in which a more realistic front is used, the frontal distortion is a superposition effect of the original front on the mountain-induced frontogenesis regions. Over a large circular mountain, only a slight frontal distortion is found because the frontogenesis is weaker and its region is broader on the leeside slope than that in the mesoscale mountain. The front experiences more deformation over the mesoscale circular mountain than that in the large-scale circular mountain. Frontogenesis in that case is stronger, but the area is smaller. The largest distortion of the front is induced by the east-west oriented mountain range. In this case, the major frontogenesis region is on the southern slope and therefore the southern part of the front is distorted into an east-west direction. For a north-south oriented mountain, the major frontogenesis region is on the eastern slope. Thus, the front becomes aligned with the mountain in a north-south orientation parallel to the leeside frontogenesis region. When the mountain is parallel to the orientation of the front, although the frontal intensity is increased when the front is on the leeside slope, there is no frontal distortion. This case confirms that the frontal distortion mainly arises from the superposition of the mountain-induced frontogenesis and the frontogenesis of the original front, rather than due to the advection by the mountain-induced anticyclonic circulation. After the front moves away from the mountain, the model front restores its original structure. However, the advective effect by the mountain flow has some, albeit small, effect in distorting the frontal structure, especially in the case of the east-west oriented mountain in which the post-frontal flows are more parallel to the long axis of the mountain.

In all cases, the front is decelerated on the upwind side and accelerated on the leeside of the mountain. After the front has moved away from the mountain region, the frontal displacements are about the same for all cases, except the east-west oriented mountain. The fronts generally move faster and are located to the east of the front in the control with no mountain. On the average, the front is about 750 to 800 km ahead of the front over the flat terrain after 96 h of integration. The acceleration is contributed by the strong downslope wind on the leeside. In Williams *et al.* (1992), the front with and without the mountain move approximately the same distance after the front passes the mountain. The major reason for this discrepancy is that in Williams *et al.* (1992), the large wind speed associated with the mature front is in the along-front direction, which is also in the along-the-mountain direction. In their study, the wind speed in the cross-front direction, which is in the cross-mountain direction, is much smaller than the along-front direction. This much smaller cross-mountain flow from the post-frontal wind in Williams *et al.* (1992) generates a much smaller downslope wind so that the front passes the mountain and advances the same distance as the front without the mountain. In the case for the east-west oriented mountain, which has quite different results from the other cases, the large downslope wind generated by the post-frontal flow is more toward the south with the east-west oriented mountain rather than toward the east as in the other cases. This is also the reason for more intensification of the front.

In conclusion, the most important factor that controls the mountain effects on the frontal structure, intensity and speed, is the mountain's orientation with respect to the approaching front.

The result of a front passing over an east-west oriented mountain resembles an observation of the frontal modification by the Alps (Kurz 1990). The frontal

speed of movement computed over different mountain regions also compares favorably with observations of a cold front passage over Alps during ALPEx (Hoinka 1987). It is encouraging that a model without moisture successfully simulated the observations under similar environmental conditions. This indicates that the dynamics play an important role in the mountain influence on fronts.

In nature, there are many other factors that may also modify the mountain influence on a frontal system. Some important factors include moisture effects and contributions from the planetary boundary layer processes. The moisture may modulate the vertical and horizontal temperature structure and have a great impact on both the frontal and mountain circulations. The condensation processes will cause differential heating in the system and may create convergence/divergence with large magnitudes. The boundary layer may induce different vertical fluxes that can also modify both the front and the mountain circulations. Finally, with a complex terrain profile, the mountain may have a more complicated impact on passing fronts. These and many other interactions of diabatic processes with adiabatic dynamics are left for future studies.

APPENDIX A

A. MODEL CONFIGURATIONS

In this model, $\sigma = p/p_s$ is used as the vertical coordinate to make the topography treatment easier. The equations can be written as follows,

x-component momentum equation:

$$\frac{\partial u}{\partial t} + u \frac{\partial u}{\partial x} + v \frac{\partial u}{\partial y} + \dot{\sigma} \frac{\partial u}{\partial \sigma} = - \frac{\partial \phi}{\partial x} + \frac{\sigma}{p_s} \frac{\partial \phi}{\partial \sigma} \frac{\partial p_s}{\partial x} + f v + F_x \quad (\text{A.1})$$

y-component momentum equation:

$$\frac{\partial v}{\partial t} + u \frac{\partial v}{\partial x} + v \frac{\partial v}{\partial y} + \dot{\sigma} \frac{\partial v}{\partial \sigma} = - \frac{\partial \phi}{\partial y} + \frac{\sigma}{p_s} \frac{\partial \phi}{\partial \sigma} \frac{\partial p_s}{\partial y} - f u + F_y \quad (\text{A.2})$$

hydrostatic equation:

$$\frac{\partial \phi}{\partial \sigma} = - \frac{RT}{\sigma} \quad (\text{A.3})$$

continuity equation:

$$\frac{\partial(p_s \dot{\sigma})}{\partial \sigma} = - \frac{\partial p_s}{\partial t} - \nabla \cdot (p_s \mathbf{V}) \quad (\text{A.4})$$

first law of thermodynamics:

$$\begin{aligned} \frac{\partial T}{\partial t} + u \frac{\partial T}{\partial x} + v \frac{\partial T}{\partial y} + \dot{\sigma} \frac{\partial T}{\partial \sigma} \\ = \frac{RT}{c_p} \left(\frac{\dot{\sigma}}{\sigma} - \frac{\partial \dot{\sigma}}{\partial \sigma} - \nabla \cdot \mathbf{V} \right) + \frac{Q}{c_p} \end{aligned} \quad (\text{A.5})$$

where $\phi = gz$ is the geopotential and T is temperature. Variables u and v are

horizontal velocity components in the x and y directions, respectively. The Coriolis parameter f is assumed to be constant. Diabatic heating will be neglected in this model, i.e. $Q = 0$.

The sigma vertical velocity vanishes at the top and bottom of the model. Flow in the x-direction is assumed to be periodic. A baroclinic disturbance will be used as the initial field for the frontogenesis model. Two- and three-dimensional mountains will be used in this research.

APPENDIX B

B. NUMERICAL METHOD

The equations are solved by a second-order accurate finite difference scheme. Arakawa's C-grid is used for the horizontal differencing because it is found to be best in simulating the geostrophic adjustment process. The vertical domain is divided into 16 layers. Since our study will focus on the lower atmosphere, most of the layers are concentrated on the bottom of the model. This configuration will provide a better resolution in the lower atmosphere. The time integration scheme is the split-explicit method, in which the linearized terms in the prognostic equations are separated into the slower moving Rossby modes and the faster gravity modes. The prognostic equation can be written in the following generic form:

$$F_t + [P] = [A], \quad (B.1)$$

where F_t is the tendency of momentum flux or thermal flux, $[P]$ is the pressure gradient force or divergence and the $[A]$ is the nonlinear term. The operator $[X]$ is the time mean of X in a time interval of $2\Delta t$.

The gravity modes in the nonlinear term $[A]$ are assumed to carry only a small fraction of the total energy, i.e. the gravity modes have small amplitude in the nonlinear terms so that the equations are quasi-linear. Therefore, the nonlinear term changes over the time scale of Rossby mode and can be integrated over the

time interval of Rossby mode. Then the equation can be written as:

$$F_t + [P] = A(t), \quad (B.2)$$

However, the P term changes over a time interval which is determined by all modes.

The above equation can be rewritten in the difference form respects to t :

$$\begin{aligned} F(t+Dt) - F(t-Dt) + 2Dt[P] &= 2DtA(t), \\ F(t+Dt) - F(t-Dt) + 2Dt([P] - P(t)) &= 2DtA(t) - P(t), \\ F(t+Dt) + 2Dt([P] - P(t)) &= F(t-Dt) - 2DtP(t) + 2DtA(t), \\ F(t+Dt) + 2Dt([P] - P(t)) &= F^{ex}(t+Dt), \end{aligned} \quad (B.3)$$

Thus, split-explicit integration can be calculated by the explicit scheme and a modification term $2Dt([P] - P(t))$.

In order to carry out the calculation of $[P]$ the grid point variables must be transferred to eigenspace, in which each mode can be treated independently. After calculation of the correction term in eigenspace, we can transfer the results back to the grid point space and obtain the change in momentum or thermal flux.

REFERENCES

- Arakawa, A., and V. R. Lamb, 1977: Computational design of the basic dynamical processes of the UCLA general circulation model. *Meth. Comput. Phys.* **17**, 174-264.
- Bannon, P. R., 1983: Quasi-geostrophic frontogenesis over topography. *J. Atmos. Sci.*, **40**, 2266-2277.
- Bannon, P. R., 1984a: A semi-geostrophic model of frontogenesis over topography. *Beitr. Phys. Atmosph.*, **57**, 393-408.
- Bannon, P. R., 1984b: Effects of stratification on surface frontogenesis: Warm and cold fronts. *J. Atmos. Sci.*, **41**, 2021-2026.
- Bannon, P. R., and J. A. Zehnder, 1989: Baroclinic flow over a mountain ridge. *J. Atmos. Sci.*, **46**, 703-714.
- Blumen, W., 1992: Propagation of fronts and frontogenesis versus frontolysis over orography. *Meteor. Atmos. Phys.* **45**, (in press).
- Blumen, W., and B. D. Gross, 1987a: Advection of passive scalar over a finite-amplitude ridge in a stratified rotating atmosphere. *J. Atmos. Sci.* **44**, 1696-1705.
- Blumen, W., and B. D. Gross, 1987b: Semi-geostrophic flow over orography in a stratified rotating atmosphere. Part I: Steady three-dimensional solutions over finite ridges. *J. Atmos. Sci.*, **44**, 3007-3019.
- Bosart, L. F., 1970: Mid-tropospheric frontogenesis. *Quart. J. Roy. Meteor. Soc.*, **96**, 442-471.
- Bosart, L. F., V. Pagnotti and B. Lettau, 1973: Climatological aspects of eastern United States back-door frontal passages. *Mon. Wea. Rev.*, **110**, 627-635.
- Buzzi, A., and S. Tibaldi, 1977: Inertial and frictional effects on rotating and stratified flow over topography. *Quart. J. Roy. Meteor. Soc.*, **103**, 135-150.
- Charney, J. G., 1947: The dynamics of long waves in a baroclinic westerly current. *J. Meteorol.* **4**, 135-163.
- Davies, H. C., 1984: On the orographic retardation of a cold front. *Beitr. Phys. Atmosph.*, **57**, 409-418.
- Davies, H. C. and P. D. Phillips, 1984: Frontal motion in mountainous terrain: analysis and implications for 0-12 hrs forecasts. Proc. Nowcasting-II Symposium, Norrköping Sweden, 3-7 Sept. 1984, ESA SP-208, 87-92.
- Eady, E. T., 1949: Long waves and cyclone waves. *Tellus*, **1**, 33-52.
- Egger, J., 1987: Distortion of fronts near orography. *Meteorol. Rdsch.*, **40**, 141-146.

- Godske, C. L., T. Bergeron, J. Bjerknes and R. C. Bundgaard, 1957: Dynamic Meteorology and Weather Forecasting. Amer. Meteor. Soc., Boston, 612 pp.
- Haderlein, K., 1989: On the dynamics of orographically retarded cold fronts. *Beitr. Phys. Atmosph.*, **62**, 11-19.
- Hoinka, K. P., 1986: On the diagnosis of a cold front observed during ALPEX. *Scientific results of the Alpine Experiment, Vol. II*. GARP Publ. Ser., No. 27, WMO/TD No. 108, 445-453.
- Hoskins, B. J., 1975: The geostrophic momentum approximation and the semigeostrophic equations. *J. Atmos. Sci.* **32**, 233-242.
- Hoskins, B. J., 1976: Baroclinic waves and atmospheric frontogenesis. Part I: Introduction and Eady waves. *Quart. J. Roy. Meteor. Soc.*, **102**, 103-122.
- Hoskins, B. J., and F. Bretherton, 1972: Atmospheric frontogenesis models: Mathematical formulation and solution. *J. Atmos. Sci.*, **29**, 11-37.
- Hoskins, B. J., and N. V. West, 1979: Baroclinic waves and frontogenesis. Part II: Uniform potential vorticity jet flows-cold and warm fronts. *J. Atmos. Sci.*, **36**, 1663-1680.
- Kurz, M., 1990: The influence of the Alps on structure and behavior of cold fronts over southern Germany. *Meteor. Atmos. Phys.*, **43**, 61-68.
- Madala, R. V., S. W. Chang, U. C. Mohanty, S. C. Mandan, R. K. Paliwal and V. B. Sarin, 1987: Description of the Naval Research Laboratory limited area dynamical weather prediction model. NRL Memorandum Report 5992. Naval Research Laboratory, Washington, DC 20375-5000, 131pp.
- McGinley, J., 1982: A diagnosis of Alpine lee cyclogenesis. *Mon. Wea. Rev.*, **110**, 1271-1297.
- Miller, J. E., 1948: On the concept of frontogenesis. *J. Meteor.*, **5**, 169-171.
- Palmen, E., and C. W. Newton, 1969: Atmospheric circulation systems. Academic Press, New York. 603 pp.
- Perkey, D. J., and C. W. Kreitzberg, 1976: A time-dependent lateral boundary scheme for limited-area primitive equation models. *Mon. Wea. Rev.*, **104**, 744-755.
- Pierrehumbert, R. T., 1984: Linear results on the barrier effects of mesoscale mountains. *J. Atmos. Sci.*, **41**, 1356-1367.
- Queney, P., 1947: Theory of perturbations in stratified currents with applications to air flow over mountain barriers. Misc. Rep. No. 23, Department of Meteorology, Univ. of Chicago.

- Queney, P., 1948: The problem of air flow over mountains: A summary of theoretical studies. *Bull. Amer. Meteor. Soc.* **29**, 16-26.
- Reed, R., and F. Sanders, 1953: An investigation of the development of a mid-tropospheric frontal zone and its associated vorticity field. *J. Meteorol.* **10**, 338-350.
- Sanders, F., 1955: An investigation of the structure and dynamics of an intense surface frontal zone. *J. Meteor.*, **12**, 542-552.
- Schumann, U., 1987: Influence of mesoscale orography on idealized cold fronts. *J. Atmos. Sci.*, **44**, 3423-3441.
- Simmons, A. J., and B. J. Hoskins, 1978: The life cycles of some non-linear baroclinic waves. *J. Atmos. Sci.*, **35**, 414-432.
- Smith, R. B., 1979a: Some aspects of quasi-geostrophic flow over mountains. *J. Atmos. Sci.*, **36**, 2385-2393.
- Smith, R. B., 1979b: The influence of mountains on the atmosphere. *Advances in Geophysics*, Vol. 21, Academic Press, 87-230.
- Smith, R. B., 1980: Linear theory of stratified hydrostatic flow past an isolated mountain. *Tellus*, **32**, 248-364.
- Smith, R. B., 1982: Synoptic observations and theory of orographically disturbed wind and pressure. *J. Atmos. Sci.*, **39**, 60-70.
- Smith, R. B., 1986: Mesoscale mountain meteorology in the Alps. *Scientific results of the Alpine Experiment, Vol. II*. GARP Publ. Ser., No. 27, WMO/TD No. 108, 407-423.
- Somieski, F., 1981: Linear theory of three-dimensional flow over mesoscale mountains. *Beitr. Phys. Atmosph.*, **54**, 315-334.
- Steinacker, R., 1981: Analysis of the temperature and wind fields in the Alpine region. *Geophys. Astrophys. Fluid Dyn.*, **17**, 51-62.
- Stone, P. H., 1966: Frontogenesis by horizontal wind deformation fields. *J. Atmos. Sci.*, **23**, 455-465.
- Snyder, C., W. C. Skamarock and R. Rotunno, 1991: A comparison of primitive-equation and semigeostrophic simulations of baroclinic waves. *J. Atmos. Sci.*, **48**, 2179-2194.
- Williams, R. T., 1967: Atmospheric frontogenesis: A numerical experiment. *J. Atmos. Sci.*, **24**, 627-641.
- Williams, R. T., and J. Plotkin, 1968: Quasi-geostrophic frontogenesis. *J. Atmos. Sci.*, **25**, 201-206.

Williams, R. T., M. S. Peng and D.A. Zankofski, 1992: Effects of topography on fronts. *J. Atmos. Sci.*, **49**, 287-305.

Young, G. S., and R. H. Johnson, 1984: Meso- and microscale features of a Colorado cold front. *J. Climate Appl. Meteor.*, **23**, 1315-1325.

Zehnder, J. A., and P. R. Bannon, 1988: Frontogenesis over a mountain ridge. *J. Atmos. Sci.*, **45**, 628-644.

INITIAL DISTRIBUTION LIST

		No. Copies
1.	Defense Technical Information Center Cameron Station Alexandria, Virginia 22304-6145	2
2.	Library, Code 052 Naval Postgraduate School Monterey, California 93943-5000	2
3.	Professor R. T. Williams Meteorology Department (Code MR/Wu) Naval Postgraduate School Monterey, California 93943-5000	1
4.	Professor M. S. Peng Meteorology Department (Code MR/Pg) Naval Postgraduate School Monterey, California 93943-5000	1
5.	Professor R. L. Elsberry Meteorology Department (Code MR/Es) Naval Postgraduate School Monterey, California 93943-5000	1
6.	Professor R. L. Haney Meteorology Department (Code MR/Hy) Naval Postgraduate School Monterey, California 93943-5000	1
7.	Professor C.-P. Chang Meteorology Department (Code MR/Cp) Naval Postgraduate School Monterey, California 93943-5000	1
8.	Professor A. L. Semtner Oceanography Department Naval Postgraduate School Monterey, California 93943-5000	1
9.	Dr. C. S. Liou Naval Research Laboratory Monterey, CA 93943	1

- | | | |
|-----|---|---|
| 10. | Dr. Simon. W. Chang
Naval Research Laboratory (Code 4220)
4550 Overlook Ave. S.E.
Washington, D. C. 20375-5000 | 1 |
| 11. | Professor C. Y. Tsay
Central Weather Bureau
64 Kung Yuen Rd.
Taipei, Taiwan, ROC | 1 |
| 12. | Professor G. T.-J. Chen
Atmospheric Sciences Department
National Taiwan University
Taipei, Taiwan, ROC | 1 |
| 13. | Shang-Wu Li
Central Weather Bureau
64, Kung Yuen Rd.
Taipei, Taiwan, ROC | 1 |

DUDLEY KNOX LIBRARY
NAVAL POSTGRADUATE SCHOOL
MONTEREY CA 93943-5101



GAYLORD S



